Silicon Photomultipliers for Visible Light Communications

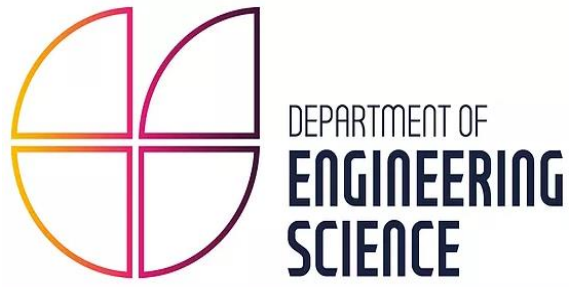
Zubair Ahmed, Mansfield College

University of Oxford

Hilary Term, 2022

Supervised by Prof. Steve Collins

This thesis is submitted to the Department of Engineering Science, The University of Oxford, in fulfillment of requirements for the degree of Doctor of Philosophy





Abstract

Over the past decade, avalanchephoto diodes (APDs) have widely been investigated for visible light communications. However, the gain and collection area of an APD is limited, which prevents this type of detector from improving its sensitivity. The gain is typically limited by excess noise, and its overall capacitance limits the collection area. Typically, the APDs of less than a square millimetre only have a bandwidth of more than 100 MHz. The excess noise factor can be avoided by biasing an APD above its breakdown voltage, significantly increasing its gain. The high gain makes an APD sensitive enough to detect photons down to a single photon, hence referred to as a single-photon avalanche diode (SPAD). Similarly, the collection area can be increased using a large array of SPAD elements. However, several important parameters are associated with the size of the array and a SPAD element, such as the effective recovery time, output pulse width or bandwidth, and linearity, which significantly impact the sensitivity and achievable data rate.

In this thesis, two off-the-shelf SiPMs are investigated as an OOK VLC receiver for indoor visible light communication and to study the impact of their various parameters on performance. For this reason, parameters such as bias-dependent dark count rate and photon detection efficiency at a particular wavelength, average standard output, optimum bias voltage, and dynamic range of selected SiPMs are characterised. Moreover, analytical models of these parameters are presented. These analytical models are then used to predict the performance of a SiPM-based VLC receiver. The performance of selected SiPMs is first evaluated in the dark without equalisation, where the impact of the bandwidth on the required power penalty due to intersymbol interference (ISI) is studied. The measured power penalty is then analysed by comparing it to the power penalty of a first-order low-pass system and a power penalty estimated based on the collection area, PDE, and the required average number of photons per bit.

Subsequently, the performance is evaluated with equalisation, and the sensitivity ratio between selected SiPMs is compared to study the impact of the collection area and the non-

linearity of SiPMs. The results obtained in the dark show that when equalsation is used, the SiPM with a larger collection area is approximately 4 times more sensitive than the SiPM with a smaller collection. Similarly, to evaluate the performance of SiPMs in the presence of ambient light, the impact of warm white LED with various absorption filters and combinations of absorption filters has been studied through various models. The performance of SiPMs is then evaluated in 500 lux of illuminance with a particular combination of absorption filters, selected based on transmittance at a wavelength equal to 405 nm and the ability to reject the ambient light from a warm white LED. The sensitivity ratio between selected SiPMs is then studied to see the impact of ambient light. The results in the ambient light show that when used with equalisation, due to the impact of ambient light, the sensitivity ratio is reduced to 2.5. However, despite the large SiPM being more susceptible to ambient light, the SiPM is still more sensitive than the small SiPM up to 1.2 Gbps. However, the limited bandwidth and non-linearity of the large SiPM mean that its sensitivity is limited at higher data rates.

Acknowledgements

I want to thank my colleagues Dr. Long Zhang at PengCheng Laboratory, Shenzhen, Dr. Hyunchae Chun at Incheon National University, Dr. Ravinder Singh at Toshiba Research Europe, Dr. Wajahat Ali at the University of Cambridge, Amna Riaz, Vincent Lee, and James Farmer at the University of Oxford for all of their participation in understanding theoretical concepts and for the technical support they provided in this project. I would also like to especially thank Mr. Grahame Faulkner for his help and advice in designing, setting up testbeds, and instrument troubleshooting.

In particular, I would like to thank both my Supervisor, Prof. Steve Collins, and co-supervisor, Prof. Dominic O'Brien, for providing an opportunity to work on this research project through which I have acquired valuable skills and experience for my future career. I am also grateful for their invaluable ideas, teaching, continuous encouragement, guidance, and advice, without which it would not have been possible to complete this research work.

List of Publications

1. W. Ali, G. Faulkner, Z. Ahmed, W. Matthews and S. Collins, "Giga-Bit Transmission Between an Eye-Safe Transmitter and Wide Field-of-View SiPM Receiver," in IEEE Access, vol. 9, pp. 154225-154236, 2021, doi: 10.1109/ACCESS.2021.3116704.
2. W. Ali, G. Faulkner, Z. Ahmed, W. Matthews, D. O'Brien and S. Collins, "Silicon photomultiplier receivers and future VLC systems," *2020 IEEE Globecom Workshops (GC Wkshps*, 2020, pp. 1-5, doi: 10.1109/GCWkshps50303.2020.9367590.
3. W. Ali, G. Faulkner, Z.Ahmed, and S. Collins, "A SiPM receiver that is compatible with a low-power, exempt 405 nm transmitter", *2020 Optical Wireless Communication Conference*.
4. Zubair Ahmed, Wajahat Ali, William Matthews, Grahame Faulkner, Dominic O'Brien, and Steve Collins (University of Oxford, UK), "Silicon Photomultiplier Receivers for Visible Light Communications.",*Photon 2020 IOP Webinars for the physics community* 1-4 September 2020.
5. W. Matthews, Z. Ahmed, W. Ali and S. Collins, "A SiPM-based VLC Receiver for 3.45 Gigabits/s Communication Using OOK Modulation,"2020 IEEE Photonics Conference (IPC), Vancouver, BC, Canada, 2020, pp. 1-2, doi: 10.1109/IPC47351.2020.9252218.
6. Z. Ahmed, L. Zhang, G. Faulkner, D. O'Brien and S. Collins, "A Shot-Noise Limited 420 Mbps Visible Light Communication System using Commercial Off-the-Shelf Silicon Photomultiplier (SiPM)," 2019 IEEE International Conference on Communications Workshops (ICCWorkshops), Shanghai, China, 2019, pp. 1-5.
7. Long Zhang, Zubair Ahmed, Hyunchae Chun, Grahame Faulkner, Dominic O'Brien and Steve Collins (University of Oxford, UK), "Single Photon Counting Receivers for Visible Light Communications.", *IOP Institute of Physics Photon 2018* 3-6 September 2020, Aston University Birmingham.
8. W. Matthews, Z. Ahmed, W. Ali and S. Collins, "A 3.45 Gigabits/s SiPM-based OOK VLC Receiver," in IEEE Photonics Technology Letters, doi: 10.1109/LPT.2021.3069802.
9. W. Matthews, W. Ali, Z. Ahmed, G. Faulkner and S. Collins, "Inter-Symbol Interference and Silicon Photomultiplier VLC Receivers in Ambient Light," in IEEE Photonics Technology Letters, vol. 33, no. 9, pp.449-452, 1May1, 2021, doi: 10.1109/LPT.2021.3067511.
10. C. He, Z. Ahmed and S. Collins, "Signal Pre-Equalization in a Silicon Photomultiplier-Based Optical OFDM System," in IEEE Access, vol. 9, pp. 23344-23356, 2021, doi: 10.1109/ACCESS.2021.3056148.
11. Z. Ahmed, R. Singh, W. Ali, G. Faulkner, D. O'Brien and S. Collins, "A SiPM-Based VLC Receiver for Gigabit Communication Using OOK Modulation," in IEEE Photonics Technology Letters, vol. 32, no. 6, pp. 317-320, 15March15, 2020.
12. L. Zhang, H. Chun, Z. Ahmed, G. Faulkner, D. O'Brien and S. Collins, "The Future Prospects for SiPM-Based Receivers for Visible Light Communications," in Journal of Lightwave Technology, vol. 37, no. 17, pp. 4367-4374, 1 Sept.1, 2019.

Contents

Abstract 2
Acknowledgements 4
List of Publications 5
List of figures 8
List of tables 10
Acronyms and Abbreviations 11
Nomenclature 12
Chapter 1 14
Introduction 14
1.1 Motivation 14
1.2 Background of VLC 15
1.3 Challenges 17
1.4 Recent trends of VLC receivers 18
1.5 Aims and objectives of the project 20
1.6 Summary 21
Chapter 2 23
Background of a VLC Receiver 23
2.1 Introduction 23
2.2 Basics of a single photon avalanche diode 23
2.3 Basics of a SiPM 26
2.4 Optical receiver for communication 30
2.4.1 Receiver with no background and bit error rate 30
2.4.2 Receiver with background 33
2.5 Bandwidth, data rate, and inter-symbol interference (ISI) 36
2.6 Communication Scenario 38
2.7 Summary 39
Chapter 3 41
Characterisation of Silicon Photomultipliers 41
3.1 Introduction 41
3.2 Off-the-shelf SiPMs 42
3.3 onsemi$_{TM}$ J-Series SiPMs 43
3.4 Characterisation of J-Series SiPMs 45
3.4.1 Bias dependent dark count rate 45

3.4.2 Bias dependent photon detection efficiency....49
3.4.3 The average standard output....53
3.4.4 Dynamic range....56
3.5 Effective PDE vs. the Irradiance....61
3.6 Summary....63
Chapter 4....66
Performance Evaluation....66
4.1 Introduction....66
4.2 Experimental setup....67
4.3 Channel response....68
4.4 Link results in the dark....69
4.4.1 Results without equalisation....70
4.4.2 Results with equalisation....77
4.4.3 Equalisation results and estimation of the average irradiance....81
4.5 Impact of ambient light....84
4.6 Link results in ambient light....90
4.7 Comparison of irradiance....94
4.8 Summary....95
Chapter 5....99
Conclusion and Future Work....99
5.1 Summary....99
5.2 Future work....104
References....108

List of figures

Figure 1.1 A generic VLC link structure system. The transmitter and receiver and separated by a free-space optical channel 15

Figure 2.1 Equivalent circuit of a basic single SPAD element (a) and a SPAD with quenching resistor (b).....24
Figure 2.2 Example of current flowing through a SPAD element as a function of time. The pulse is asymmetric around $t = t_{max}$ because of $R_Q \gg R_S$ 25
Figure 2.3 Equivalent circuit of a SiPM biased with an external voltage source V_{BIAS}. The dashed box shows single microcell consists of a basic SPAD and a quenching resistor R_Q. 26
Figure 2.4 Performance of RS (255,239) decoder capable of correcting eight symbol errors 32
Figure 2.5 The average number required photons per bit at a range of background counts per bit to achieve a BER equals to 1×10^{-3} 34
Figure 2.6 Example of an OOK signal received at the output of the receiver with infinite bandwidth (a) and finite bandwidth (b). The receiver with finite bandwidth clearly shows the impact of ISI.36
Figure 2.7 Power penalty required by a single-pole low-pass system vs. the ratio of 3 dB bandwidth to data rate.....37
Figure 2.8 Spectrum of warm (dotted line) and cool (solid line) white LED lamp (Philips IBRS) measured using ocean optics SD2000 spectrometer 38

Figure 3.1 Simplified schematic of onsemi$_{TM}$ SiPM. Unlike standard SiPMs, each junction in the SiPM device has a connection to a third electrode with low capacitive coupling.....44
Figure 3.2 Experimental setup used to measure the average standard output pulse of the 30035 SiPM 46
Figure 3.3 Signal captured in the total dark from the fast readout of the 30035 when biased at 28 V (Top) and histogram of the signal (Bottom). The inset shows the histogram of the pulses above the threshold value.....47
Figure 3.4 Dark count rate as a function of the bias applied at the 30035 at a surrounding temperature of 30 degree Celsius around the SiPM.....48
Figure 3.5 Block diagram of the experiment set-up to measure the measure bias-dependent PDE of the 30035 at 405 nm 50
Figure 3.6 Resultant beam of the 405 nm transmitter.....51
Fig. 3.7 Bias dependent PDE of the 30035 SiPM at 405 nm 52
Figure. 3.8 Shape of the standard output pulse of J-Series SiPMs [76].....54
Figure. 3.9 The standard output pulse of the MicroFJ-SMA-30035 when biased at 28 V captured from Agilent's Infiniium DSO9254A 2.5 GHz, 20 Gsa/s scope. The pulse is averaged over 512 pulses triggered using the scope's built-in averaging function 55
Figure 3.10 Block diagram of the experiment set-up to measure the response of the 30035 and the 60035 SiPM 56
Figure 3.11 The insight of saturation response of the 30035 and the 60035 57
Figure 3.12 Measured photocurrent as a function of irradiance at 405 nm reaching the 30035 and the 60035 SiPM when both biased at 28 V.....57
Figure 3.13 Ratio of the estimated currents and measured currents between the 60035 and 30035 at a range of irradiance 60
Fig. 3.14 Estimated PDE vs. the average irradiance reaching the 30035 and the 60035 SiPM .61

Fig. 3.15 Estimated PDE vs. the ratio of the recovery time to the average time between the photon hitting the microcell> 62

Figure 4.1 System block diagram describes the experimental setup used to evaluate the performance of selected J-Series SiPMs.....67
Figure 4.2 Frequency response of the link when the 30035 (black dashed) and 60035 (grey dotted) are used. The solid line is the first-order low-pass filter responses with τ = 0.75 ns (black solid) and τ = 1.8 ns (grey solid).....68
Figure 4.3 Data rate vs. average irradiance required by the 30035 and the 60035 to achieve a target BER of 1×10^{-3}. The performance is evaluated in the dark without equalisation applied at the received signal 74
Figure. 4.4 Power penalty vs. the ratio of the 3dB bandwidth to the data rate. Black and grey circles show the measured power penalty for the 30035 and 60035, respectively, and when no equalisation is applied to the received signal 75
Figure. 4.5 (i) Eye diagrams of the signal received at 500 Mbps (left), 1 Gbps (middle), and 2 Gbps (right). Eye diagrams in the top row show signal without equalisation, and diagrams in the bottom row show signal with equalisation when the 30035 is used as a VLC receiver 78
Figure. 4.6 Data rate vs. average irradiance required by the 30035 and 60035 to achieve a target BER of 1×10^{-3} in the dark 79
Figure 4. 7 Data rate vs. average irradiance required by the 30035 and the 60035 when evaluated the performance in the dark and the DFE (circle) is applied on the received signal.....82
Figure 4.8 Power penalty of the 30035 and 60035 with equalisation vs. the ratio of 3dB bandwidth and data rate. The solid line shows the power penalty of the first-order low-pass system 82
Fig. 4.9 Distribution of dark pulses captured from the fast output of the 30035 and the 60035. Solid line shows Gaussian fit to the distribution with mean (μ) and standard deviation (1σ) equal to 4.84×10^{-3} and 7.9×10^{-4} for the 30035, and 1×10^{-2} and 4×10^{-3} for the 60035 respectively 83
Figure 4.10 Transmittance of various glass filters at a range of wavelengths. The transmittance data of these glass filters is extracted from their datasheets provided by Edmund Optics.....85
Fig. 4.11 Spectral irradiance of warm white LED at a range of wavelength. The data is taken from [100].....86
Fig. 4.12 Luminous flux at a range of wavelength converted from the spectral irradiance of the warm white LED using Equation 4.9.....87
Fig. 4.13 Average irradiance required by the 30035 and the 60035 to achieve the target BER at a range of data rates when the equalisation is employed, and the ambient light level is equal to 500 lux 91
Figure 4.14 Ratio of the linear response to the measured SiPM current vs. the irradiance falling on the SiPM 92
Figure 4.15 Ratio between the average irradiance required by the SiPM in 500 lux and in the dark at a range of data rates 93
Figure 4.16 The ratio between the average irradiance required by the 30035 and the 60035 when operating in the dark with and without equalisation and in 500 lux with equalisation 94

List of tables

Table 1.1 The irradiance required by different VLC receivers to achieve a BER less than 3.8×10^{-3} or FEC limit at different data rates 19

Table 2.1 The average number of photons (n_s) required by a noiseless optical receiver to achieve various BERs 31
Table 2.2 Relationship between quality and BER of an image and a few video formats 33

Table 3.1 Performance parameters of various commercial SiPM modules (First Sensor, Hamamatsu, AdvanSiD, KETEK and onsemi$_{TM}$) 43
Table 3.2 SiPM and optical power detector parameters for Equation 2.2, 3.3 and 3.4 52
Table 3.3 Parameter values used in equation (3.8), (3.9), and (3.11) to estimate the photocurrent generated by SiPMs 59

Table 4.1 Slope and constant value of fits shown in Figure 4.4 80
Table 4.3 Thickness and transmittance at 405 nm of selected glass filters 85
Table 4.4 The transmittance of various glass filters and combinations of glass filters at 405 nm and their estimated detected count rate for the 60035 at a range of wavelength of the warm white LED 88
Table 4.5 Slope and constant value of fits to average measured irradiance in Figure 4.13 91

Acronyms and Abbreviations

APD	Avalanche Photodiode
AP	After-Pulse
CT	Cross-talk
DCR	Dark Count Rate
DFE	Decision Feedback Equalisation
DVLC	Diffused Visible light Communication
FWHM	Full Width Half Maximum
GM-APD	Geiger-mode APD
IM/DD	Intensity Modulation Direct Detection
ISI	Inter-symbol Interference
LED	Light Emitting Diode
NRZ	Non-return-to-zero
OOK	On-Off Keying
OWC	Optical Wireless Communication
OD	Optical Density
PDE	Photon Detection Efficiency
QL	Quantum Limit
RF	Radio Frequency
SPAD	Single Photon Avalanche Diode
MPPC	Multi-Pixel Photon Counter
SiPM	Silicon Photomultiplier
SBR	Single Bit Response
UV	Ultra-violet
VLC	Visible Light Communication
AOI	Angle of Incident
FOV	Field of View
BER	Bit Error Rate/Ratio

Nomenclature

Physical constant

c	299 792 458 m/s	(Speed of light)
e	2.718281828	(Euler's number)
π	3.141592654	(Ratio of the circumference over the diameter of a circle)
q_e	1.602×10^{-19} C	(Electron charge)
h	6.626×10^{-31} $J\times s$	(Planck's constant)

Mathematical and physical variables

V_{br}	Breakdown voltage
V_{bias}	Bias voltage
V_{ov}	Overvoltage
τ_{rise}	Rise time
τ_{fall}	fall time
η	Quantum efficiency
FF	fill factor
V_{rel}	Relative voltage
n_s	Signal photons per bit
n_b	Background counts per bit
n_T	Threshold number
n_1	Sum of signal photons and background counts per bit
$\sigma0$	Standard deviation of received 0s
$\sigma1$	Standard deviation of received 1s
PP	Power penalty
BW	Bandwidth
R_b	Data rate
A_{SiPM}	Area of a SiPM
A_{PD}	Area of optical power detector
$A_{\mu cell}$	Area of a microcell

E_{ph}	Energy of photon
$C_{\mu cell}$	Microcell capacitance
C_t	Terminal capacitance
$q_{\mu cell}$	Microcell charge
I_{SiPM}	SiPM current
$N_{\mu cell}$	Total number of microcell
r_{np}^{max}	Non-paralysable maxiumum count rate
r_{p}^{max}	paralysable maxiumum count rate
r_{np}	Non-paralysable count rate
r_p	Paralysable count rate
$r_{incident}$	Incident photon rate
$r_{background}$	Background count rate
T_r	Effective recovery time
$T_{inter-\mu cell}$	Average time between two photon incident on a microcell
T_b	Duration of the bit
G	Gain
ω	Angular frequency
I_{avg}	Average irradiance
R_e	Extinction ratio
I_1	Irradiance corresponds to logic ‘1’
I_0	Irradiance corresponds to logic ‘0’
I_{rr}	Irradiance
ϕ_v	Luminous flux per square metre
$V(\lambda)$	Luminous efficiency
K	luminous efficacy
τ_i	Transmittance
t	Symbol error
n	Length of codeword
k	Number of data symbols

Chapter 1

Introduction

1.1 Motivation

In traditional electronic systems, the communication between two electronic devices take place via copper cables such as in the USB, Ethernet and Serial port communication or via microwaves such as Wireless LAN (WLAN), WiMax and Bluetooth. However, the cost of cabling and the radio interference are increasingly posing problems. Moreover, the number of devices, such as smartphones, tablets, and laptops, and their applications, e.g., video conferencing and video streaming, such as streaming of high resolution (4k/8k) videos both are continuing to increase dramatically, which demand high transfer rate. A report published in October 2021, shows that the number of unique mobile phone users around the world has reached to 67.1% of the world's total population [1]. This increase in the number of mobile users and applications clearly indicates that the radio frequency (RF) spectrum is nearly scarce and unable to handle such a large number of users or wireless services [2], [3].

In recent years, optical wireless communication (OWC) has been emerged as a complimentary solution to existing RF wireless systems. Recent advancement in silicon technology has made a significant contribution to the development of high-speed sources such as LEDs and laser diodes and sensitive detectors, such as APDs and PIN photodiodes having a bandwidth in the range of gigahertz (GHz). These silicon-based detectors are more sensitive in the visible light and can provide a better performance in the visible band for a short range communication. Optical wireless communication systems operating in the visible spectrum commonly referred to as visible light communication (VLC) [4]. VLC can be used in various scenarios such as such as indoor broadband access, vehicle to traffic light and vehicle to vehicle communication, underwater communication, distributed lighting remote monitoring and control [5].

Other advantages of VLC include license-free band, frequency re-use, free from electromagnetic interference and secure.

In addition to VLC, the millimetre-wave (mmWave) is also a favourable choice capable of providing gigabit per second data rates for short-range communication in an indoor environment [6]. Similar to VLC, the performance of a mmWave system is strongly dependent upon the line-of-sight (LOS) channel; therefore, highly directive propagation is required. Due to this nature of propagation, both mmWave and VLC are susceptible to the blockage induced by obstacles in the LOS path. However, the launching cost of mmWave systems is much higher than VLC systems as highly directive antenna arrays and beamforming are required for mmWave communication [7]. In particular, the launching cost of VLC can significantly be lowered compared to mmWave, especially in environments where illumination is essential. Furthermore, VLC is safe for human eyes and skin (depending upon wavelength and intensity), and for electromagnetic interference (EMI) sensitive scenarios such as aircraft and hospitals [7].

1.2 Background of VLC

The basic structure of a VLC system may consists of a transmitter, optical channel and a receiver

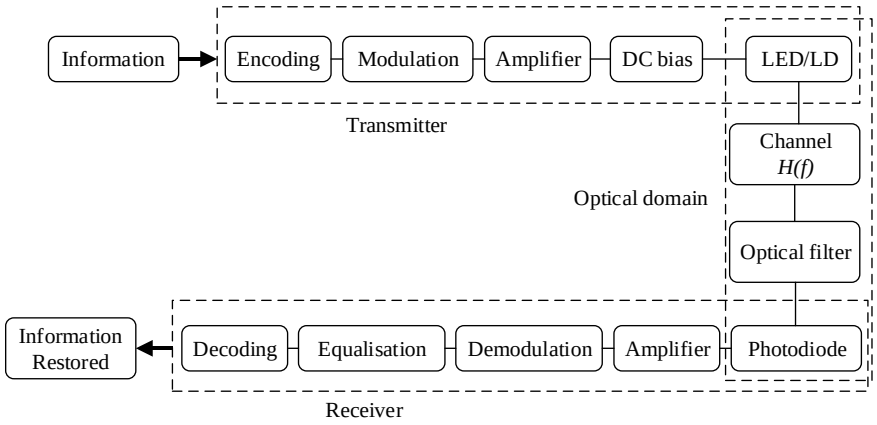


Figure 1.1 A generic VLC link structure system. The transmitter and receiver and separated by a free-space optical channel

as shown in Figure 1.1. The transmitter in a VLC system is responsible to transmit the digital

information to the receiver by using the principle of intensity modulation (IM), which is a process varying the intensity of the light according the information. Typically, semiconductor light sources are used in the front end of the transmitter to vary the intensity of light. The advantage of using semiconductor light sources is their long life, cost effectiveness, low power consumption, and switching rate at several megahertz (MHz) [Strathclyde]. The semiconductor light sources may include LEDs, and laser diodes. A VLC transmitter also consist of an encoder, which encode to the information into binary data, a modulator, which convert the binary data into a specific modulation format such as non-return-to-zero (NRZ) or multi-level PAM signal, and may also include optics and other important electronic components such as an amplifier and Bias-Tee to drive a LED or a laser diode.

The wireless optical channel in a VLC system represents the gap between the transmitter and receiver. Although the channel in a VLC has no electrical or RF inference, the optical channel may be significantly influenced by the ambient light or by the other VLC transmitters in the vicinity [8]. Similarly, the receiver in a VLC system may include optical filters, a photodiode (PD) for direct detection, which converts the incident light to an electrical signal, a transimpedance amplifier, and processing elements, such as demodulation, synchronization, and decoding to convert the received signal back into the original information [9].

So far most of the VLC systems being researched for indoor environment and short-range communications, which still may not fully replace the RF-based wireless systems due its coverage and mobility issues. However, despite these drawbacks, VLC systems can still provide relatively higher data rates than conventional RF-based wireless systems [10]. For example, existing WiFi protocols are limited to a few hundreds of Mbps [11], [12]. Whereas, VLC systems have already demonstrated data rates of several gigabits per second (Gbps) for indoor environment and also addresses the increasing demand of data consumption in indoors, which cannot be fulfilled by RF wireless systems alone [13], [14], [15], [16]–[18]. However, the irradiance required to achieve a

target bit-error-rate (BER) at a given data rate is the key characteristic of a VLC system. It is worth noting that the irradiance required by a VLC receiver should be within in the eye-safe limit [19].

1.3 Challenges

Ideally, a VLC system requires a high bandwidth transceiver, wide field of view (FOV) or coverage, large dynamic range, no interference from ambient light, and sensitive receivers so that the maximum possible data rate can be achieved with a minimum bit error rate (BER). However, in practice, a VLC system has a finite bandwidth, dynamic range and FOV, and is susceptible to ambient light, which impairs its sensitivity and limits the maximum achievable data rate and BER. Moreover, eye safety concerns poses a limit on the level of exposure of eye to the intensity of light, which means that the intensity of light in VLC systems cannot exceed a certain limit [19], [20], [21]. Therefore, a VLC system requires that the receiver have a high dynamic range, large bandwidth, and be sensitive enough to support communication at least in the range of Gbps.

Over a few years, APDs and PIN photodiodes have most widely been investigated for VLC systems. Typically, APDs have higher level sensitivity compared to PIN photodiodes due to the avalanche multiplication in their active regions. The process of avalanche multiplication increases the gain of APDs several times compared to the gain a typical PIN photodiode, and thus provide much higher sensitivity [22]. However, APDs require higher operating voltage than PIN photodiodes, and also the statistical nature of the avalanche process in APDs results to produce a higher level of noise, which limit their gain between a few tens to hundred [22], [23]. Although several sensitive silicon APDs are available in the market, such as single-photon counting modules (SPCM) from THORLABS and MICRO PHOTON DEVICES (MPD) [24], [25], which are sensitive enough to detect photons down to a single photon. Their collection area is limited, and due to the cost, these are available to high-end users only [26]. Typically, APDs having an

collection area of larger than one square millimeter do not exhibit a bandwidth larger than 100 MHz [27].

A larger active area of an APD means that it can cover more light at a given irradiance than an APD with a smaller active area. However, the capacitance also increases with increasing the collection area, which limits the bandwidth, and dynamic range or linearity of an APD. The bandwidth of an optical detector is an important parameter, which significantly impacts on the irradiance required to achieve a target BER at a given data rate. The sensitivity of a VLC receiver may also be impaired by the optical interference. In an indoor environment, the optical interference may come from domestic lights, such as fluorescent and LED lights. Typically, the narrow bandpass filters are preferred to reject this optical interference [28], [29]. However, their performance is guaranteed only at a normal angle of incident (AOI), which means that the spectral properties of these types of optical filters may change significantly with the AOI. Hence, the FOV is limited; therefore, it is challenging to have a wide FOV while maintaining the transmittance and quality of a filter to reject optical interference [21].

1.4 Recent trends of VLC receivers

Over the past decade, APDs have drawn a lot of attention by researchers for sensitive VLC receivers. Table 1.1 summarises and compares the sensitivity of various commercially available off-the-shelf (COTS) and custom-designed APD-based VLC receivers. From Table 1.1, it can be seen that among receivers based on APDs and PIN photodiodes, the APD with a diameter of 800 μm built using BiCMOS technology reported in [30] is the most sensitive. For instance, this APD requires an irradiance of 223 mWm^{-2}, 281 mWm^{-2}, and 560 mWm^{-2} at a data rate of 500 Mbps, 1 Gbps, and 2 Gbps to achieve a BER of 1×10^{-3}, which is significantly less than irradiances required by other VLC receiver based on APDs or PIN photodiodes. Conversely, Hamamatsu Photonics' 3 mm, and FEMTO's 400 μm diameter PIN photodiodes reported in [31] and [32] require an

irradiance almost two orders of magnitude and more than five orders of magnitude, respectively, to achieve a target BER of 1×10^{-3} compared to the APD with a diameter of 800 μm. Similarly, the

Detector (Area[m^2]/diameter[μm])	Data rate [Gbps]	Irradiance (W/m^2)	BER	Optical Power (dBm)	Ref.
APD BiCMOS (200 μm)	2.5	8.4	1×10^{-3}	–35.8	[33]
CMOS Receiver (1×10^{-8} m^2)	2.5	400	1×10^{-3}	–24	[34]
onsemi 30035 (9.42×10^{-6} m^2)	2.4	132×10^{-3}	1×10^{-3}	–29	[14]
APD BiCMOS (800 μm)	2	560×10^{-3}	1×10^{-3}	–35.5	[30]
APD BiCMOS (200 μm)	2	4.8	1×10^{-3}	–38.2	[33]
onsemi 30035 (9.42×10^{-6} m^2)	2	11.5×10^{-3}	1×10^{-3}	–39.6	[14]
onsemi 30035 (9.42×10^{-6} m^2)	1.4	2.3×10^{-3}	1×10^{-3}	–46.6	[14]
APD HV CMOS (200 μm)	1.25	4.2	1×10^{-3}	–38.8	[35]
APD BiCMOS (800 μm)	1	281×10^{-3}	1×10^{-3}	–38.5	[30]
APD BiCMOS (200 μm)	1	3.6	1×10^{-3}	–40	[33]
onsemi 30035 (9.42×10^{-6} m^2)	1	1.34×10^{-3}	1×10^{-3}	–49	[14]
First Sensor AD800-11 (1×10^{-6} m^2)	0.7	76	-	–14.2	[17]
onsemi 30035 (9.42×10^{-6} m^2)	0.8	0.8×10^{-3}	1×10^{-3}	–50	[14]
APD210 (500 μm)	0.62	1280	1.8×10^{-3}	–6	[36]
APD BiCMOS (800 μm)	0.5	223×10^{-3}	1×10^{-3}	–39.5	[30]
Hamamatsu PIN (10784) (3 mm)	0.5	12.60	1×10^{-3}	–10.5	[31]
Femto (HSA-X-S-1G4-SI) (400 μm)	0.5	5960	2.8×10^{-3}	–1.25	[32]
onsemi 30035 (9.42×10^{-6} m^2)	0.5	1.2×10^{-3}	1×10^{-3}	–49.4	[37]
Custom SPAD array (7.28×10^{-6} m^2)	0.4	1.4×10^{-3}	1.8×10^{-3}	–50	[38]
onsemi 30035 (9.42×10^{-6} m^2)	0.4	0.96×10^{-3}	1×10^{-3}	–50.5	[37]
Hamamatsu PIN (S10784) (3 mm)	0.32	852.4	1×10^{-3}	7.8	[39]

Table 1.1 The irradiance required by different VLC receivers to achieve a BER less than 3.8×10^{-3} or FEC limit at different data rates

APD with a diameter of 200 μm built using BiCMOS technology reported in [33] requires an

irradiance a factor of thirteen at 1 Gbps and nine at 2 Gbps when compared to 800 μm BiCMOS APD.

In contrast to APDs and PIN photodiodes, the array of single-photon avalanche diodes (SPAD), also referred to as silicon photomultipliers (SiPMs), have also been investigated as a sensitive VLC receiver reported in [26], [38], [40]–[47] [48]–[50]. A silicon photomultiplier consists of an array of SPAD elements that increase its collection area. Thus, a VLC receiver can achieve significantly higher sensitivity in this way. Results in [50] already show that a 1 mm^2 (C11209-110) SPAD-based VLC receiver is more sensitive than the state-of-the-art 3 mm^2 APD (AD1900-9-TO5i). Moreover, theoretical results in [50] show that the SPAD-based VLC receiver requires only 14% of photon detection efficiency (PDE) to match the performance of the state-of-the-art APD. Furthermore, it has been suggested that an array of SPADs of an active area larger than a square millimetre and PDE greater than 40% can provide a sensitivity significantly higher than a receiver based on an APD. Table 1.1 evident that a 9.4 mm^2 SiPM-based VLC receiver is significantly better at every data rate when compared to receivers based on an APD and PIN photodiode [14], [45].

1.5 Aims and objectives of the project

The project aims to characterise a range of silicon photomultipliers, evaluate and compare their performance, and study their results to develop a model that can be used to accurately predict the performance of a silicon photomultiplier when used as a VLC receiver. The characterisation include the measurement of various parameters of a SiPM, such as bias-dependent dark count rate and PDE, linearity, effective recovery time, and bandwidth. Similarly, the performance evaluation involves the measurement of the irradiance required by a SiPM to achieve a particular BER at a range of data rates with different modulation schemes and when operating in the dark and ambient light. Moreover, the performance evaluation involves when a SiPM's parameters

vary, such as its active area, linearity, effective PDE, and bandwidth. The project also involves studying the impact of various parameters of a SiPM on its performance and the development of a model that can be used to predict the performance of a SiPM-based VLC receiver in various operating conditions.

1.6 Summary

This chapter discusses an overview and basic components of optical wireless communication and its need. Optical wireless communication has the potential to augment existing RF systems to fulfill the demand for high-speed data transfer and an increased number of wireless devices. However, fast and sensitive receivers at all wavelengths are required for optical wireless systems. Until recently, most of the sensitive and high-speed receivers are based on silicon, which means their sensitivity is high only in the visible band. Therefore, the chapter mainly discusses the background and challenges associated with VLC receivers. The challenges include finite bandwidth, dynamic range and FOV of the receiver, and also a limit on the level of irradiance from transmitter due to the safety of the eye or skin. Therefore, sensitive receivers are required for the communication. However, a highly sensitive receiver means that the receiver will be susceptible to background light. Therefore, optical interference filters can be used to deal with the background light. Although interference filters can substantially reject the background light, which depends upon their bandstop properties, and allow transmission of a particular wavelength, their spectral properties vary significantly when the incident angle is not normal. Hence, the FOV of the receiver is limited with these types of optical filters. As a result, it is difficult to have a wide FOV and to reject the background light while maintaining the sensitivity of the receiver. Moreover, the impact of the detector's active area on the bandwidth is also discussed. Both detectors' active area and bandwidth have a trade-off and may directly impact the sensitivity of a receiver.

The chapter also discusses the recent trend of various VLC receivers incorporating APDs, PIN, and an array of single-photon detectors. Comparatively, SiPMs perform better and are more

sensitive than APD and PIN photodiode-based VLC receivers. However, numerous factors, such as finite bandwidth and dynamic range, effective PDE, and optical interference, can significantly influence the performance of a SiPM. These factors have been studied throughout the thesis.

Chapter 2

Background of a VLC Receiver

2.1 Introduction

This chapter explains the basics and working principles of single-photon avalanche diodes and an array of single-photon avalanche diodes and their important characteristics, such as output signal, quenching mechanism, photon detection efficiency (PDE), and inherent noise. Subsequently, theoretical models are discussed, which describe the behaviour of an ideal photon-counting receiver in terms of average required photons per bit from a transmitter with and without background count per bit taken into account to achieve a particular BER. An impact of various BER values on the average required photons per bit, a relationship between the bandwidth and data rate to the inter-symbol interference (ISI) and power penalty, the impact of cool and warm white LED as a background light, and the selection of a wavelength for transmission are also discussed in this chapter.

2.2 Basics of a single photon avalanche diode

As discussed in the previous chapter, APDs have been widely used in VLC systems. However, the avalanche multiplication creates a gain-dependent excess noise, which limits its gain around up to a few hundred [22], [23], [51]. This limitation in the gain can be avoided by biasing an APD above its breakdown voltage, which allows the diode to create a self-sustained avalanche multiplication. The process of avalanche multiplication increases the gain of the APD to typically 10,000 [52]. An APD operating above its breakdown voltage is often referred to as Geiger-mode APD (GM-APD), which is sensitive enough to detect photons down to a single photon and hence, is also referred to as single-photon avalanche photodiode (SPAD).

To understand the operation of a SPAD, an equivalent circuit of a single-SPAD element model is shown in Figure 2.1 (a) developed by McIntyre (1961) and later Haitz (1964) [53] can be used. The equivalent circuit consists of a capacitor C_J, a voltage source V_{BR} (breakdown voltage of the APD), and a series resistor R_S, which is the total resistance of undepleted regions in an APD [53]. The R_S depends upon the bias applied to the SPAD element. When no bias is applied, R_S is on the order of several hundred ohms, however, when a bias voltage is applied to the SPAD, it reduces to tens of ohms. Now assume that a bias voltage (V_{BIAS}) of greater than V_{BR} is applied, in the event when there is no photon incident or avalanche event occur, the switch 'S' in the circuit model will remain open and the C_J will be charged to V_{BIAS}. Where V_{BIAS} is ΔV volts higher than

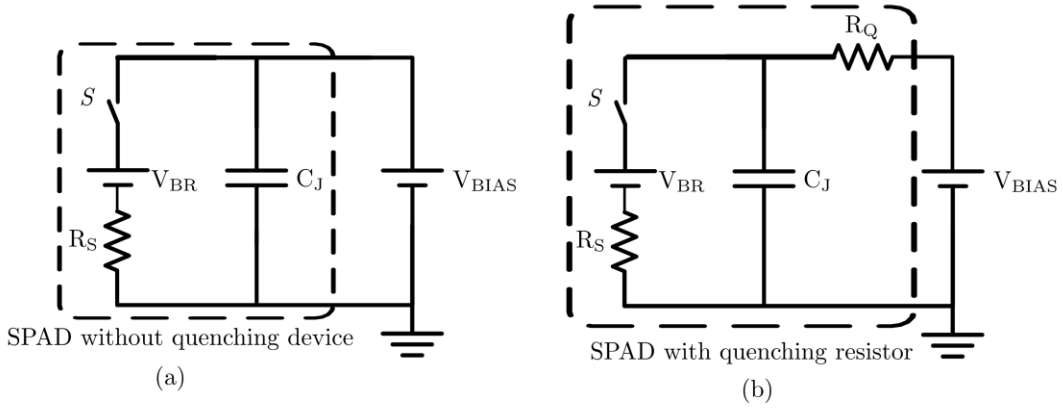


Figure 2.1 Equivalent circuit of a basic single SPAD element (a) and a SPAD with quenching resistor (b)

the V_{BR}. The term ΔV typically known as overvoltage. However, when an avalanche event occurs, the switch 'S' in the equivalent circuit will be close and in this case, the capacitor C_J begins to discharge through R_S. As a result, the effective voltage across the APD will be reduced [53]. However, a current $(\frac{\Delta V}{R_s})$ continue to persist across the APD due to APD being biased with a constant voltage source. To avoid this situation and to recovery the APD to its sensitive state, the avalanche process need to be quenched [53]. Typically, there are two types of quenching mechanism that can be used to quench an avalanche event known as active quenching and

passive quenching [26]. The active quenching may involve a complex circuitry to record or count the number of avalanche event(s) occurred in a particular time. Whereas, the passive quenching can be implemented using just a single component such as resistor in series with a SPAD element. Mostly, all commercially available SiPMs are incorporating passive quenching mechanism in their SPAD elements.

Figure 2.1 (b) show that a resistor (R_Q) is added in series to SPAD element (shown in the dashed-line box), which act as a quenching circuit. When a photon is absorbed or an avalanche event occurs, C_J begins to discharge through R_S, and hence the effective bias across the APD will be reduced and a voltage drop across R_Q. Figure 2.2 shows an example of current pulse when

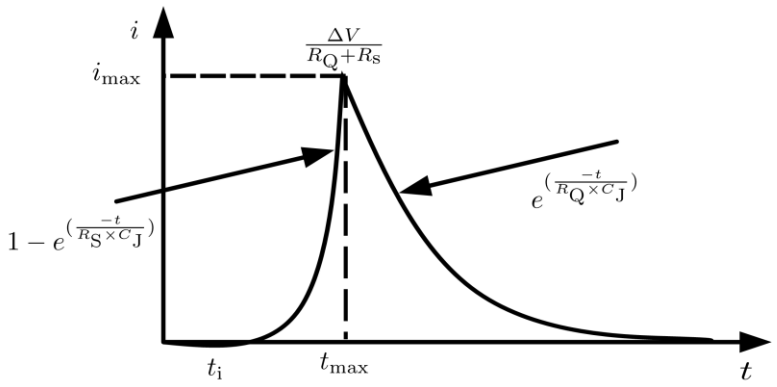


Figure 2.2 Example of current flowing through a SPAD element as a function of time. The pulse is asymmetric around $t = t_{max}$ because of $R_Q \gg R_S$

an avalanche event occurs. It can be seen at $t = t_{max}$, the current reaches to its maximum value ($I_{max} = \frac{\Delta V}{R_Q+R_S} \approx \frac{\Delta V}{R_Q}$) in a time constant $\tau_r = R_S \times C_J$ known as the rise time. Similarly, the trailing edge shows that the process is quenched at the same time i.e. $t = t_{max}$ and the capacitance will be recharged again to V_{BIAS} so that the APD recover itself to its sensitive state. The recharge time constant is given as $\tau_f = R_Q \times C_J$ [54], [55].

A single SPAD can be used as a VLC receiver, however, as discussed earlier, it requires a finite interval of time to restore itself to a sensitive state. Typically, the recharge time constant of some commercial single-photon modules is in the order of a few tens of nanoseconds [24], [56]. Since even an ideal photon-counting receiver requires a few photons per bit to detect, therefore, the data rate, in this case, would be limited with a single SPAD. However, this limitation can be overcome by using multiple SPAD elements or an array of SPAD, which gives an advantage of detecting multiple photons at a single instant of time. A SPAD element often referred to as a microcell when an array of SPAD element is used with a name of SiPM. The next section discusses the basics of a SiPM.

2.3 Basics of a SiPM

A SiPM consists of multiple microcell connected in parallel, where each microcell is identical and consists of a series combination of a basic SPAD and a quenching resistor R_Q. Figure 2.3 shows an equivalent circuit model of a typical SiPM. Assume that the SiPM is biased above its breakdown voltage and all the switches in the equivalent circuit are open when there is no avalanche event occurs. However, as soon as a photon is incident on a microcell or an avalanche event take place, the switch 'S' is closed and the output current begins to flow through the

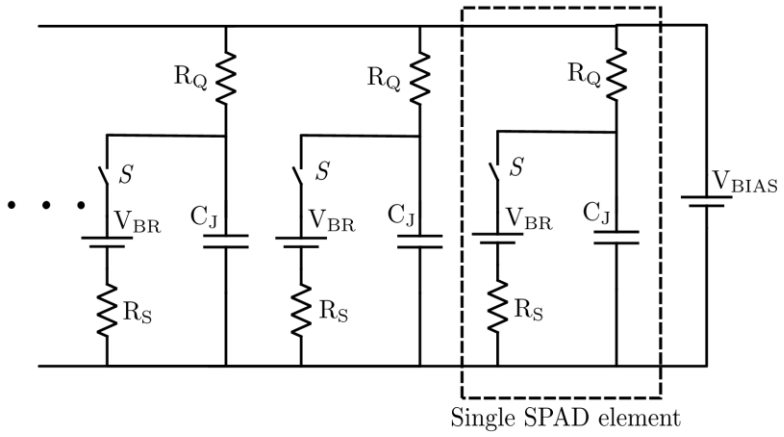


Figure 2.3 Equivalent circuit of a SiPM biased with an external voltage source V_{BIAS}. The dashed box shows single microcell consists of a basic SPAD and a quenching resistor R_Q.

terminals of the SiPM. Subsequently, the avalanche process is quenched and the microcell recovers back to its sensitive state. As discussed in the previous section, the recovery of a microcell takes a finite interval of time often known as recovery time. Ideally, during this time, the microcell is insensitive to any photon. The recovery time is an important parameter, which determine the sensitivity of a SiPM. A longer recovery of a SiPM may result in poor sensitivity.

In a case when two or more photons concurrently trigger an avalanche in different microcells, the current flowing through terminals of a SiPM will be the sum of the current produced by avalanche effect in different microcells. However, if a single microcell absorbs two or more photons at the same, then the resulting current pulse will be identical to the current produce by a single microcell when it absorbs a single photon. Moreover, it is important to note that that the recovery time of a microcell in a SiPM may differ from the recovery of time of single SPAD as the parasitic capacitance associate to tracks, which connect all the microcells together may significantly impact the recovery time. When a microcell of a SiPM recovers from an avalanche event, C_J tends to recharge to V_{BIAS}. This means that during this recharging process, the current will also flow across the junction capacitor of all other microcells. The latter current tends to lowering V_{BIAS} on the other microcells until the value is completely reaches equal V_{BIAS} on the recovering microcell, which eventually means that, all the microcell recharge together to V_{BIAS} [57].

2.3.1 Noise components of a SiPM

When a thermally generated charge carrier triggers an avalanche event in microcells of a SiPM, SiPM generates noise components. The noise in a SiPM is produced in the form of output pulses per unit of time even when there is no light incident on its active. To measure noise components of a SiPM, SiPM is required to be operated in the dark condition, which allows a faster evaluation of its noise. The noise of a SiPM imposes a limit on the minimum detectable count rate when a SiPM is illuminated with light [54]. A SiPM may has two type of noise components. The first is the

primary noise often referred to as dark counts and the secondary noise include optical cross-talk (CT) and after-pulsing (AP). The dark counts of a SiPM is determined by the number of avalanche events occurred per unit of time caused by thermally generated charge carriers in a microcell and typically known as dark count rate (DCR). The dark count rate scales according to the SiPM area and increases with applied bias [57], [58]. A dark count is indistinguishable and uncorrelated to pulse produced by a photo-generated event. Similarly, the cross-talk (CT), which is the secondary noise component, may take place in two different ways. The first is the direct-cross-talk (Direct-CT) in which an avalanche event produced in one microcell result in an electro-luminescent emission of a photon (by recombination of an electron-hole pair) [54] that can trigger the avalanche in an adjacent microcell simultaneously. These two simultaneous avalanches in adjacent microcells may results in an amplitude of output pulse twice the amplitude of output pulse produced by a single avalanche. For silicon, the wavelength of the photon produced by cross-talk lies within the range of 450 nm and 500 nm [57], [59]. The second is the delayed-CT, which is also the secondary noise and involves photons that are re-absorbed in the inactive regions of a SiPM. The electron or hole generated through this process must then diffuse to the active region of a cell before being able to trigger an avalanche. The pulse produced is correlated and therefore has a certain time-delay of the order of few ns compared to the original pulse [57]. The after-pulsing (AP) is also the secondary noise components. The after-pulsing effect is related to charge carriers trapped in the silicon lattice defects during the avalanche multiplication and then released with a statistical fluctuation delay or may release during the recharge phase of a microcell. The amount of charge released in an after-pulse depends on the time delay between the primary and secondary avalanche [57].

2.3.2 Photon detection efficiency

The photon detection efficiency of a SiPM is an important optical characteristic, which determine the ability of a SiPM to detect the number of photons per unit of time against the number of photon

incident over its active surface. The PDE of a SiPM slightly differ from the conventional quantum efficiency (η) due its microcell structure [60]. The PDE is the statistical probability that an incident photon interact with a microcell to trigger an avalanche and is the product of the quantum efficiency (η) of the SiPM and the avalanche probability ($P_{avalanche}$) as [60], [61].

$$PDE = \eta(\lambda) \times P_{avalanche}(\Delta V) \tag{2.1}$$

Where the quantum efficiency is the function of wavelength of the incident light and microcell fill factor (FF) and is expressed as [61]

$$\eta(\lambda) = FF \times (1 - R_F)[1 - e^{-a1 \times x}] \tag{2.2}$$

The fill factor represent the geometrical dimension of a microcell and refers to the percentage of the microcell active area that is sensitive to the light. The area of a microcell, which is insensitive to the light is used by the quench resistors and signal track known as the dead space. A high fill factor means that the microcell has a large active-region/space-charge-region and higher probability of detecting photons, thus, resulting in a higher PDE [61]. However, a large active area also results in higher capacitance, which means longer recovery times and also a limited dynamic range. R_F in Equation 2.2 is the reflection coefficient, which is negligible due to the anti-reflection (AR) coating on the SiPM, a_1 is the absorption coefficient, and x is the absorption path length or absorption depth [61]. Similarly, $P_{avalanche}$ in Equation 2.1 is the function of the relative overvoltage (V_{rel}) and is expressed as [58], [62], [63]

$$P_{avalanche}(\Delta V) = \left(1 - e^{\frac{-v_{rel}}{\alpha_2}}\right) \tag{2.3}$$

where a_2 is the parameter, which is device and wavelength specific [63]. This means that the PDE of a SiPM is also depends upon the avalanche triggering probability ($P_{avalanche}$) that triggers an

avalanche event, which strongly depends on the value of overvoltage (ΔV) applied at the SiPM [62].

2.4 Optical receiver for communication

The performance an optical receiver for communication depends upon the number of bits, which are received correctly against the number of transmitted bits. An error occurs when a transmitted bit is not received correctly; therefore, an erroneous bit is required to be re-transmitted, degrading the receiver's performance. For an on-off keying (OOK) modulation, the probability of transmitting a logic '0' and logic '1' is equal. Hence, in this case, the probability of error or the bit error rate (BER) can be expressed as [26], [62], [64]

$$BER = \frac{1}{2}[p(R0|T1) + p(R1|T0)] \tag{2.4}$$

where $p(R0|T1)$ is the probability of receiving a logic '0' when a logic '1' is transmitted. Similarly, the $p(R1|T0)$ is the probability of receiving logic '1' when a logic '0' is transmitted.

2.4.1 Receiver with no background and bit error rate

A noiseless on-off keying optical receiver counts the number of photons per bit. Following the concept from Equation 2.4, the receiver counts the number photons in a duration of bit T_b when a logic '1' is transmitted. If the receiver count no photons within the duration of a bit, then this means that either a logic '0' is transmitted or photons corresponding to logic '1' have been missed. Therefore, the probability $p(m)$ of generating m number of electron-hole pairs by an ideal optical receiver with in a duration of bit when a logic '1' is transmitted follows Poisson statistics [62], [64]

$$p(m) = \frac{n_s^m . e^{-n_s . T_b}}{m!} \tag{2.5}$$

Where n_s is the number of photons per bit required by the receiver in a duration of bit when a logic '1' is transmitted. However, in the case when the receiver is noiseless, no photons are detected

by the receiver, which means that the transmitter is completely turned-off or transmit no light when a logic '0' is transmitted and also there are no background or dark counts are present. Therefore, in this case, the probability $p(R1|T0) = 0$ and the BER, which is calculated using Equation 2.4 and 2.5 as [64], [65]

$$BER = \frac{1}{2}[p(R0|T1) + 0] = \frac{1}{2}e^{-n_s.T_b} = \frac{1}{2}e^{-n_s.T_b} \quad (2.6)$$

Equation 2.6 is called the quantum limit, which is a common measure of the sensitivity of an optical receiver to achieve a particular BER. Moreover, it can be noticed that the BER has an exponential relationship to the required number of photons per bit (n_s). A small increase in n_s may

BER	n_s	BER	n_s
10^{-3}	6.2	10^{-8}	17.7
10^{-4}	8.5	10^{-9}	20
10^{-5}	10.8	10^{-10}	22.3
10^{-6}	13.1	10^{-11}	24.6
10^{-7}	15.4	10^{-12}	26.9

Table 2.1 The average number of photons (n_s) required by a noiseless optical receiver to achieve various BERs

significantly impact the BER as shown in Table 2.1.

Furthermore, from Table 2.1, it can be noticed that to achieve a lower BER value such as less than 1×10^{-9} or 1×10^{-10} at which data transmission is considered to be error free [44], [66], a receiver requires more than 20 photons per bit. However, to achieve a BER of 1×10^{-3}, only 6.1 photons are required by the receiver, which is 30% of the photons required per bit to achieve a BER of 1×10^{-9}. The advantage of using a higher BER value is that a fewer photons are required to detect by the receiver, and forward error correction (FEC) is a technique, which has the capability to control errors in data transmission over a channel. FEC typically uses two structurally different codes, which are in common use such as block codes and convolutional codes [67]. Reed-Solomon is a popular error correcting codes, which is a type of block codes and able to correct $t = (n - k)/2$ symbol errors of n-symbol long codeword, where each symbol is of q bits long, k is the number of data symbols, and the code rate is k/n. RS(255,239) is well-known code

standardized in ITU-T G.975 and G.709 [68], where n = 255, k = 239, t = 8 and q = 8. The rate

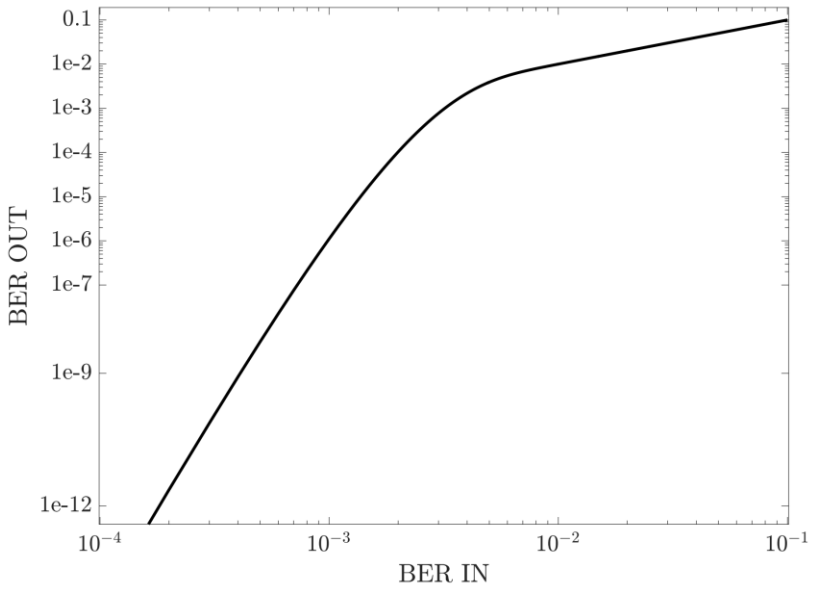


Figure 2.4 Performance of RS (255,239) decoder capable of correcting eight symbol errors

is 239/255 = 0.94 and the overhead is 16/239 = 6.7% [69]. The error rate at the output as a function of BER at the input of the RS (255,239) decoder is shown in Figure 2.4 estimated from [69].

The effect of various BER values can be assessed by the quality of an image or a video transmission as describe in Table 2.2. Table below shows the quality of a JPEG and compressed sensing (CS) encoded image [70], a 640×480 pixels, 25 frame per second (fps), and H.264 encoded video [71], a HD 4k uncompressed video [66], and a H.265 video [72], [73] at a BER values(s). From Table 2.2, it can be concluded that an excellent image quality when CS encoded, and a good quality video with either H.264 or H.265 encoded can be achieved when the BER is 1×10^{-4}. However, RS(255,239) FEC in Figure 2.4 suggests that when the input BER is 1×10^{-3} at the decoder, a BER of 1.1×10^{-6} can be achieved at the output, which is much lower than the BER of 1×10^{-3}, required to ensure a transmission of good quality image or a high-resolution video.

Image/Video (Type)	Data Rate	Quality	BER	Reference
Image (JPEG)	-	Average	1×10^{-5}	[60]
		Poor	1×10^{-4}	
		Degraded	1×10^{-3}	
Image (Compressed Sensing)		Excellent	1×10^{-5}	
		Excellent	1×10^{-4}	
		Good	1×10^{-3}	
MPEG-4 (480p, 25 fps) (H.264)	1.15 Mbps	Excellent	$< 10^{-4}$	[61]
		Good	1×10^{-4} to 4×10^{-4}	
		Satisfactory	4×10^{-4} to 8×10^{-4}	
		Poor	8×10^{-4} to 1×10^{-3}	
		Very Poor	$>1\times10^{-3}$	
HD 4k (Uncompressed)	5.5 Gbps	Excellent	$< 1\times10^{-10}$	[56]
Full HD (1080p, 50 fps) (HEVC/H.265)	5 Mbps	Good	1×10^{-4}	[62], [63]

Table 2.2 Relationship between quality and BER of an image and a few video formats

2.4.2 Receiver with background

In addition to the number of required photons per bit, an optical receiver detect background counts in the presence of an ambient light, which may also include dark counts generated inherently by a detector at both events i.e. when a logic '0' and logic '1' is transmitted. Hence, a decision is required in this case between the number of counts received at logic'1' and at logic '0' to distinguish received 1s and 0s. For a photon counting receiver, this decision is based on a threshold number n_T. If the number of counts per bit (n) is greater than n_T, then the received bit will be perceived as a logic '1', otherwise the bit will be perceived as logic '0'. An error occurs when a transmitted bit is logic '1' and it is perceived as logic '0' or vice versa. If n_b denotes the number background counts per bit, then Equation 2.4 can be re-written to calculate the BER as [26], [74]

$$BER = \frac{1}{2}\left[p(n < n_T|T1) + p(n > n_T|T0)\right] \tag{2.7}$$

where $p(n < n_T|T1)$ is the error probability of transmitted bit '1' for being detected bit '0, and $p(n > n_T|T0)$ is the error probability of bit '0' for being detected as bit '1'. During transmission of bit '0', only the background counts are detected by the receiver. Whereas, when bit '1' is transmitted, then the total number of counts detected by the receiver will be the sum of the number of signal photons n_s from the transmitter and the number of background counts n_b. This means that the number of background counts will always be present regardless of transmitted bit [26]. The BER in this case is expressed as [26], [62]

$$BER = \frac{1}{2}\left[\sum_{k=0}^{n_T} \frac{(n_s+n_b)^k}{k!}.e^{-(n_s+n_b)} + \sum_{k=n_T}^{\infty} \frac{(n_b)^k}{k!}.e^{-n_b}\right] \quad (2.8)$$

Figure 2.5 shows the average number of signal photons required per bit from the transmitter (solid line) as a function of the background counts per bit based on Poisson statistics (Equation 2.8).

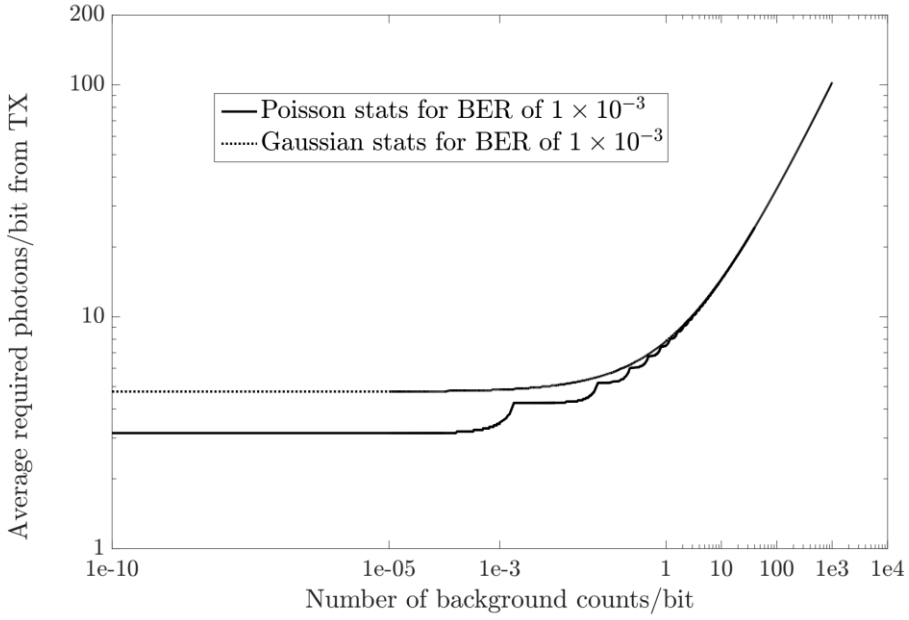


Figure 2.5 The average number required photons per bit at a range of background counts per bit to achieve a BER equals to 1×10^{-3}

From Figure 2.4, it can be seen up to a certain limit of the number of background counts per bit i.e. when it is less than the one-fifth of the BER, no additional photons are required to maintain the BER or in other words, no power penalty is required. This also means that the average number

of signal photons per bit required from the transmitter is independent of the number background counts when it is significantly lower than the target BER [26]. For instance, the average number of signal photons per bit required in Figure 2.5 is 3.1 as long as the number of background counts per bit is less than the one-fifth of the BER i.e. 2×10^{-4}. However, as the number of background counts crosses this value, a steeper rise in the average number of signal photons per bit can be seen, which is due to the change in the threshold number (n_T). It is important to note that despite this trend, the average number of signal photons per bit required from the transmitter increases less rapidly than the number of background counts. For instance, even at 1000 background counts per bit, it is required only 102.5 signal photons from the transmitter to achieve a target BER of 1×10^{-3} as can be seen in Figure 2.5. This suggests that a SiPM with a large detection area is a suitable choice as long as this trend is maintained.

Furthermore, Figure 2.5 also shows the average number of signal photons required per bit from the transmitter (dotted line), which is based on the Gaussian approximation, and is described as [52], [75]

$$BER = \frac{1}{2} \times erfc\left[\frac{n_1 - n_T}{\sigma_1\sqrt{2}}\right] \tag{2.9}$$

where, $n_T = \frac{n_b\sigma_{1+}n_1\sigma_0}{\sigma_{1+}\sigma_0}$, σ_0 and σ_1 are the standard deviations of received '0s' and '1s' respectively. The $\sigma 0 = \sqrt{n_b}$ and $\sigma 1 = \sqrt{n_1}$, n_1 is the sum of the average number of signal photons per bit (n_s) required from the transmitter and the number of background counts per bit (n_b). From Figure 2.5, it can be seen that the flat region where the number of background counts bit is less than 2×10^{-4} (one fifth of the target BER), the Gaussian approximation significantly overestimates the average number of photons per bit by a factor 1.5. However, as the number of background counts increases over 1 per bit, the Poisson and Gaussian statistics start to converge and are indistinguishable at a few tens of the number of background counts per bit.

2.5 Bandwidth, data rate, and inter-symbol interference (ISI)

In VLC systems, like noise and background counts, the bandwidth of a receiver may also negatively impact on its sensitivity. For a given data rate (R_b), as a rule of thumb, the optimum 3 dB bandwidth (BW_{3dB}) of an OOK receiver should is about 60 to 70% of the data rate [76]. Conversely, the data rate is a factor of 1.5 the optimum 3 dB bandwidth. However, if the data rate is higher than this factor, ISI starts to impact the system and the signal swing will be reduced. The ISI is the distortion in the transmitted signal due to the limited bandwidth of the channel. For instance, Figure 2.6 (i) shows examples of an OOK signal transmitted to a receiver with an infinite bandwidth (a) and with finite bandwidth (b). The values (white dots) of the signal sampled at the

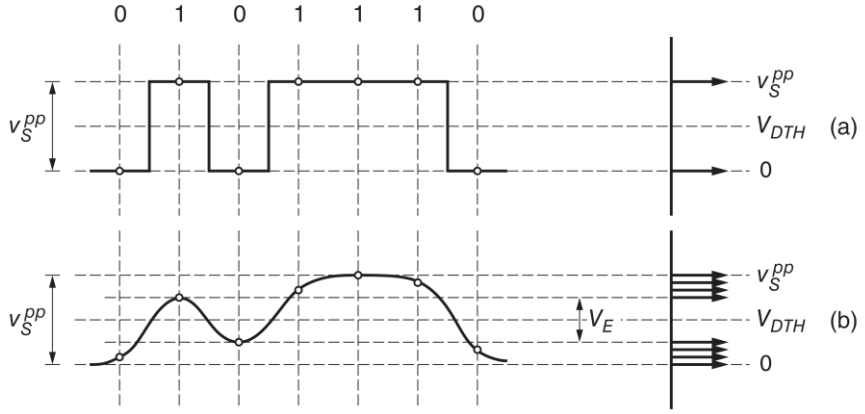


Figure 2.6 Example of an OOK signal received at the output of the receiver with infinite bandwidth (a) and finite bandwidth (b). The receiver with finite bandwidth clearly shows the impact of ISI

output of the receiver with finite bandwidth (Fig. 2.6, b) clearly shows that these do not only depend on the current bit (or symbol) but also on the bits, before and after the current bit [77]. Whereas, in the case of the receiver with an infinite bandwidth, values sampled at the output are undistorted, and their histogram shown on the right (Figure 2.6, a). The distortion in the received signal due to the ISI results in the BER being compromised.

A power penalty (PP) will be required to maintain the original or target BER. For a single-pole low-pass system, assuming the full swing is normalised to 1, the power penalty in this case is [76]

$$PP = 10 \times \log_{10}\left(\frac{1}{1-2\times exp\left(\frac{-2\times\pi\times BW_{3dB}}{R_b}\right)}\right) \tag{2.10}$$

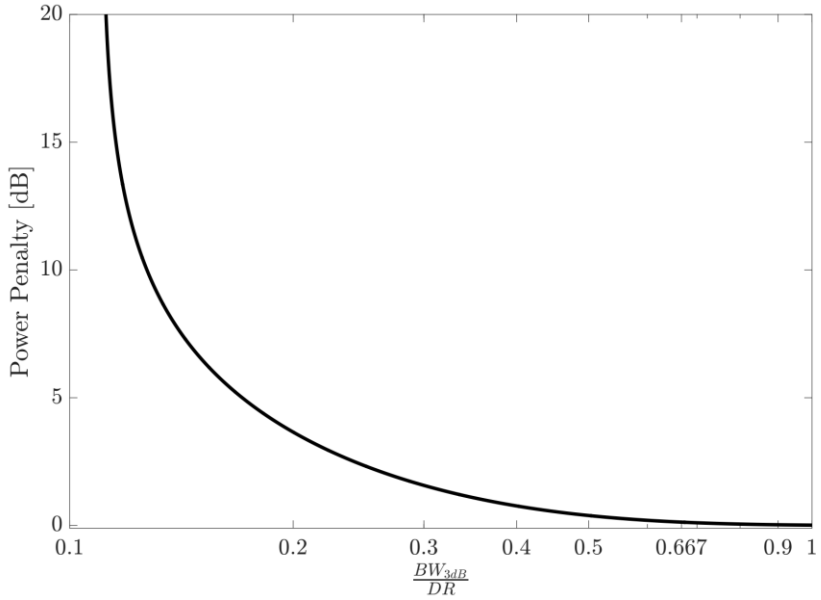


Figure 2.7 Power penalty required by a single-pole low-pass system vs. the ratio of 3 dB bandwidth to data rate

where PP is in decibel (dB). Figure 2.7 shows the relationship of PP to the 3 dB bandwidth and data rate. From Figure 2.7, it can be seen as long as the ratio of 3 dB bandwidth to data rate is below two-third (2/3), the power penalty is negligible. However, the power penalty is more than 0.5 dB when the ratio is below 0.5 and then rapidly increases as the ratio decreases further. This suggest that the signal needs to be equalised in order mitigate the impact of ISI so that the power penalty can be avoided. The process of equalisation filters out ISI or reversal the signal distortion incurred by the finite bandwidth of the system [76], [78].

2.6 Communication Scenario

A VLC system should be workable in the presence of ambient light in an indoor environment. Typically, an indoor environment may include a normal office, study library, common room, show room, check-out area, kitchen and an auditorium. The recommended illuminance required in such indoor environments is equal to 500 lux [79]. Since white LEDs are being most widely used in indoor environment due to their many advantage such as long-life, low-cost, low heat emission, and low-power consumption [80]. Therefore, spectra of two widely used white LEDs have been considered and are shown in Figure 2.8. From Figure 2.8, it can be seen that there are two regions where both white LEDs have relatively a negligible intensity. The first region is wavelengths

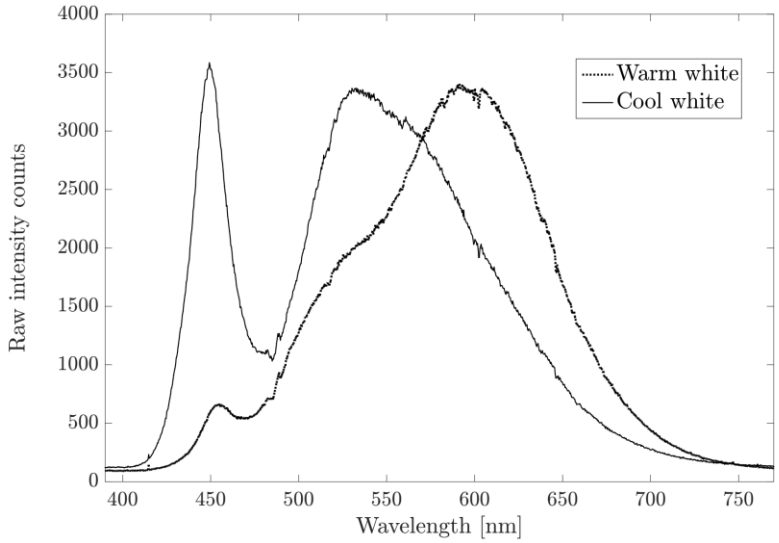


Figure 2.8 Spectrum of warm (dotted line) and cool (solid line) white LED lamp (Philips IBRS) measured using ocean optics SD2000 spectrometer

shorter than 410 nm and the second region is wavelengths longer than 750 nm. However, at longer wavelengths, the photon detection of efficiency of silicon-based detectors is low [54]. Whereas, silicon-based detectors show better sensitivity at shorter wavelengths [63], [81], [82]. Therefore, on the basis of sensitivity of silicon-based detectors and negligible intensity at shorter wavelength, it can be decided that the transmission of data at around 400 nm is an appropriate choice.

2.7 Summary

In this chapter, basics of a single photon avalanche diode (SPAD) is explained, which can be used as a photon counting receiver in VLC systems. However, a single SPAD element has a limitation that it require a finite interval of time to recover itself after when it detects a photon. The time required to recover a SPAD often referred to as recovery time, which poses a limit on the achievable data rate and the target BER. By using an array of SPAD elements allows to detect multiple photons at a single instant of time and hence the limit of achievable data rate can be increased. However, in practice, increasing SPAD elements associated to non-ideal effects such as dark counts, after-pulsing and cross-talk, which have been discussed in section 2.3.1 may significantly impact the sensitivity of the receiver. The chapter also discusses the Photon detection efficiency, which is an important factor to determine the sensitivity of a receiver. In Section 2.3.2, a model is also presented, which can be used to predict the photon detection efficiency of a detector, and discusses its dependence on fill factor, overvoltage and avalanche probability, and wavelength.

The error probability of a basic OOK receiver has been discussed in section 2.4. In particular, the performance of OOK receiver in terms of its sensitivity or the number of required photons per bit to achieve a BER, the performance of Reed-Solomon encoder i.e. RS(255,239) for error correction and a few example of acceptable BER in various systems are discussed. However, in addition to non-ideal effects associated to an array of SPAD or SiPM, the background counts from an ambient light may also degrade the performance of the receiver, which has been discussed in Section 2.4.2. Moreover, a model is presented, which predicts additional photons per bit required by the receiver to maintain a target BER at a range of background counts per bit. Results obtained from the model show the trend of the average number of signal photons per bit required from the transmitter and suggest that a SiPM, which covers large area can perform better. However, as discussed earlier, increasing the number of microcell in a SiPM result in

increasing the non-ideal effects and may also introduce parasitic capacitance associated to grid or tracks connecting the microcells. These parasitic may significantly impact the bandwidth and sensitivity of the receiver, which has been discussed in section 2.5.

At the end of this chapter, a few examples of indoor environment are presented, where white LEDs are being used widely for illumination. These white LEDs may act as an ambient light source to VLC systems. Therefore, cool and warm white LED spectra with respect to their impact on VLC systems at different wavelengths have been discussed in section 2.6 and it has been concluded that transmitting data at around 400 nm is an appropriate choice due to high sensitivity of silicon-based detector and negligible impact of white LEDs at this wavelength.

Chapter 3

Characterisation of Silicon Photomultipliers

3.1 Introduction

In recent years, silicon photomultipliers (SiPMs) have become attractive optical sensors in many low light applications because of their unique features such as compared to the photo-multiplier tubes (PMTs), SiPMs consume low power and require low-voltage operation, insensitivity to the magnetic field, compact and capability to work at room temperature. SiPMs can potentially be used in applications involving single or a few photon detections such as spectroscopy, visible light communications, quantum experiments and distance measurement applications such as LIDAR.

As discussed in section 2.3, a silicon photomultiplier (SiPM) consists of a matrix of Geiger-mode avalanche photodiodes (GM-APDs), connected in parallel, which are often referred to as microcells of a SiPM. Each microcell is biased above its breakdown voltage, which is sensitive enough of detecting photons down to a single photon. When a photon is absorbed by a microcell, it triggers the Geiger discharge, which results in a current. This current is then converted to a voltage pulse using a load resistor. However, when multiple photons are absorbed by individual microcells, the current from each microcell is added together and is proportional to the number of microcells active simultaneously. An ideal SiPM has characteristics such as a large collection area, PDE equal to 100% at all wavelengths, a narrow output pulse width, no dark count rate, and lowest recovery time. However, in practice, there are numerous factors are involved, which introduce limitation to these characteristics.

The aim of this chapter is to survey various state-of-the-art commercial-off-the-shelf SiPMs, which can be used a sensitive receiver for visible light communication, discuss the criteria of selecting a SiPM and present methods of experiment for characterisation of various parameters

of a SiPM. The characterisation include bias-dependent dark count rate and photon detection efficiency, the shape of the output pulse and recovery time, dynamic range, and effective PDE. Moreover, different analytical models have been discussed and compared to the measured characteristics of a SiPM. These analytical models can be useful to predict the performance of a SiPM for applications such as visible light communications.

3.2 Off-the-shelf SiPMs

Silicon photomultipliers are relatively new type of photodetectors, which represents a new step in the development of the modern silicon-based detection structures. Typically, SiPMs are sensitive in the visible light spectrum. However, modern SiPMs are now provide increased sensitivity, reduced non-idealities and superior timing performance into the red and NIR region of the electromagnetic spectrum [83]. The performance of these modern SiPMs are comparable to other solid-state photodetectors such as APDs and PIN diodes.

Table 3.1 summarses, some commercially available state-of-the-art SiPMs from different manufacturers such as onesmi$_{TM}$, Hamamatsu, AdvanSiD, KETEK GmbH, and First Sensor are listed in Table 3.1. These SiPMs have been mainly surveyed for their potential as a sensitive VLC receivers. The important key parameters, which need to be considered are active area, microcell fill factor, photon detection efficient, dark count rate, the total number of microcells, RC time constant, and output pulse have been compared.

Manufacturer	First Sensor (NUV3S-SMD)	Hamamatsu (S13361-3050)	AdvanSiD (ASD-NUV3S-P)	KETEK (PM3325-EB)	onsemi$_{TM}$ J-Series 30035	onsemi$_{TM}$ J-Series 60035
Physical Parameters						
Active area (m^2)	9×10^{-6}	9×10^{-6}	9×10^{-6}	9×10^{-6}	9.4×10^{-6}	36.8×10^{-6}
Microcell fill factor (Microcell size)	60% (40 µm)	74% (50 µm)	60% (40 µm)	- (25 µm)	75% (35 µm)	75% (35 µm)
Number of microcells	5520	3600	5520	13408	5676	22292

Performance Parameters						
Peak PDE (%)	43@420nm	40@450nm	43@420nm	34@430nm	50@420nm	50@420nm
Dark count rate (Mcps)	0.5@2V_{ov}	0.5 (Typ.)	0.5@2V_{ov}	2.2@2.5V_{ov}	0.5@2.5V_{ov}	1.9@2.5V_{ov}
Microcell RC time (ns)	70	40	70	40	45	50
FWHM Output pulse width (ns)	25	25	25	-	1.5 (Fout) 30 (Sout)	3 (Fout) 50 (Sout)
Breakdown voltage (V)	26	53	26	25	24.5	24.5

Table 3.1 Performance parameters of various commercial SiPM modules (First Sensor, Hamamatsu, AdvanSiD, KETEK and onsemi$_{TM}$)

While comparing performance parameters such as PDE, onsemi$_{TM}$ SiPMs have higher PDE in the blue region compared to other SiPMs in the table. First Sensor and AdvanSiD exhibit a higher recovery time among other SiPMs in the table. Similarly, when comparing the dark count rate, SiPMs of the same size have almost the same rate except KETEK, which has a dark count rate more than 4 times the dark count rate exhibit by other SiPMs. A unique feature of onsemi SiPMs is their dual-mode readout, which shows that the signal from their fast readout (Fout) has a pulse width (FWHM) is significantly smaller than the signal from their standard readout (Sout). Whereas, other SiPMs listed in Table 3.1 has no such feature. Therefore, based on a higher PDE, low dark count rate and fast readout feature, onsemi J-series SiPMs have been selected in this work to evaluate the performance of these SiPMs as sensitive VLC receivers.

3.3 onsemi$_{TM}$ J-Series SiPMs

The microcell of onsemi$_{TM}$ J-Series SiPMs is based on high-volume and P-on-N silicon structure, which allows these SiPMs to achieve a PDE of 50% in the blue region and with sensitivity extending down into the UV region [84]. The J-Series SiPMs operate at lower operating voltages as compared to PMTs and APDs. It has an exceptional breakdown voltage uniformity of ±250 mV, low dark count rates of 50 kHz/mm^2 and provide excellent temperature stability [84]. The unique feature of onsemi SiPMs is their third electrode “fast readout terminal”, which is coupled to the

individual microcells through low capacitance capacitors as shown in the simplified schematic of Figure 3.1. The equivalent capacitance at the fast readout terminal is reduced by an order of magnitude and act as a high pass filter. Therefore, the signal collected from the fast readout terminal has a much shorter fall time than the signal collected from the standard readout. From Table 3.1 it can be seen that the full width half maximum (FWHM) of the signal collected from the fast readout is significantly smaller than the FWHM of the signal collected from the standard readout. The simplified schematic diagram also shows that a quenching resistor (R_Q) is connected

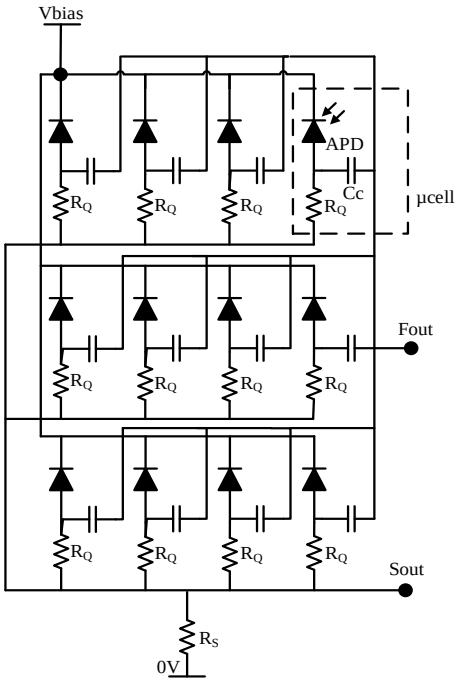


Figure 3.1 Simplified schematic of onsemi$_{TM}$ SiPM. Unlike standard SiPMs, each junction in the SiPM device has a connection to a third electrode with low capacitive coupling

in series with the microcell to quench the avalanche process and a resistor (R_S) in series with the SiPM. The standard readout terminal is connected across the resistor R_S. The resistor R_S plays an important role in recovering a microcell, which has been discussed in detail in application notes provided by onsemi$_{TM}$ [60].

3.4 Characterisation of J-Series SiPMs

onsemi$_{TM}$ provide two options to evaluate their J-Series SiPM sensors. The first option is the SMA biasing board and the second is the pin adapter board (SMTPA). However, their SMA boards have been optimised for best possible timing performance [84]. Therefore, the SMA board is preferred over SMTPA to characterise various parameters. The SMA board consists of three SMA connections. The first connection “Sout” is the standard readout terminal, second “Fout” is the fast readout terminal, and the third “Vbias” is the input to supply the bias voltage. Initially, MicroFJ-SMA-30035 has been characterised as the fast readout output pulse width is half the fast readout output pulse width of the 60035 SiPM. However, both SiPMs exhibit the same PDE, avalanche gain, and microcell fill factor except the recovery time, pulse width and dark count rate due to the difference in sensor size, total number of microcell and on board series resistance.

Figure 3.2 shows the block diagram of the experiment set up used to measure the dark count rate. When a typical bias voltage of 27 V is applied on MicroFJ-SMA-30035 board. A strong interference of RF signal from the WiFi device to the SMA board has been observed on the scope. Hence, to avoid external RF interference to the SMA board, the board has been fixed inside a box and EMF protection fabric is used.

3.4.1 Bias dependent dark count rate

In practice, a SiPM produces thermally generated free charge carriers even when there is no light is incident on the SiPM. These charge carriers trigger an avalanche event and as a result a pulse is generated known as dark pulse, which is indistinguishable from the pulse generated by photo-generated event. The thermally generated avalanche trigger has a finite probability and depends upon factors such temperature and the bias applied at the SiPM. The number of avalanche events or pulses produced per unit of time due these thermally generated charge carriers is the dark count rate (DCR). The dark count rate of a SiPM imposes a limit on the minimum detectable

counts when a SiPM is illuminated with light [54]. Moreover, the dark count rate also describe the minimum background count rate, which result in an extra number of photons per bit is required by the receiver. Thus, limit the receiver sensitivity.

In addition to RF shielding in the experiment, a BK5 blackout fabric (shown as the thin dashed line) is also used to cover the box and evaluation board to make sure that the SiPM is in the total dark. In the setup, a dual-channel variable dc power supply (GW Instek 3030D) is used to supply the bias voltage at the SiPM. The DCR has been measured from the fast readout of the SiPM follows Mini-Circuits® low noise amplifier (ZFL-1000LN+), which is required to amplify the output. The high definition scope (Lecroy HD6104-MS) is used to observe the output pulses, which is interfaced to the PC to capture the raw data.

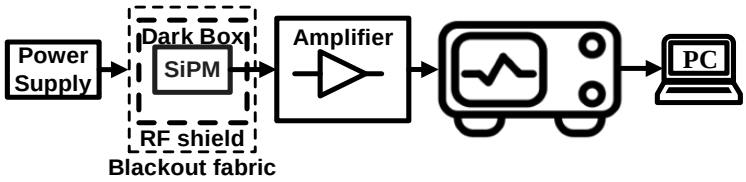


Figure 3.2 Experimental setup used to measure the average standard output pulse of the 30035 SiPM

To measure the DCR at different bias voltage applied at the SiPM, the bias voltage is varied from 25.5 V to 30.5 V. At each bias voltage, the raw data sampled by the scope at a sampling rate of 2.5 Gsps and 2.5 mega samples is first stored in the PC and processed offline using MATLAB® to calculate the number of pulses per unit of time.

Figure 3.3 (Top) shows an example of the raw signal captured from the fast readout of the 30035 SiPM when it is in the dark and operated at a bias voltage of 28 V. From the figure, it can be seen that pulses have different amplitude and well separated in time. To measure the dark count rate, individual pulse has been counted over a length of time. To count a pulse, a threshold is required, which separate the output pulse from the thermal noise present in the signal. For this reason, a histogram of the signal has been extracted shown in Figure 3.3 (Bottom). From the

histogram, it can be seen that the distribution, which has a mean equal to zero is the thermal noise and its occurrence towards positive amplitude is negligible/insignificant at around 2.5 mV. Hence, a threshold equal to 2.5 mV has been set in this case. Any pulse, which has a peak

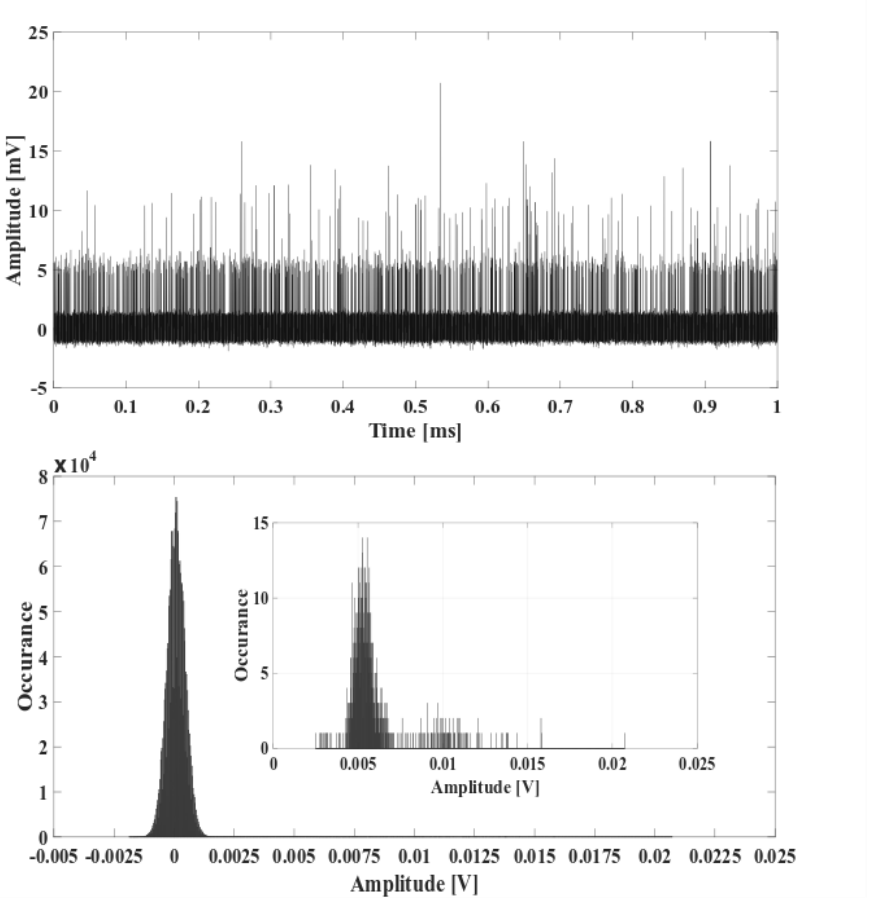


Figure 3.3 Signal captured in the total dark from the fast readout of the 30035 when biased at 28 V (Top) and histogram of the signal (Bottom). The inset shows the histogram of the pulses above the threshold value

amplitude greater than the threshold value will be counted as a number of counts. The number of counts depends upon the weight of the peak amplitude of that pulse and the definition of single pulse amplitude. The definition of single pulse amplitude is set equal to the mean value of the distribution of peak amplitude of pulses, which are greater than the threshold. The distribution of the peak amplitudes is shown in the inset of Figure 3.3. The mean value of the peak amplitudes in the distribution is approximately equal to 5.3 mV, which describe the maximum occurred peak amplitude.

A pulse, which has an peak amplitude greater than the threshold value and less than 1.5 times the single pulse amplitude (5.3 mV) would be counted as 1 [85]. Similarly, a pulse of peak amplitude greater than 1.5 times the single pulse amplitude would be counted equal to 2, which might be the case of two individual simultaneously avalanche breakdowns in two separate microcells. Likewise, a pulse greater than 2.5 times the single pulse amplitude would be counted equal to 3 and so forth. The total number of counts would be the sum of the number of counts per pulse. This method of counting the total number of counts over a length of time is known as peak counting method [46], [86]. In the same way, the total number of counts has been calculated at other bias voltages. Figure 3.4 shows the dark count rate as a function of the bias voltage applied at the SiPM. It is worth noting that the temperature also impact the dark count rate, however,

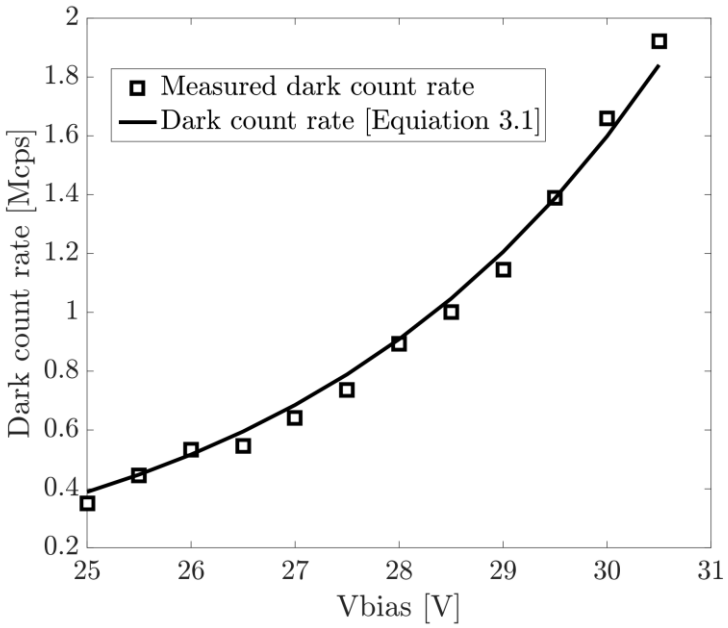


Figure 3.4 Dark count rate as a function of the bias applied at the 30035 at a surrounding temperature of 30 degree Celsius around the SiPM

during the measurement no temperature control unit is used to maintain the SiPM temperature. The solid line in Figure 3.4 is the model, which approximately describe the behavior of the dark count rate against a range of bias applied at the SiPM. The model can be expressed using the following relation [63]

$$DCR(V_{rel}) = e^{(a+b.V_{rel})} \quad (3.1)$$

V_{rel} is the relative overvoltage, which can be expressed as

$$V_{rel} = \frac{V_{BIAS}-V_{BR}}{V_{BR}} = \frac{V_{OV}}{V_{BR}} \quad (3.2)$$

where V_{BR} is the breakdown voltage of the SiPM, which is typically equal to 24.5 V, V_{BIAS} is the bias applied at the SiPM ranges from 25 V to 30.5 V, and V_{OV} is the overvoltage above breakdown voltage. a and b in Equation 3.1 are fitting parameters of the 30035, which may vary with the temperature and device and their best values are equal to 3.5 and 7.5 obtained from [63].

3.4.2 Bias dependent photon detection efficiency

The photon detection efficiency (PDE) of a SiPM is a measure of the sensitivity of a SiPM vs. the incident light. In practice, the PDE of a SiPM is the ratio of the number of detected photons to incident photons per unit of time over the area of a SiPM.

To measure the bias-dependent PDE, the experimental setup is shown in Figure 3.5. Due to the SiPM sensitivity at shorter wavelengths and negligible impact of WLED at around 400 nm (discussed in chapter 2), the wavelength chose is equal to 405 nm. The experiment consists of a L405P150 laser diode (LD) from THORLABS, wavelength centered at 405 nm, the dc power supply (GPS-3030D) supplies a 40 mA of current (marginally higher than the threshold current) to drive the LD. The beam of the bare laser diode was elliptical in shape and had an asymmetric distribution. Therefore, an aspheric condenser lens (ACL25416U-A) from THORLABS is used to collimate the light, which is then converged using a plano-convex lens (LA1805) and coupled to the fibre optic cable (M74L01) using the F240FC fiber collimator. An optical shutter is also used in the path of the light, where its gate mechanism is controlled by the interlocking system. A 25

mm wire-grid polariser (34-254) from Edmund Optics, which has been mounted in a manual

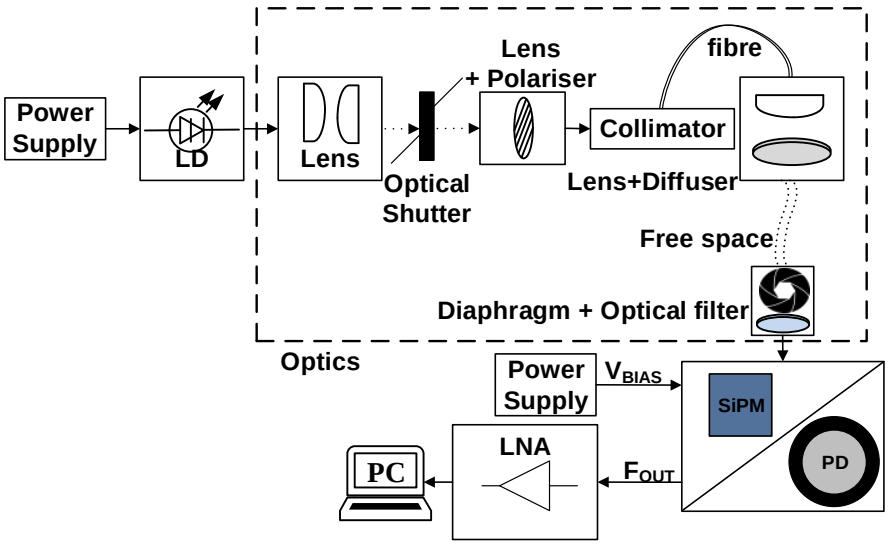


Figure 3.5 Block diagram of the experiment set-up to measure the measure bias-dependent PDE of the 30035 at 405 nm

rotation mount is also placed before the fiber collimator to vary the light coupled to the fiber optics. In order to accurately measure the PDE of the SiPM, the light coupled to the fiber optics has been lowered in the range of Pico Watt. The other end of the fibre optic cable is connected to a collimator following an optical diffuser (DG10-220-MD) so that the microcells of the SiPM can uniformly be illuminated. The resultant beam pattern is circular in pattern, symmetric around the center and larger than the SiPM area as shown in Figure 3.6. To filter out other wavelengths, a FB405-10 narrowband optical banpass filter is also used and placed above the detector as shown in the experiment.

Moreover, the experiment also include Newport's calibrated optical power detector (818-SL/DB), which has been used to measure the optical power arriving at the SiPM. The optical power detector is used with the Newport 1830-C picowatt digital optical power meter. To measure the optical power arriving the SiPM, the optical power detector is accurately placed at the position of the SiPM using X-Y translation stage, optical posts and other opto-mechanical components. To characterise the bias-dependent PDE of the selected SiPM, the optical power has been reduced

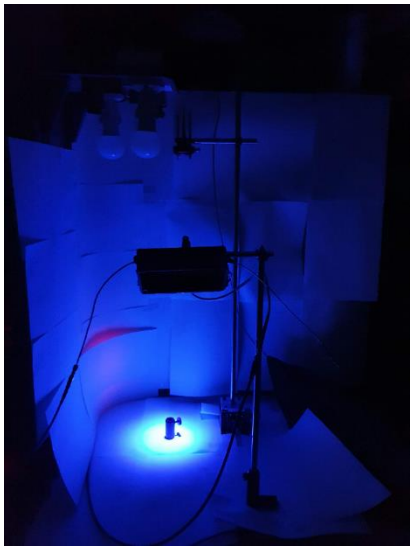


Figure 3.6 Resultant beam of the 405 nm transmitter

to 200 pW. The reason of using a low optical power is to increase the average time between incident photons so that individual photons can be counted accurately. In the case of high optical power, the count rate of the incident photons will be high and thus counting the individual pulses accurately may not be possible due to the significant pile-up of pulses. The count rate of the incident photon correspond to the 200 pW is equal to 38.37 Mcps. Alternatively, the average time between photons incident over the SiPM is approximately equal to 26 ns, which is significantly higher than the fast output pulse width. The count rate of the incident photons can be estimated using the following relation

$$r_{incdient} = \left(\frac{I_{rr} \times A_{SiPM}}{E_{ph}}\right) \tag{3.3}$$

where I_{rr} is the irradiance in W/m^2, and can be calculated as

$$I_{rr} = \frac{P_{opt}}{A_{PD}} \tag{3.4}$$

P_{opt} is the optical power measured at the position of the SiPM using calibrated optical power detector, A_{PD} is the area of the optical power detector, A_{SiPM} is the area of the SiPM, and E_{ph} is the energy of the photon at a wavelength and their values are listed in Table 3.2.

Parameter	Value
Area of SiPM (A_{SiPM})	9.425×10^{-6} m^2
Fill Factor (FF)	0.75
Area of optical power detector (A_{PD})	100.24×10^{-6} m^2
Energy of photon at 405 nm	4.9×10^{-19} joule

Table 3.2 SiPM and optical power detector parameters for Equation 2.2, 3.3 and 3.4

To measure the number of detected photons at an optical power of 200 pW, the optical power meter is replaced by the SiPM in the experiment. The bias voltage is applied at the SiPM from 25 V to 30 V with a step 0.5 V using variable dc power supply (GW Instek 3030D). The fast readout of the SiPM is used to measure the count rate of the detected photons at each bias. The fast readout is connected to the LNA (ZFL-1000LN+), which amplifies detected pulses. The LNA follows the scope (HDO6104-MS), which is used to capture the raw data over a period of 1 millisecond. The raw data is then used in MATLAB® to count the detected pulses using the peak counting method described in the previous section and converted to the count rate of the detected photons. For the true count rate of the detected photons, the DCR needs to be subtracted from

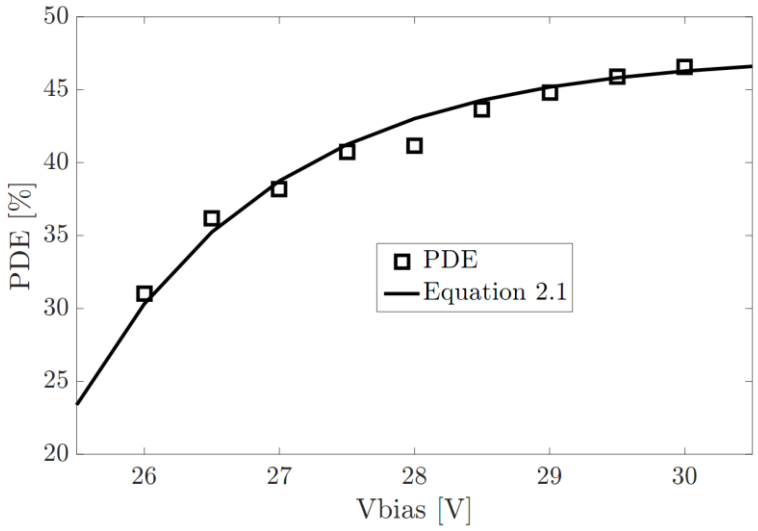


Fig. 3.7 Bias dependent PDE of the 30035 SiPM at 405 nm

the detected pulses. The PDE at each bias voltage has been obtained by dividing the true count

rate of the detected photons by the count rate of the incident photons. Figure 3.7 shows the measured PDE of the SiPM at 405 nm at a range of bias applied. The solid line fit in Figure 3.7 is the estimation, which is based on Equation 2.1, 2.2 and 2.3 and shows a good agreement to the measured PDE. The value of a_1 and absorption depth x for Equation 2.2 can be find in [87] and, a_2 in Equation 2.3 is approximately 0.06 at 400 nm for the 30035 [63]

3.4.3 The average standard output

The average output pulse of a SiPM can be used to determine various characteristics such as full width half maximum (FWHM) and effective recovery time of a SiPM. As discussed in section 3.3, onsemi$_{TM}$ SiPMs have dual output i.e. the fast output, which has a shorter output pulse width due its output being coupled to the low capacitance capacitors and a standard output. To evaluate the effective recovery time, the standard output is used, which does not comprise of any pulse-shaping or high-pass filtering effect. The datasheet of the J-Series SiPMs of onsemi$_{TM}$ shows the shape of both the fast and standard output pulse for their TSV package when a 10-ohm output resistance is used with the package and operated at a bias of 27 V. The recovery time has been calculated by calculating the time difference between the time at 90% and 10% of the maximum amplitude in the trailing edge. For instance, Figure 3.8 shows the pulse shape of the standard output of the 30035 and 60035. The time difference between the time at 90% and 10% of the maximum amplitude is approximately 115 ns and 180 ns for the 30035 and 60035 respectively [84]. However, the MicroFJ-SMA-30035 board has a series resistance of 50-ohm. Moreover, the optimum bias voltage investigated for this SiPM in [14] is equal to 28 V. Therefore, the same experiment, which is shown in Figure 3.2 has been setup and standard readout of the SiPM is used to measure the average output pulse of the SMA board and compared to the standard output pulse given in the datasheet.

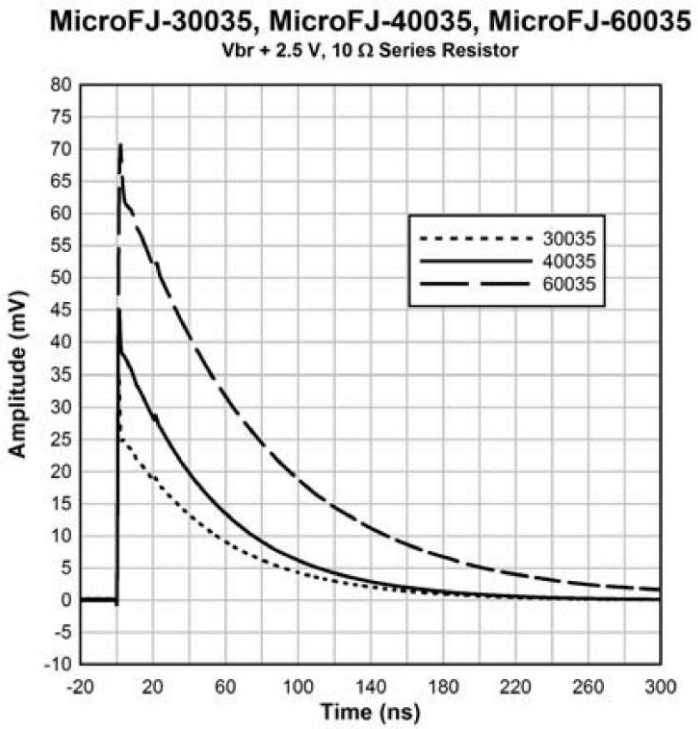


Figure. 3.8 Shape of the standard output pulse of J-Series SiPMs [76]

Figure 3.9 shows the measured averaged standard output pulse when the SMA board of the 30035 is biased at 28 V. The recovery time calculated is approximately 120 ns, which is quite close to the recovery time calculated from the standard output pulse shown in Figure 3.8, where they have used a 10-ohm series resistance. This means that an output resistance of 50-ohm on the SMA board does not significantly impact the recovery time of the SiPM. On the contrary, the MicroFJ-SMA-60035 board has the same series resistance as it has been mentioned for the output pulse provided in the datasheet. Hence, the recovery time calculated from Figure 3.8 has been considered credible.

The recovery time is a useful characteristic of a SiPM, which can be used to determine the dynamic range and maximum count rate of the detected photons of selected SiPMs. For SiPMs with non-paralysable response, the maximum count rate is the function of the total number

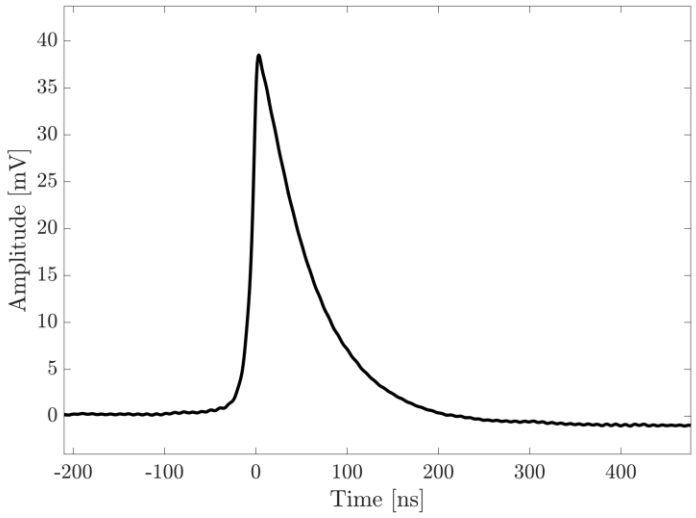


Figure. 3.9 The standard output pulse of the MicroFJ-SMA-30035 when biased at 28 V captured from Agilent's Infiniium DSO9254A 2.5 GHz, 20 Gsa/s scope. The pulse is averaged over 512 pulses triggered using the scope's built-in averaging function

of microcells and the effective recovery time. In this case, the maximum count rate can be described using the following expression [88], [89]

$$r_{np}^{max} = \frac{N_{\mu cell}}{T_r} \tag{3.5}$$

where T_r is the effective recovery time and $N_{\mu cell}$ is the total number of microcells in a SiPM. Based on recovery times (time difference between 90% and 10% of the maximum amplitude in the trailing edge) calculated from the standard output pulse, the non-paralysable maximum count rate (r_{np}^{max}) in this case would be around 48.5 Gcps for the 30035 and 124 Gcps for the 60035. Similarly, for SiPMs with paralysable response, the maximum count rate can be defined as [90]

$$r_{p}^{max} = \frac{N_{\mu cell}}{\exp(1) \times T_r} \tag{3.6}$$

Hence, the paralysable maximum count rate (r_{p}^{max}) in this case would be around 18 Gcps for the 30035 and 45.5 Gcps for the 60035.

3.4.4 Dynamic range

The dynamic range describe the response of a SiPM against the light incident on the SiPM. The response can be measured as the detected photons and/or current drawn by the SiPM. The dynamic range of a SiPM depends upon various parameters such as the recovery time, number of microcells and PDE. To measure and compare the dynamic range of selected SiPMs, an experiment similar to the experiment shown in Figure 3.5 has been used. The experiment setup is shown in Figure 3.10, and is used measure the current drawn by the SiPM at a range of irradiance. The experiment include the same optics used in the measurement of bias-dependent PDE except a slight change in the bias connection to the SiPM. In the bias connection a digital

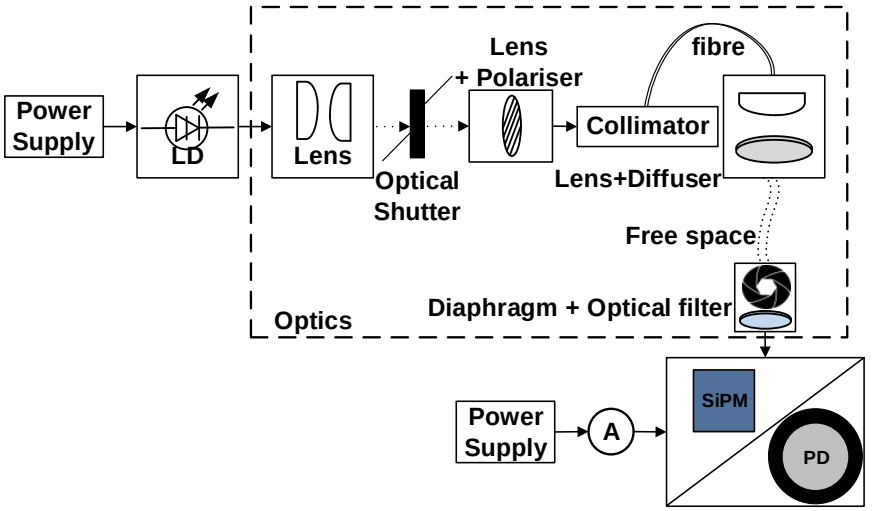


Figure 3.10 Block diagram of the experiment set-up to measure the response of the 30035 and the 60035 SiPM

ammeter has been introduced between the bias terminal of the SMA board and the dc power supply as shown in Figure 3.10 so that the current drawn by SiPMs can be measured. However, prior to measure the current drawn by the SiPM, the optical power detector is used to measure the optical power arriving at the position where the SiPM was placed. A range of optical power has been measured. To vary the irradiance, the polarisation of the wire-grid polariser has been changed using the rotational dial face (engraved scale marked) of the rotation mount and the optical power is recorded at each 4 degree of increment. Once a range of optical power has been

measured, the optical power detector is then replaced with the SiPM to measure the photocurrent at the same range of irradiance.

Keithley's 195A digital ammeter is used to measure the current drawn by the SiPM when biased at 28 V. Figure 3.11 shows the measured response of both the 30035 and the 60035 SiPM against a range of irradiance falling on the SiPM. From the measured response it can be seen that both SiPMs are linear up to approximately 1 mWm^{-2}. However, the response of the 60035 reaching saturation gradually compared to the 30035. Figure 3.12 shows the insight of saturation

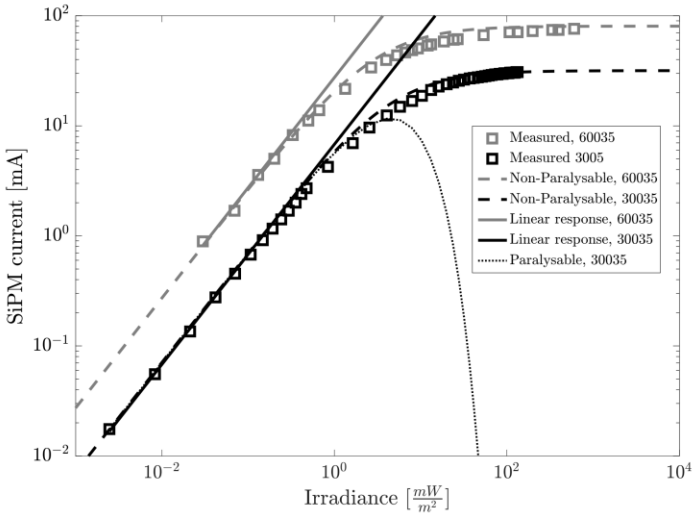


Figure 3.12 Measured photocurrent as a function of irradiance at 405 nm reaching the 30035 and the 60035 SiPM when both biased at 28 V

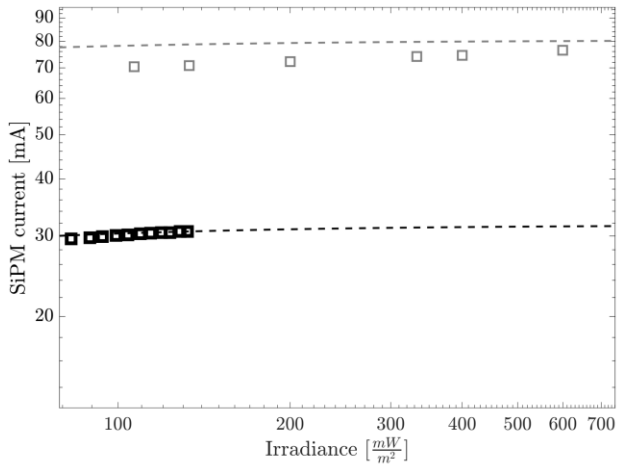


Figure 3.11 The insight of saturation response of the 30035 and the 60035

response of both SiPMs. For the 30035, it can be seen that from 80 mWm^{-2} to 130 mWm^{-2}, there is only a 3% increase in the current, which suggest that the 30035 is almost saturated at around 31 mA. Whereas, the 60035 approaching saturation between 300 mWm^{-2} to 600 mWm^{-2}, where its response within this range of irradiance shows a 3% increase in the current and saturating at around 75 mA. The dotted and dashed lines in Figure 3.11 is the estimation of the SiPM current, which depend upon the single microcell charge and the count rate of the detected photons and can be estimated as

$$I_{SiPM} = q_{\mu cell} \times r_{detected} \tag{3.7}$$

where $r_{detected}$ depend upon the type of detector. For a paralysable type detector, the count rate of the detected photons can be estimated as [88], [89]

$$r_p = r_{incident} \times PDE \times \exp\left(-\frac{r_{incident} \times PDE \times T_r}{N_{\mu cell}}\right) \tag{3.8}$$

$r_{incident}$ is the count rate of the incident photons (Equation 3.3), PDE is the photon detection efficiency, T_r is the effective recovery time, and the $N_{\mu cell}$ is the total number of microcells in a SiPM. $q_{\mu cell}$ in Equation 3.7 is the charge on the single microcell, which depend upon the effective microcell capacitance ($C_{\mu cell}$) and the overvoltage (V_{ov}) applied at the SiPM. The relation for the charge at single microcell can be expressed as

$$q_{\mu cell} = C_{\mu cell} \times V_{ov} \tag{3.9}$$

A generic way of estimating the microcell capacitance is given as [91]

$$C_{\mu cell} = \frac{C_t}{N_{\mu cell}} \tag{3.10}$$

Where C_t is the terminal capacitance of the SiPM output. The onsemi$_{TM}$ J-Series datasheet provides terminal capacitance for both the fast and standard output of their SiPMs. The terminal capacitance may affected by the parasitic capacitances of the quenching resistor and traces on the board. Hence, the method may overestimates the microcell junction capacitance. However,

the overestimation may not be significant, particular for SiPMs having large microcell sizes such as 35 microns [91]. This has been checked by comparing the microcell capacitance (187 fF) and charge (0.65 pC) at microcell estimated using Equation 3.9 and 3.10 to the microcell capacitance in [63] and microcell charge in [92], which show no significant difference.

For a non-paralysable, the count rate can be estimated as follows [88]–[90]

$$r_{np} = \frac{r_{incident} \times PDE}{(1+\frac{r_{incident} \times PDE \times T_r}{N_{\mu cell}})} \tag{3.11}$$

Table 3.3, summarises the value of the parameters used to estimate the SiPM current. The estimated current (dotted line) in Figure 3.11 is based on the paralysable count rate, results suggest that the SiPM is of non-paralysable type. However, when estimated the current (dashed line) based on the non-paralysable count rate, the estimation almost describe the measured response the SiPM, which clearly shows that the SiPM is of non-paralysable type.

Parameter	**Value**	
Microcell capacitance ($C_{\mu cell}$)	**60035**	**30035**
	~187F	
Overvoltage (V_{oV})	3.5 V	
Photon detection efficiency (PDE) at 405 nm when biased at 28 V	~40 %	
Active area of SiPM (A_{SiPM})	36.8e-6 m^2	9.4e-6 m^2
Recovery time (T_r) [onsemi$_{TM}$ averaged Sout pulse]	~180 ns (90%-10% of V_{max}) with 10 ohm load	~115 ns (90-10% of V_{max}) with 10/50 ohm load

Table 3.3 Parameter values used in equation (3.8), (3.9), and (3.11) to estimate the photocurrent generated by SiPMs

To make sure that the saturation has been by SiPMs, the estimated current based on the non-paralysable model has been extended to an irradiance of 10 Wm^{-2}. The saturation has been checked between the third last measured data point of both the 30035 and 60035 and 10 Wm^{-2}. For both SiPMs, it has been noticed that there is a less than 1% increase in the current within the range mentioned above. This suggest that both SiMPs are saturated within their respective range of irradiance, which are discussed earlier.

Moreover, the ratio of the estimated current of the 60035 to 30035 and the ratio of the

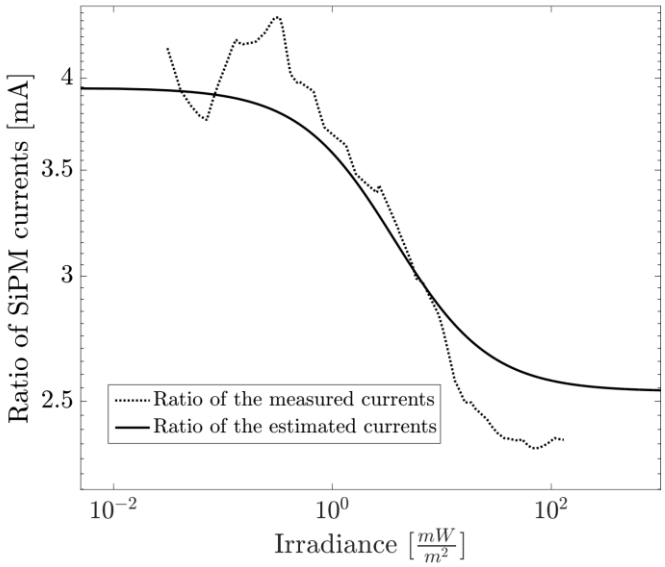


Figure 3.13 Ratio of the estimated currents and measured currents between the 60035 and 30035 at a range of irradiance

measured current of the 60035 to 30035 are also compared. From Figure 3.13, it can be seen that at lower irradiances, the ratio estimated currents is around 4. Ideally, the ratio between the current of the 60035 and 30035 can also be estimated by comparing their size. However, the ratio of the estimated currents starts to fall significantly when the irradiance is around 1 mWm^{-2} and saturate at around 2.5 when the irradiance is over 100 mWm^{-2}. Factors that cause the ratio of estimated currents to decline as the irradiance increases include the finite number of microcells, and linearity of the SiPMs, which is related to the relationship between the inter-photon time and effective recovery time, which has been discussed later in this chapter. While comparing the ratio of measured currents (dotted line) to the ratio of estimated currents (solid line), it can be seen that the ratio of measured currents follows almost the same trend as the ratio of estimated currents and saturates at around slightly below 2.4 at which the ratio of estimated currents is saturated. However, the variations in the ratio of measured currents may have been caused by factors such as variations in the temperature, measurement and the microcell charge.

3.5 Effective PDE vs. the Irradiance

The PDE is an important characteristic, which determines how sensitive a detector is against an incident light. In other words, the PDE describe the capability of a SiPM for detecting photons against the incident photons per unit of time. In addition to physical properties of a SiPM such as the microcell structure, fill factor and total number of microcell, which influence the PDE. The amount of incident light also important, which impact the PDE. For this reason, results from the previous section have been used to analyse the effective PDE of selected SiPMs. For instance, as both the 30035 and the 60035 exhibit non-paralysable behaviour. Therefore, dividing the count rate of the detected photons based on the non-paralysable (Equation 3.11) by the count rate of the incident photons (Equation 3.3) can be used to estimate the effective PDE as

$$PDE_{est} = \frac{r_{np}}{r_{incident}} \tag{3.12}$$

Figure 3.14 shows the PDE estimated for the 30035 and the 60035 SiPM at a range of irradiance. From figure, it can be seen that despite the recovery time is 1.5 times the recovery

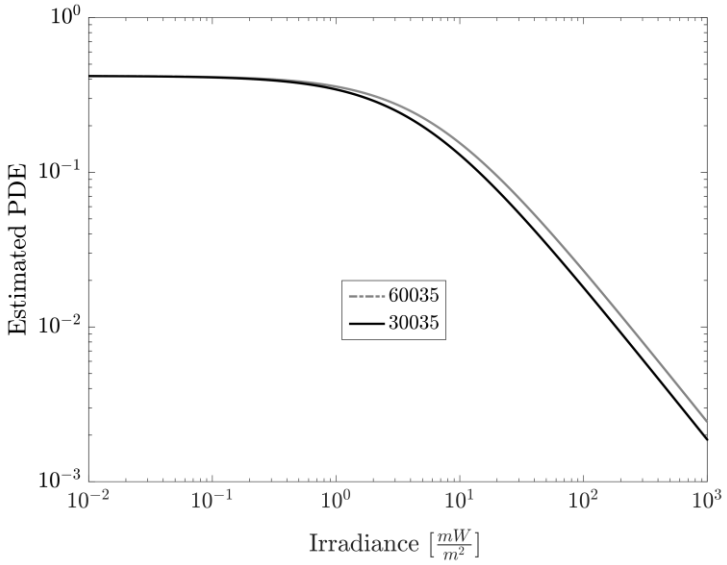


Fig. 3.14 Estimated PDE vs. the average irradiance reaching the 30035 and the 60035 SiPM

time of the 30035, the PDE (black dashed-dotted line) of the 60035 is almost the same as the 30035 (black solid line) up to approximately 1 mWm^{-2}. However, the PDE start to reduce as the

irradiance goes higher than 1 mWm$^{-2.}$ Therefore, the average time between the incident photons over the microcell active area has been compared to the recovery times, which have been used to estimate the current of 30035 and the 60035 SiPM. Re-arranging Equation 3.3 to estimate the average time between the incident photons as

$$T_{inter-\mu cell} = \frac{E_{ph}}{A_{\mu cell} \times I_{rr}} \tag{3.13}$$

where $A_{\mu cell}$ is the active area of the microcell, E_{ph} is the energy of photon at 405 nm, and I_{rr} represent the average irradiance in Wm^{-2}. A convenient way to calculate the microcell area is to divide the active area of the SiPM by the total number of microcells as

$$A_{\mu cell} = \frac{A_{SiPM}}{N_{\mu cell}} \tag{3.14}$$

The grey dotted and dashed lines in Figure 3.15 represents the PDE of the 30035 and the 60035 with respect to their ratio of the recovery time to the average inter-photon time of the

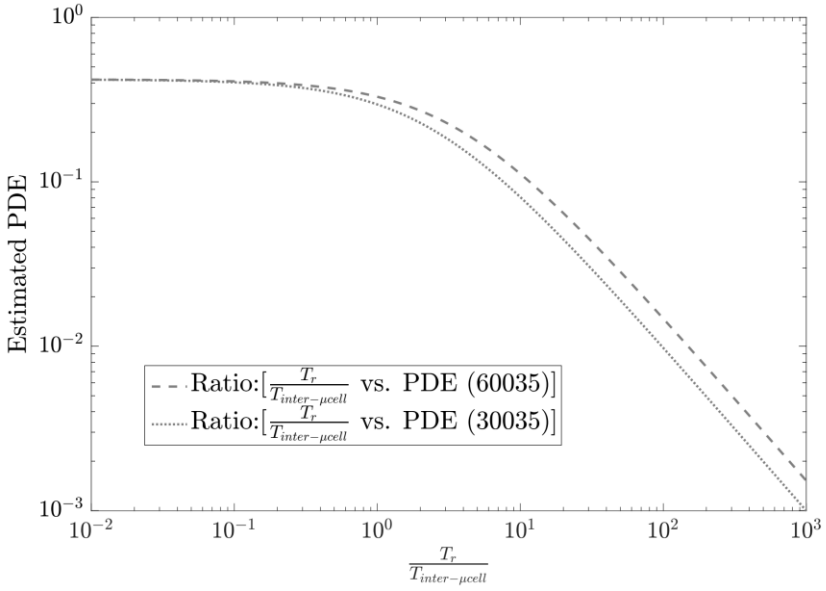


Fig. 3.15 Estimated PDE vs. the ratio of the recovery time to the average time between the photon hitting the microcell>

microcell. Results show that at lower irradiances, when the average inter-photon time is significantly higher than the recovery time, the PDE remains constant. However, when the

irradiance is over 1 mWm^{-2}, the average inter-photon time is comparable to the microcell recovery time. For instance, at 1 mWm^{-2}, the ratio of the recovery time of the 30035 to the average inter-photon time is equal to 0.4, whereas, the ratio is equal to 0.6 in the case of the 60035. However, above 1 mWm^{-2}, both of the ratios approach to 1 and as a result, the PDE starts to decline significantly as shown in Figure 3.15. Furthermore, it can also be noticed that despite the larger recovery time of the 60035, it shows the same PDE as the 30035 at irradiances 30% higher than irradiances at the 30035 as shown in Figure 3.15. The primary reason that the 60035 is a bit better than the 30035 is because of its large number of microcells compared to the 30035.

3.6 Summary

In this chapter, key parameters, which are important to select a SiPM, a brief surrey of off-the-shelf SiPMs, experimental methods to characterise and analytical models to predict various performance parameters of a SiPM, and a comparison between two different SiPMs are presented. To select a SiPM, typically, its sensor size, microcell fill factor, PDE, output pulse width and recovery time, and non-ideal effects such as dark count rate are important. Onsemi$_{TM}$ J-series SiPMs are selected due to their fast output pulse width, which is equal to 1.5 *ns* for the 30035 and 3 *ns* for the 60035 respectively. As the bias voltage applied to a SiPM determines various important characteristics such as dark count rate and PDE at a wavelength. Therefore, initially, the dark count rate and PDE at 405 nm have been measured at a range of bias voltages applied at the SiPM. As both SiPMs have the same DCR per square millimetre and PDE as described in the datasheet [84]. Therefore, the characterisation of bias-dependent DCR and PDE has been performed only at the 30035. Results show that the dark count rate and PDE strongly depend upon the value of bias applied at the SiPM. Although, the PDE increases with the bias voltage, however, it should be noted that the non-ideal effects such as dark count rate and the probability of after-pulsing and cross-talk also increase. Therefore, these non-ideal effects should be limited

and the SiPM should be operated at an optimum bias voltage. This optimum bias voltage is equal to 28 V for the 30035, which has been discussed in section 3.4.3.

Similarly, the recovery time of a SiPM is also an important parameter, which determines factors such as the maximum count rate and dynamic range of a SiPM. To calculate the effective recovery, average standard output of the 60035 and the 30035 were analysed, where the effective recovery has been calculated by measuring the time difference between 90% and 10% of the maximum amplitude of the trailing edge. The recovery times calculated are equal to approximately 118 ns and 180 ns for the 30035 and 60035 respectively and their maximum count rate based on the non-paralysable count rate (Equation 3.5) are approximately 48 Gcps and 124 Gcps respectively. These count rate suggests that for a BER of 1×10^{-3}, where 6.2 photons are required per bit by an ideal receiver, a data rate of 7.7 Gbps, and 20 Gbps can be achieved by the 30035 and 60035 respectively. However, in practice, the achievable data rate is limited by factors such as finite bandwidth, non-ideal effects, non-linearity, and effective PDE of the SiPM.

The dynamic range of a SiPM determines its linearity in terms of the detected photon rate against the incident photon rate. The dynamic range of a SiPM can be used to predict its performance as a VLC receiver in terms of the average irradiance required to achieve a particular BER at a given data rate. Typically, the dynamic range depends upon factors such as the total number of microcells, effective recovery time, applied bias and PDE of the SiPM. The dynamic range has been measured separately for the 30035 and 60035 in terms of their measured SiPM current at a range of irradiance incident on their active areas. Two models are presented, which estimate the SiPM current (Equation 3.7) and have been compared to the measured SiPM current. The first model is based on the paralaysable count rate (Equation 3.8), and the second is based on non-paralysable count rate (Equation 3.11). The measured SiPM current has been well described by the second model and suggests that SiPMs are of non-paralysable type. Moreover, it has been observed that the measured SiPM current of both SiPMs increases linearly

up to an irradiance slightly less than 1 mWm^{-2}, which means that as long as their responses are linear, the ratio of sensitivity between the 60035 and 30035 SiPM will approximately be equal to 4 as expected from their difference in size. However, the ratio of sensitivity falls to approximately 2.5 when their response approach saturation at irradiances over 100 mWm^{-2}, which has been discussed in section 3.4.4. This suggest that a maximum sensitivity can be obtained when SiPMs are operating in the linear region.

Chapter 4

Performance Evaluation

4.1 Introduction

The potential of a SiPM as a sensitive VLC receiver depends upon various factors such as its pulse width, photon detection efficiency, dynamic range and active area. Typically, the performance of a SiPM-based VLC receiver can be evaluated on the basis of its irradiance required to achieve a target BER at a given data rate, which strongly depends upon these factors. The performance of the 30035 SiPM as a VLC receiver has already been evaluated through experiments and results are published in [37], [93]. In [37], [93], the dc bias optimisation of the SiPM and the laser diode, selection of the voltage swing, baseline problem of the amplifier, and impact of the non-linear effect of the SiPM and inter-symbol-symbol are studied.

The aim of this chapter is to study and compare various aspects such as sensor size, pulse width and dynamic range, and to present methods of predicting the performance of a SiPM. For this reason, experiments have been performed using the 60035 and the 30035 and their results are compared. As discussed in chapter 2, the 30035 and the 60035 have the same PDE and the microcell size except, the 60035 occupies a size approximately 4 times the size of the 30035. This means that the 60035 would be able to cover an irradiance 4 times the irradiance, which can be covered by the 30035. Hence, it can be anticipated that the 60035 would require an irradiance 4 times less than the irradiance required by the 30035 to achieve a target BER at a given data rate. However, when operating in the ambient light, the large size of the 60035 means, the impact of background light will be 4 times worse than the impact on the 30035. Therefore, the performance of these SiPMs will also be compared in the presence of ambient light. Moreover,

optical filtering to mitigate the impact of ambient light, and the impact of output pulse and dynamic range on the performance will also be investigated in this chapter.

4.2 Experimental setup

To measure the impact of various factors on the performance of SiPM, the experiment has been set up in a way that the transmitter is set up in conjunction with a warm white LED lamp, which act as an ambient source. The spectrum of the warm white LED is shown in chapter 2. The reason for choosing the warm white over the cool white LED is that the blue part of its spectrum is suppressed, which may raise concern for the eye-safety [94]. The illuminance set from the LED lamp at the position of the SiPM is equal to the standard lighting levels in the workplace defined under the Health & Safety at Work Act of 1974, which is equal to 500 lux [20]. Figure 4.1 shows

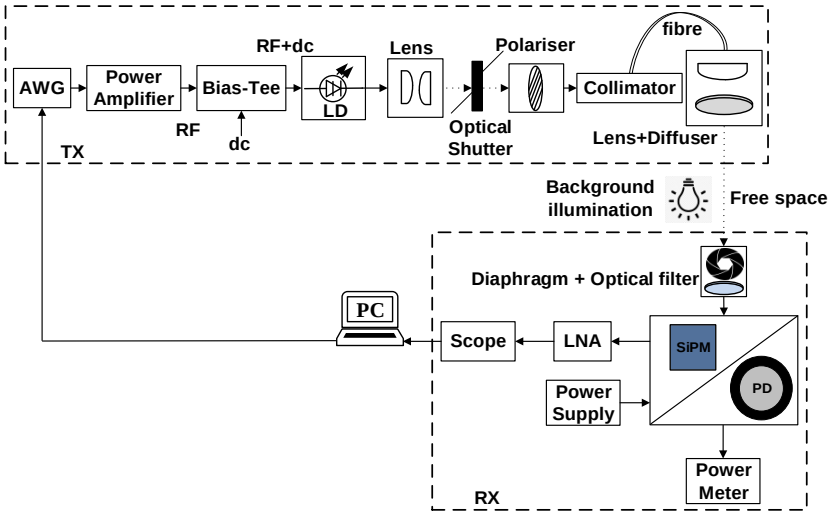


Figure 4.1 System block diagram describes the experimental setup used to evaluate the performance of selected J-Series SiPMs

the block diagram of the experimental setup, where the transmitter and receiver are approximately 1 m apart from. The transmitter chain consists of Tektronix 7000A series arbitrary waveform generator (AWG), follows Fairview Microwave FMAM3269 6 GHz amplifier, which amplifies the AWG output. The amplifier has been used because the maximum peak-to-peak voltage, which can be generated by the AWG is limited to 500 mV. Following the amplifier, Mini-circuits® ZFBT-

4R2GW+ bias-Tee is used, which adds dc to the RF signal so that the laser diode (THORLABS L405P20) can be prevented from the reverse bias. The optics in the transmitter chain and their arrangement are the same as used for the measurement of dynamic range of SiPMs. Similarly, the receiver chain consist of Thorlab FB405-10, narrow bandpass optical filter to reject the ambient light reaching the SiPM. To amplify the signal from the fast readout of the SiPM, Mini-circuits® ZFL-1000LN+ low noise amplifier is used. The signal from the output of the amplifier is then recorded using Infiniium V-Series MSOV334A, 33 GHz scope and processed offline using MathWorks® MATLAB.

4.3 Channel response

Prior to transmitting any data to the SiPM, the frequency response of the channel has been measured. The same experimental setup has been used as shown in Figure 4.1. However, except

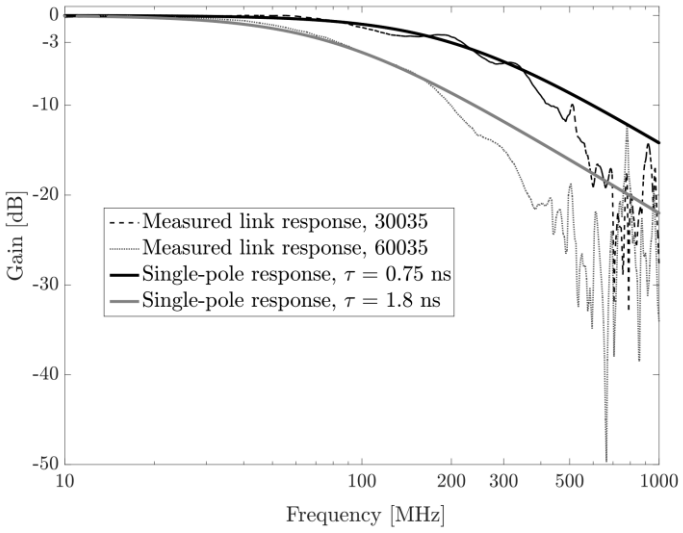


Figure 4.2 Frequency response of the link when the 30035 (black dashed) and 60035 (grey dotted) are used. The solid line is the first-order low-pass filter responses with τ = 0.75 ns (black solid) and τ = 1.8 ns (grey solid)

the AWG and PC, the HP 8753 series vector network analyser (VNA) is used. Port 1 of the VNA is connected to the power amplifier at the transmitter side and port 2 is connected to LNA's output.

The input of the LNA is connected to the fast output of the SiPM. To measure the frequency response, a sine-wave ranging from 300 kHz to 1.3 GHz is generated using the VNA. The signal is then amplified to approximately 1.6 V peak-to-peak to avoid any non-linearity, which may occur from the amplifier when a large voltage is used, and a dc bias of approximately 35 mA (equivalent to 3.3 V) is added to the signal using Bias-Tee. The resulting signal is then applied to the laser diode, which generates an optical signal transmitted to the SiPM. Subsequently, the frequency response has been measured using the VNA. The SiPM is biased at 28 V and no background illumination is used. Figure 4.2 shows the measured frequency response of the system for both when the 30035 and the 60035 is used. The maximum gain of the system is normalised to 0 dB, and it can be seen the gain of the system drops by 3dB at a frequency of 215 MHz (black dashed line) when the 30035 is used and 80 MHz (grey dotted line) when the 60035 is used. Solid lines in Figure 4.2 are first-order low-pass filter response. The first-order low-pass filter response is expressed as

$$G\ (dB) = 20 \times \log_{10}(\frac{1}{1+j\omega\tau}) \tag{4.1}$$

where ω is the angular frequency in rad/sec and τ is the RC time constant. The black and grey solid line responses are obtained using Equation 4.1 with RC time constants equal to 0.75 ns and 1.8 ns respectively. From Figure 4.2, it can be seen that the first-order low-pass responses approximately define the measured link response up to 350 MHz and 170 MHz for the 30035 and 60035 respectively. However, as the frequency increase, the measured link response deviate from the first-order low-pass response.

4.4 Link results in the dark

In practice, the maximum achievable data rate of an optical communications system depends upon factors such as bandwidth, background noise, and the modulation scheme. The performance of selected SiPMs has been evaluated using non-return-to-zero (NRZ) modulation

scheme. In chapter 2, a relationship between the 3dB bandwidth (BW_{3dB}) and the data rate (R_b) for a NRZ receiver is discussed. The relationship states that when a NRZ data of a rate twice the 3dB bandwidth is transmitted at the receiver or when the ratio between BW_{3dB} and R_b is less 0.5, a significant rise in the power penalty was been observed [77]. In the later sections, the trend of this power penalty will be investigated based on the 3dB bandwidth of the measured frequency response of the system when the 30035 and the 60035 are used.

From Figure 4.2, it can be seen that the 3dB bandwidth of the system is approximately 215 MHz when the 30035 is used. Whereas, in the case when the 60035 is used, the 3dB bandwidth is equal to approximately 80 MHz. Based on these 3dB bandwidths, it can be anticipated that a data rate of 430 Mbps can be achieved using the 30035 and 160 Mbps approximately using the 60035 without encountering the ISI power penalty.

4.4.1 Results without equalisation

Initially, the performance of SiPMs is evaluated in the dark. The transmitter configuration is has been set in a way that it generates an 8b10b encoded data or a frame of length equal to 40960 bits ($2^{15}+2^{13}$), which has been transmitted to the SiPM using the same dc bias and voltage swing used in the measurement of the frequency response of the system. However, the voltage swing does not ensure that the transmitter will be completely OFF i.e. transmit no light when transmitting 0s. This means that the transmitter may contribute to the background noise when transmitting 0s. The 8b10b encoding is used to overcome the base-line problem of the amplifier as the amplifier used in the transmitter has a lower cut-off of 10 MHz, which may introduce a droop in the signal when a long sequence of 1s occurs [95]. Hence, 8b10b encoded data avoid a long sequence of 1s and 0s, provide a DC-balanced serial data sequence, and maintain a maximum run-length of 5 [95]. On the receiver side, a dc bias of 28 V is applied at both of the SiPMs, which is the optimum bias voltage investigated in [14].

Since the target BER is 1×10^{-3} and to ensure this BER, multiple frames are transmitted to the SiPM and an average BER is calculated. The BER of single frame is calculated in a way that the received raw signal is first is low-pass filtered using a first-order Butterworth filter in MATLAB, whose cut-off frequency is adjusted according to the ratio of the data rate and sampling of the scope. The filtered signal is then correlated to the transmitted signal so that the first and last bit of the frame can be synchronised to the transmitted signal. Subsequently, the signal has been down-sampled by picking a sample from the mid each bit. Each sample is then separated according to the corresponding transmitted bit. If the sample of the received bit corresponds to the bit '1' transmitted it will be sorted in the distribution of 1s. Similarly, if the sample of the received bit corresponds to bit '0' then it will be sorted in the distribution of 0s. Once, distribution of received samples correspond to 1s and 0s have been extracted, then a range of threshold starting from the mean of the distribution of 0s to the mean of the distribution of 1s is selected. At each value of threshold, the number of received 1s and 0s are separated to measure the BER. A threshold is considered to be the optimum at which the BER is minimum. If the minimum BER is not close the target the BER, the above process is then repeated by varying the irradiance reaching the SiPM using polariser.

The data is transmitted using a voltage swing of 1.6 V peak-to-peak and a dc bias 3.3 V is applied at the laser diode. However, a low voltage swing means that the transmitter is not fully turned-off when transmitting 0s. In the case of 1.6 V peak-to-peak means that the logic level '0' corresponds to 2.5 V when a dc bias of 3.3 V is added to the signal. Therefore, the transmitter will contribution to the number of background counts per bit when transmitting 0s. Apart from this, the SiPM has its dark count rate, which also contribute the background counts per bit to both of the levels i.e., logic level '0' and logic level '1'. For this reason, an average irradiance required by the SiPM has been estimated at a range of data rates, so that it can be compared to the measured average irradiance. The solid line in Figure 4.3 is the estimation of the average irradiance, which

is based on the PDE of the SiPM at 405 nm, area of the SiPM (A_{SiPM}), and the average number required photons (n_s) from the transmitter in a bit duration, which depends upon the target BER and the number of background counts (n_b) per bit. The average number of photons per bit can be estimated using Equation 2.8 expressed in section 2.4.2. The equation for estimating the average irradiance required from the transmitter at a given data rate can be expressed as [40]

$$I_{avg} = \frac{n_s \times E_{ph}}{T_b \times PDE \times A_{SiPM}} \tag{4.3}$$

where E_{ph} is the energy of photons at wavelength equal to 405 nm. As discussed earlier, the number background counts per bit involves the dark counts of the SiPM and the background counts from the transmitter when it transmit 0s. The dark count rate of the 30035 is approximately equal to 1 Mcps at a bias voltage 28 V as shown in Figure 3.4. Similarly, the background count rate from the transmitter can be estimated by transmitting a light on the SiPM corresponds to the dc level of bit '0' (2.5 V) at a given data rate. Since, the dc level of bit '0' was not been measured at any data rate during the experiment, therefore, initially, a range of the number of background counts per bit is chosen at a single data rate i.e. at 200 Mbps. For each number of background counts per bit, the average number of required photons per bit is estimated using Poisson statistics and then the average irradiance using Equation 4.3. The average irradiance estimated satisfies the measured average irradiance, when the total number of background counts (including dark counts) is approximately equal to 0.95 per bit and an average number of photons of 7.4 per bit is required. This number of background counts corresponds to an irradiance of 24.7 μWm^{-2} when the transmitter transmits 0s, which can be calculated by substituting n_s with n_b in Equation 4.3. However, to calculate the background counts per bit at other data rates, the extinction ratio (R_e) is a useful term, which can be expressed as

$$R_e = \frac{I_1}{I_0} \tag{4.4}$$

The irradiance, which corresponds to the logic level '1' can be estimated as

$$I_1 = 2I_{avg_m} - I_0 \tag{4.5}$$

where I_{avg_m} is equals to 0.2 mWm^{-2} at 200 Mbps and I_0 equals to 24.7 μWm^{-2} and the resulting I_1 is equals to 375 μWm^{-2}. Substituting the value of I_0 and I_1 in Equation 4.4 gives an extinction ratio approximately equal to 15. The extinction ratio is then can be used in Equation 4.6 to estimate the irradiance corresponds to logic level '0' at other data rates as

$$I_0 = 2I_{avg_m}(\frac{1}{R_e+1}) \tag{4.6}$$

where I_{avg_m} is the measured average irradiance at a given data rate. To translate the estimated irradiance I_0 to the number of background counts per bit the following expression can be used

$$n_b = \frac{I_0 \times PDE \times A_{SiPM} \times T_b}{E_{ph}} \tag{4.7}$$

Once the number of background counts per bit (n_b) has been calculated, the process of estimating the average number of photons per bit required and average irradiance is then repeated at other data rates. Figure 4.3 shows the average irradiance required from the transmitter in the dark by the 30035 and the 60035 SiPM at a range of data rates. From Figure 4.3, it can be seen that in the case of the 30035, the estimated average irradiance (solid black line) approximately describe the behavior of the measured average irradiance (black diamond) up 500 Mbps (2.7 on the log scale). However, above 500 Mbps, a power penalty has been observed. The power penalty at data rates higher than 500 Mbps is related to the ISI present in the system. The ISI power penalty has been discussed in section 2.5, which describe that when the ratio between the 3dB bandwidth and the data rate falls below 0.5, the power penalty starts to rise significantly.

Figure 4.4 compares the power penalty (black circles) of the 30035 to the power penalty (solid line) of the first-order low-pass filter against the ratio of the 3dB bandwidth (215 MHz when

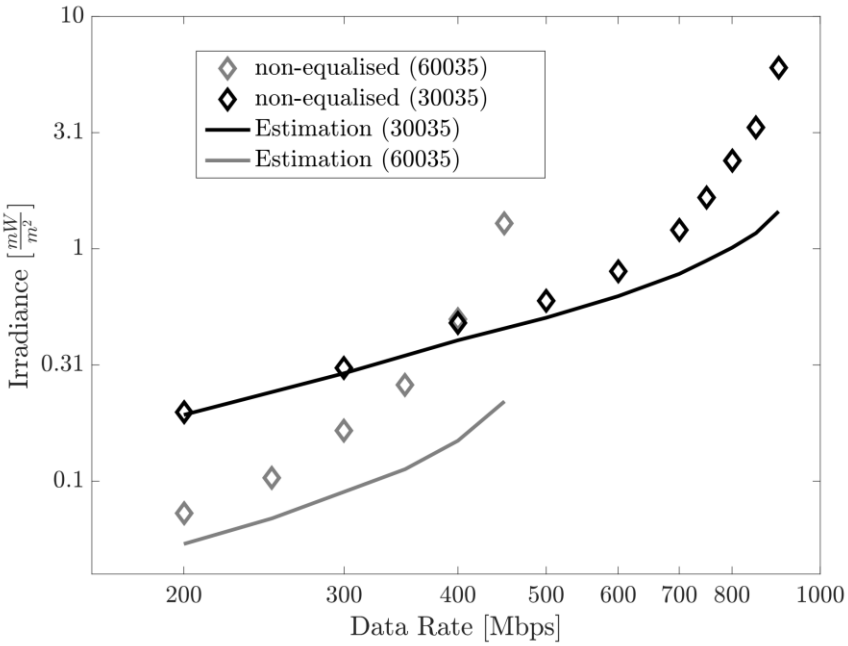


Figure 4.3 Data rate vs. average irradiance required by the 30035 and the 60035 to achieve a target BER of 1×10^{-3}. The performance is evaluated in the dark without equalisation applied at the received signal

the 30035 is used) to the data rate. From Figure 4.4, it can be seen that as expected the power penalty of the 30035 lies between 0 dB and 0.5 dB as far as the ratio of the 3dB bandwidth and the data rate is below 0.5. However, it is worth noting that the measured frequency response (dashed line in Figure 4.2) of the system deviates from the fist-order low-pass response (black solid line in Figure 4.2) at frequencies higher than the 3dB frequency. Moreover, the average irradiance required by the SiPM at data rates higher than 500 Mbps is around 1 mWm^{-2}. At this irradiance, the non-linearity of the SiPM, which has been discussed in section 3.4.4 starts to impact on the average required irradiance. Hence, as a result of ISI and non-linearity, the power penalty of the 30035 is steeper as compared to observed in the case of the first-order low-pass response.

On the contrary, when the 60035 is used, Figure 4.3 shows that the average required irradiance (grey diamond) has a similar behavior as when the 30035 is used. From Figure 4.3, it can be seen that the 60035 is better at lower data rates i.e. it require less irradiance than the

30035 until the data rate is reached to 400 Mbps (2.602 on the log scale). However, as the data rate is higher than 400 Mbps, the 60035 requires more irradiance than the 30035, which is mainly related to the limited bandwidth of the system when the 60035 is used and the ISI power penalty, which have been discussed later in this section.

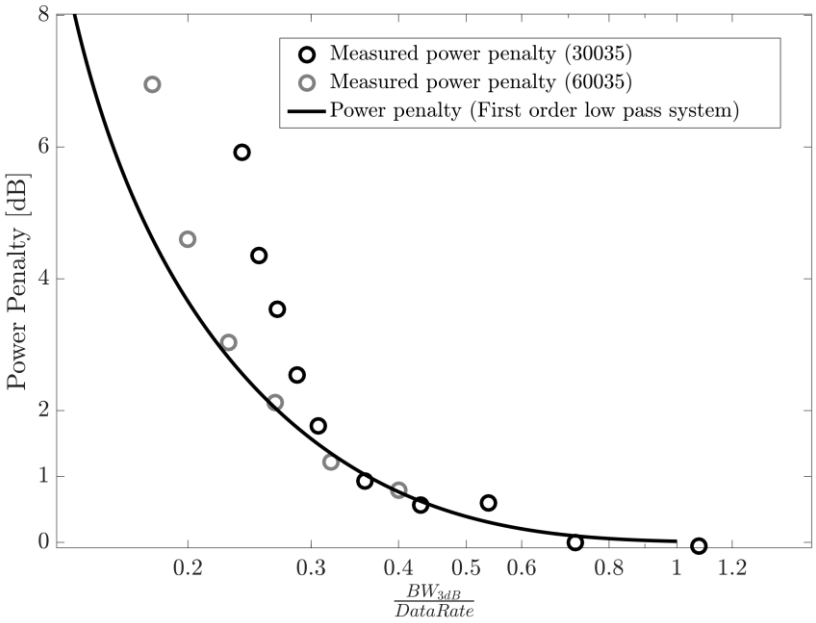


Figure. 4.4 Power penalty vs. the ratio of the 3dB bandwidth to the data rate. Black and grey circles show the measured power penalty for the 30035 and 60035, respectively, and when no equalisation is applied to the received signal

Figure 4.4 also compares the power penalty (grey circle) of the 60035 to the power penalty (solid line) of the first-order low-pass filter. From Figure 4.4, it can be seen that as expected when the ratio between the 3dB bandwidth (85 MHz when the 60035 is used) to the data rate is below 0.5, the power penalty of the 60035 is slightly steeper as compared to the power penalty of the first-order low-pass system. The deviation of power penalty of the 60035 from the power penalty first-order low-pass system is because of the deviation of the measured frequency response (dotted line in Figure 4.2) from the fist-order low-pass response (red solid line) at frequencies higher than the 3dB frequency. However, from Figure 4.3, it can be seen that the average irradiance required by the 60035 from 200 Mbps (2.3 on log scale) to 450 Mbps (2.65 on log scale) is 0.073 mWm^{-2} and 1 mWm^{-2}. These irradiances suggest that the impact of the non-

linearity is not significant and hence, therefore, the power penalty is less steeper than the power penalty observed in the case of the 30035.

Figure 4.3 also shows an estimation of the average irradiance (grey solid line) when the 60035 is used. As the lowest data rate transmitted at SiPMs is equal to 200 Mbps (2.3 on log scale), which suggest that the ratio of the 3dB bandwidth to data rate is equal to 0.42 in the case when the 60035 is used. This ratio is slightly less than the ratio of 0.5 at which the system does not encounter a significant ISI power penalty. However, the ratio decreases as the data rate goes higher than 200 Mbps. Therefore, expectedly, the measured average irradiance (grey diamond) deviates significantly from the estimated average irradiance (grey solid line) at higher data rates. Furthermore, the reason to transmit the lowest data rate at 200 Mbps is because of amplifier's lower cut-off frequency, which is equal to 10 MHz. The use of dc balancing scheme such as 8b10b encoding may also encounter signal attenuation due to the amplifier's lower cut-off frequency when transmitting a lower data rate such as 100 Mbps. The absolute worst case run-length of consecutive equal bits in the 8b10b coding is 5. For instance, if a bit pattern …0111110… or ...1000001… occurs in the transmission, ideally, the bandwidth (BW_p) required to transmit such pattern can be calculated based on the following Equation 4.2 [77]

$$BW_p(n_{bc}) = \frac{0.5}{T_b \times n_{bc}} \tag{4.8}$$

where n_{bc} is the number of consecutive bits e.g., 1s or 0s in a time of interest and T_b is the bit duration. In the example bit patterns discussed above, the number of consecutive (n_{bc}) is equal to 5. Hence, the bandwidth required to transmit this type of pattern calculated is equal to 10 MHz when the data rate is 100 Mbps. However, the power amplifier (FMAM3269) in the transmitter chain has a lower cut-off equal to 10 MHz, which means that it is not suitable to transmit a data rate around 100 Mbps as the signal may encounter significant attenuation due the lower cut-off of the power amplifier.

4.4.2 Results with equalisation

The previous section observed how the 3dB bandwidth impacts the average irradiance required on the SiPM from the transmitter. In particular, when the ratio of the 3dB bandwidth to a data rate is higher than 0.5 or when a data rate is higher than the twice the 3dB bandwidth is transmitted at the SiPM, an ISI power penalty is incurred. As discussed in section 2.5, the ISI occurs when the channel behaves as a band-limited filter and causes the transmitted signal to distort. To avoid ISI and the need of power penalty, the signal can be equalised at the receiving end. There are various techniques, such as linear equalisation (LE) and decision-feedback equalisation (DFE) that can be used to perform equalisation. Typically, a digital filter is used as a channel equaliser, which correct the signal distortion (or ISI) by selecting its number of taps and tap weights, which typically are adapt by adaptive algorithm [96].

To measure the performance of both SiPMs as VLC receivers with equalisation, decision feedback equalisation was used. The DFE is a nonlinear equaliser, typically consisting of a feedback filter, a forward filter, and a detector that uses previous detector decisions to eliminate the ISI [97]. Unlike linear equalisation, the DFE does not enhance the noise and amplifies the high-frequency components [98], [99]. The optimised structure of DFE gives better performance as compared to the linear equalisation [96].

MATLAB's built-in decision feedback equalisation (DFE) is used to see the impact of equalisation. The 'dfe' function in MATLAB creates an equaliser object and is used with a function called 'equalize' to perform equalisation. The optimum number of feed forward and feedback taps required by the DFE at a given data rate has been searched through a range of values. The weights of these taps were then determined using the recursive least squares (RLS) algorithm, which is an option within the MATLAB DFE function. Subsequently, the equalised signal is then used to calculate the BER using the same procedure, described in section 4.4.1. However, if the

achieved BER is not equal to the target BER then the process is repeated until the target BER is achieved by varying the irradiance at the SiPM.

Figure 4.5 (i) shows examples of eye diagrams of signals received at different data rates with and without equalisation when the 30035 is used. From Figure 4.5 (i), it can be seen that there isn't a significant difference between eye diagrams at 500 Mbps, as the impact of ISI at this data rate is not important. However, the benefit of equalization can clearly be seen at higher data rates, such as at 1 Gbps and 2 Gbps.

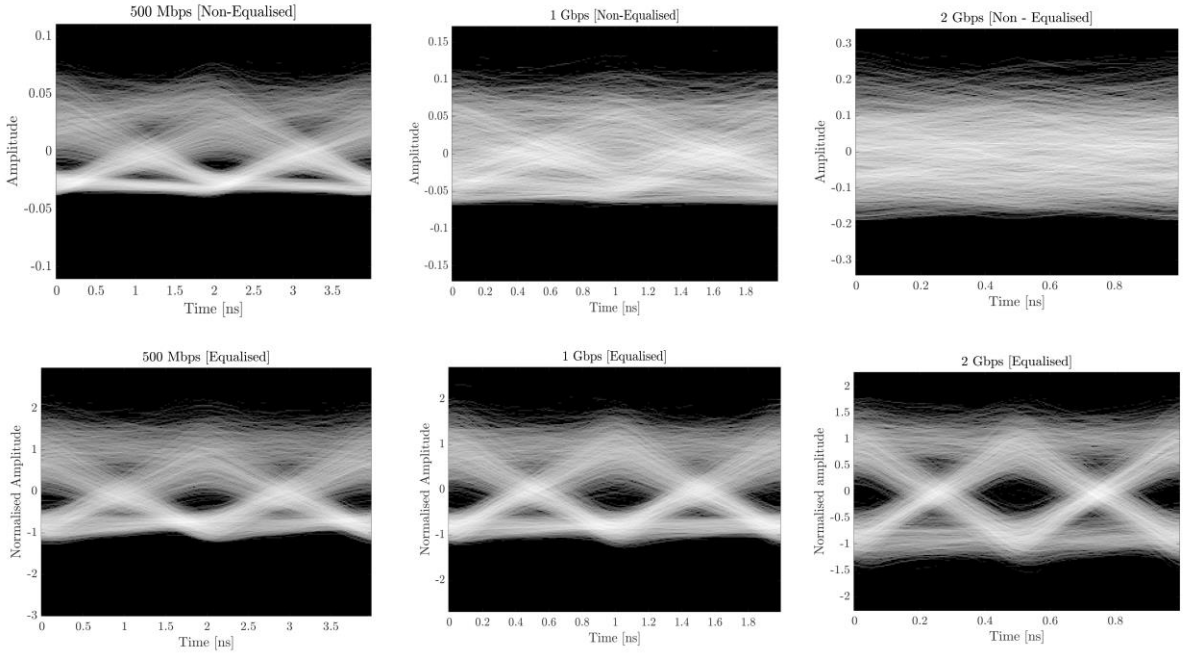


Figure. 4.5 (i) Eye diagrams of the signal received at 500 Mbps (left), 1 Gbps (middle), and 2 Gbps (right). Eye diagrams in the top row show signal without equalisation, and diagrams in the bottom row show signal with equalisation when the 30035 is used as a VLC receiver

Furthermore, Figure 4.6 compares the average required irradiance (diamond) without equalisation and the average required irradiance (circle) with equalisation applied at the received signal. In the case of the 30035, the average required irradiance (black diamond) without equalisation shows a rapid growth when the data rate is 500 Mbps. This growth is mainly due to the impact of ISI present in the system. However, when the equalisation is applied at the received signal, ISI is compensated and as a result, the average required irradiance varies approximately

with a constant slope from 200 Mbps until 1.4 Gbps. Also, it can be noticed that before ISI starts to impact on the average required irradiance i.e. at data rates from 200 Mbps to 500 Mbps, the equalisation has no significant impact. A linear fit (black dashed) to the average required irradiance shows that the slope is equal to 0.9. However, a significant change in the slope of the average required irradiance is observed when the data rates is higher than 1.4 Gbps. The linear fit (black dashed-dotted) shows that this slope is equal to 3.2. The fit to the average required irradiance can be described using the following expression

$$log_{10}Irradiance\ (mWm^{-2}) = m \times log_{10}DR(Mbps) + c \tag{4.8}$$

where m is the slope and constant c varies with slope. Table 4.1 summarises values used for each fit shown in Figure 4.6.

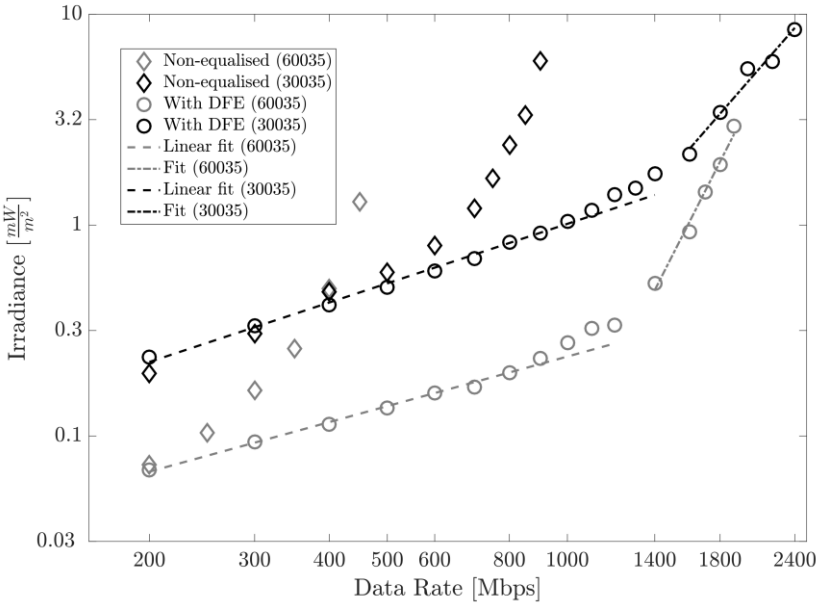


Figure. 4.6 Data rate vs. average irradiance required by the 30035 and 60035 to achieve a target BER of 1×10^{-3} in the dark

The abrupt change in the slope of the average required irradiance over 1.4 Gbps can be investigated using an ideal characteristic required by an OOK receiver to achieve a target BER at a given data rate without being impacted by the ISI power penalty. For a case when the data rate is 1.4 Gbps, ideally, a ratio between the 3dB bandwidth to the data rate should be equal to 0.5,

which has been already discussed in section 4.4.1. Therefore, to transmit a data rate of 1.4 Gbps without the impact of ISI, a 3dB bandwidth of 700 MHz is required. However, from the measured frequency response (dashed line) shown in Figure 4.2, it can be seen that at around 700 MHz, the response of the link varies significantly, where the drop from –17 to –32 dB. This means that at around 700 MHz, the noise in the system dominates and a significant power penalty is required by the equalisation. Hence, as a result the slope of the average required irradiance to increase from 0.9 to 3.2 when the data rates is higher than 1.4 Gbps. The power penalty at these data rates has been discussed in section 4.4.3. Moreover, the average irradiance required at higher data rates means that the SiPM is operating in the non-linear region, which also impact the average required irradiance.

A similar behavior has been observed when the 60035 is used. From Figure 4.6, it can be seen that with using the equalisation, the average required irradiance (grey circle) increases linearly up to 1.2 Gbps (3.079 on log scale) with a similar slope (shown as the grey dashed line) as observed in the case of the 30035. However, the slope changes significantly from 0.9 to 5.6 when the data rate is above 1.2 Gbps. As discussed earlier, this abrupt change in the slope (grey dashed-dotted line) is related to the frequency response of the system. From Figure 4.2, it can be seen that when the 60035 is used, the measured frequency response (grey dotted line) shows significant variations in the response around 600 MHz. However, these variations are more

Name of the fit	Slope (m)	Constant (c)
Black dashed	1	-3
Black dotted-dashed	3.2	-10
Grey dashed	0.9	-3.2
Grey dotted-dashed	5.6	-17.8

Table 4.1 Slope and constant value of fits shown in Figure 4.6

significant than observed for the 30035. Hence, a significant power penalty is required to equalise

the received signal. As a result, the slope of the average required irradiance in the case of the 60035 is more significant than the slope observed for the 30035 at higher data rates. Furthermore, it can be noticed that the equalisation marginally impacts on the average required irradiance at 200 Mbps when compared to the average irradiance required when no equalisation is applied. This means that the impact of ISI is not significantly at this data rate. It has been also noticed that despite of lower 3dB bandwidth, the 60035 requires a lower average irradiance compared to the 30035 when used with equalisation.

4.4.3 Equalisation results and estimation of the average irradiance

In section 4.4.1, it is observed that without equalisation, a power penalty is required to achieve the target BER when the data rate is higher than the twice the 3dB bandwidth of the system. The power penalty is primarily related to the ISI present in the system and can be calculated on the basis of the average irradiance estimated based on the Poisson stats. To observe the impact of the equalisation on the power penalty, results with equalisation has been compared to both the estimated average irradiance and results without equalisation. For this reason, the estimated average irradiance has been extended to higher data rates as shown in Figure 4.7.

Figure 4.7 compares the measured average irradiance (circle) with equalisation to the average irradiance (solid line) estimated based on Equation 4.3 and results without equalisation. From Figure 4.7, it can be seen that the estimation for the 30035 (black solid line) fit well to results without equalisation (diamond) up to 500 Mbps and with (black circle) up to approximately 1.1 Gbps. However, it can be noticed that when equalisation is employed, the average irradiance deviate from the estimated when the data rate is higher than 1.1 Gbps. In other words, when the ratio between the 3dB bandwidth and data rate is approximately 0.2 as shown in Figure 4.8, the power penalty (black square) increases rapidly. However, without equalisation, the power penalty

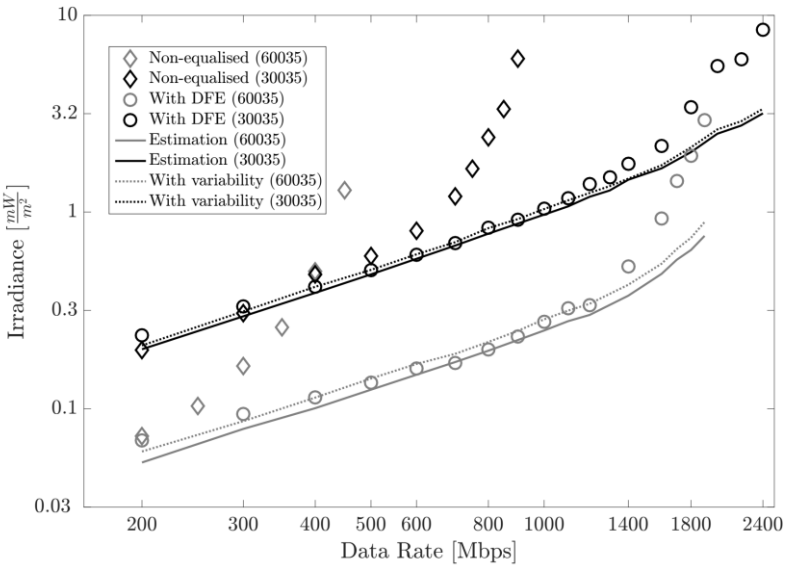


Figure 4. 7 Data rate vs. average irradiance required by the 30035 and the 60035 when evaluated the performance in the dark and the DFE (circle) is applied on the received signal

start to impact the average irradiance when the ratio was equal to 0.5. Hence, Figure 4.8 shows the advantage of using the equalisation and its impact on the power penalty.

On the contrary, when comparing the measured average irradiance (grey circle) to the estimated average irradiance (grey solid line) in Figure 4.7, it can be seen that the first two data

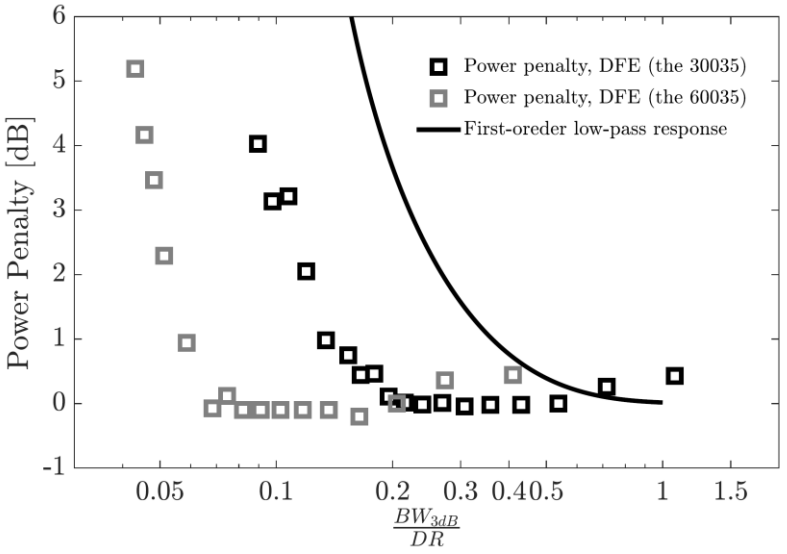


Figure 4.8 Power penalty of the 30035 and 60035 with equalisation vs. the ratio of 3dB bandwidth and data rate. The solid line shows the power penalty of the first-order low-pass system

points i.e. measured at 200 Mbps (2.3 on log scale) and 300 Mbps (2.477 on log scale) have deviated from the estimation despite of using the equalisation. The equalisation means that the power penalty required at the first two data is not related to the ISI and the impact of non-linearity of the 60035 is also negligible as the average required irradiances are low enough. However, it can be observed that as the data rate reaches 400 Mbps (2.6), the estimation starts to fit to the measured up to 1.2 Gbps (3.079). So far, the only thing, which changes in the estimation as the data rate increases is the background counts per bit and hence the average number of required photons per bit. For this reason, dark counts data of both the 30035 and the 60035 have been investigated. Figure 4.9 shows distributions of integral of approximately 500 primary dark pulses captured from the fast output of the 30035 and the 60035. The statistics of these distributions is described in the caption of Figure 4.9. From the statistics of the 30035, their dark pulses vary by a factor of 1.16 from the mean value according to one standard deviation ((1σ)). Similarly, in the case of the 60035, the pulses are variable by a factor of 1.4 when the high side of the distribution is considered for one standard deviation. In particular, a dark pulse may counted as 1.16 count per pulse for the 30035 and 1.4 for the 60035 when the high side of the distribution is considered.

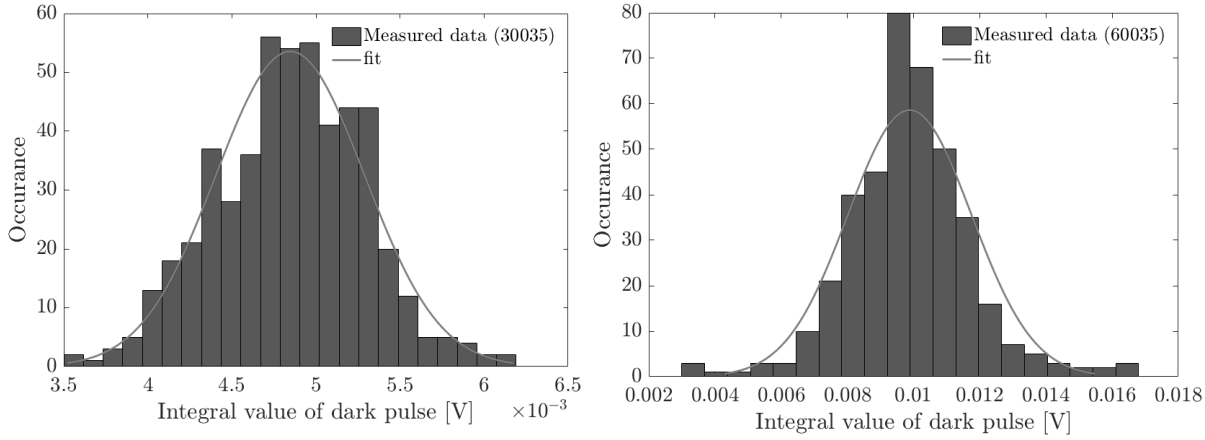


Fig. 4.9 Distribution of dark pulses captured from the fast output of the 30035 and the 60035. Solid line shows Gaussian fit to the distribution with mean (μ) and standard deviation (1σ) equal to 4.84×10^{-3} and 7.9×10^{-4} for the 30035, and 1×10^{-2} and 4×10^{-3} for the 60035 respectively

Hence, the same concept can be applied on the background count rate estimated for each data rate in section 4.4.1 and then average required irradiance can be re-estimated. Since the estimation (grey solid line) underestimates the average required irradiance, that is why the high side of the distribution is considered and applied the same factors to the background counts per bit and estimated the average required irradiance. The resulting estimation is shown as the grey dotted line in Figure 4.7 and it can be seen that it is more close to the measured average irradiance than the grey solid line up to approximately 1.2 Gbps. On the contrary, in the case of the 30035, it can be seen that there is no significant difference between the estimation (black solid line) and the estimation (dotted), which take into account the standard deviation of the 30035 for the number of background counts per bit while estimating the average required irradiance.

4.5 Impact of ambient light

As discussed in section 4.2, the aim is to demonstrate a VLC system, which works in conjunction with commercial white LED lamps, which are commonly used in most of the existing indoor environments such as study room, office, library workshop and/or auditorium. The performance of the 30035 has already been evaluated when it has been operated in an ambient light level of 500 lux and used a 10 nm wide narrow bandpass filter to reject the ambient light reported in [14], [45]. However, the field of view (FoV) of the filter was limited to ±10 degrees with a transmittance of 35% at 405 nm and at normal angle of incident (AOI). This is section is therefore discusses possibility of using various glass filters, which may provide a large of FoV because their spectral response is independent of the angle of incident. However, there is a trade-off between the impact of background from a warm white LED and the transmittance of 405 nm transmitter at the SiPM for a particular glass filter or a combination of glass filters. Therefore, this trade-off are also discussed in this section.

In chapter 2, it has been observed that the warm white LED may significantly impact the performance of a SiPM, where its impact depends upon the lux level or the total illuminance over

a range of wavelength. From Figure 2.8, it can be seen that at shorter wavelengths i.e. shorter than 420 nm, the intensity counts of warm white LED are negligible and similarly these are negligible at wavelength longer than 750 nm. For this reason, a range of glass filters from Edmund Optics are selected on the basis of their potential to reject the ambient light ranging from 420 nm to 750 nm and their transmittance at 405 nm. Figure 4.10 shows the transmittance profile of selected filters at a range from 390 nm to 780 nm, which covers a entire portion of the warm white LED. Their important characteristics such as thickness and transmittance at a wavelength of 405 nm are tabulated in Table 4.3. From the figure, it can clearly be seen that the UG5 has barely a transmittance of about 20% at 420 nm and absorbs wavelengths greater than 420 nm up to approximately 650 nm. Similarly, HoyaB370 has a transmittance of about 40% at 420 nm and then decline steeply, where it has a transmittance of less than 1% at 470 nm and absorb longer wavelengths up to approximately 680 nm. This means that both are good candidate to filter out blue to red part of the white LED. However, both UG5 and HoyaB70 have a less transmittance at 405 nm as compared to the other filters in the list. On the contrary, BG3 in the list has a

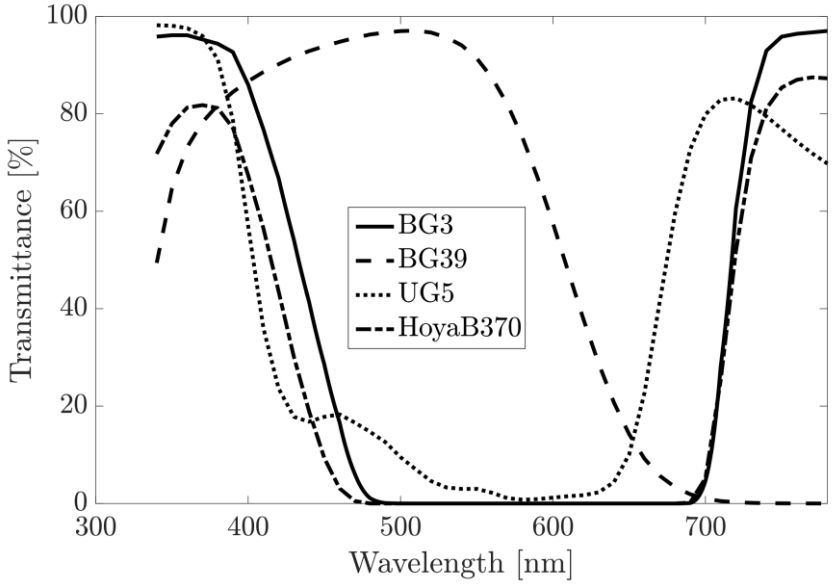


Figure 4.10 Transmittance of various glass filters at a range of wavelengths. The transmittance data of these glass filters is extracted from their datasheets provided by Edmund Optics

transmittance at 405 nm more than 80%, however, the filter may allow a significant part of the blue light of the WLED due its high transmittance in the blue region. A combination of these filters is therefore is an appropriate choice to rejection of most of the blue, green, yellow and some of the red part of the white LED. However, a drawback of combining these filters is the transmittance at 405 nm and rejection of wavelengths longer than 680 nm. Hence, BG39 seems to be appropriate a choice in the combination, which can be used to filter out the impact wavelengths longer than 680 nm.

Since the aim is to evaluate the impact of ambient light on a SiPM using these glass filters when the background illuminance is equal to 500 lux. For this reason, a spectral irradiance of warm white LED, which is equivalent to approximately 500 lux is estimated from [100]. The spectral irradiance is shown in Figure 4.11 and its equivalence to luminous flux per square-merer can be converted using the following relation [101], [102]

$$\phi_v = K \times \int_{\lambda=390nm}^{\lambda=780nm} I_{rr}((\lambda)\, V((\lambda) d\lambda \tag{4.9}$$

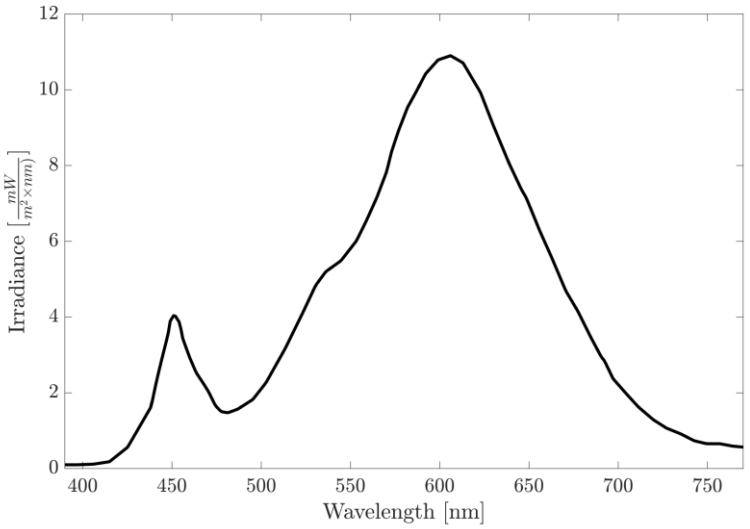


Fig. 4.11 Spectral irradiance of warm white LED at a range of wavelength. The data is taken from [100]

where, irradiance I_{rr} is the optical power in watts per square meter per nanometer (Wm^{-2}/nm), K is the luminous efficacy equal to 683 lumens per watt (lm/W) and $V(\lambda)$ is the luminous efficiency, which can be expressed as [102]

$$V(\lambda) = 1.019\ \mathrm{e}^{-285.4\left(\lambda_{\mu}-0.559\right)^{2}} \tag{4.10}$$

λ_{μ} is the wavelength in micrometer. To calculate the luminous flux at a particular wavelength, the irradiance (I_{rr}) at that wavelength can be multiplied by the luminous efficacy (K) and luminous efficiency ($V(\lambda)$). Figure 4.12 shows the luminous flux at a range of wavelength. The total luminous flux is equal to 500 lumens per square-meter calculated using Equation 4.9, where 1 lux is equal to 1 lumen per square-meter (1lm/m^2).

To observe the impact of the warm white LED on the SiPM when it generates 500 lux, the spectral irradiance of the warm white LED needs to be converted to the incident photons rate ($r_{incident}$) using Equation 3.6 Subsequently, the incident photon rate of each wavelength is then multiplied by the PDE of the SiPM corresponding to that wavelength and then the background

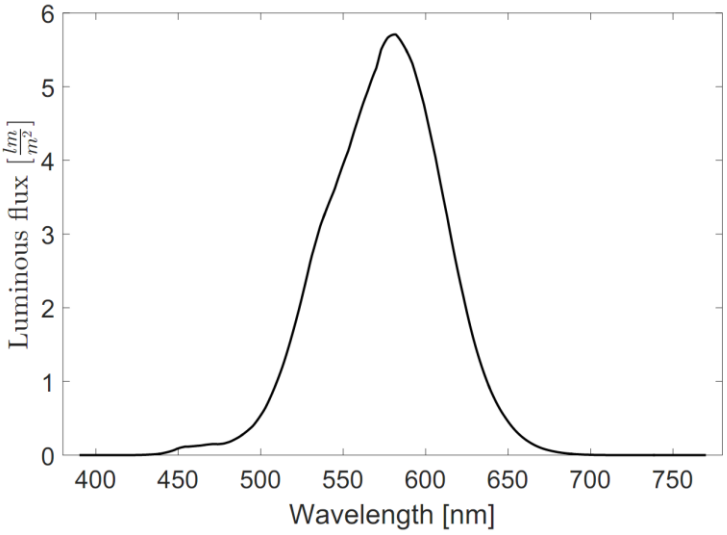


Fig. 4.12 Luminous flux at a range of wavelength converted from the spectral irradiance of the warm white LED using Equation 4.9

count rate is estimated. The PDE of the SiPM at a range of wavelengths is estimated from the J-Series datasheet. Similarly, the estimated background count rate can be multiplied by the transmittance of the glass filter or a combination of glass filters to see its impact on the SiPM. Table 4.4 summarises the results of the overall background count rate with a glass filter and a combination of glass filters. The overall background count rate ($r_{background}$) is obtained by integrating the background count rate over a range of wavelengths and can be calculated using the following relation

$$r_{background} = \int_{\lambda=390nm}^{\lambda=780nm} r_{incident}(\lambda) \times PDE(\lambda) \times \tau_i(\lambda) d\lambda \quad (4.11)$$

where $r_{incident}$ is the incident photon rate and τ_i is the transmittance of a glass filter or a combination of glass filters. From Table 4.4, it can be observed that when a single glass filter is considered, the estimation of the overall background count based on Equation 4.11 is a significant factor of

Glass filter type	Measured current of the 60035 [mA]	Transmittance at 405 nm [%]	Estimated overall background count rate [Gcps]		
			Equation 4.11	Equation 3.7	Ratio
No filter	77	100	25347	117	216.6
BG3	59.3	81	1340	90	15
BG39	-	88	16439	-	-
UG5	64	46	2643.8	97.3	27.2
HoyaB370	54.6	62	717	83	8.7
2×BG3	48	66	628	73	8.6
(2×BG3)×HoyaB370	-	41	277	-	-
HoyaB370×BG39	46.3	54	403.8	70.4	5.7
HoyaB370×BG3	46.5	50	403.2	70.7	5.7
(2×BG3)×BG39	38.3	58	368	58.2	6.3
BG3×HoyaB370×BG39	26.78	44	184	40.7	4.5
(2×BG3)×HoyaB370×BG39	15	36	99	23	4.3
(2×BG3)×HoyaB370×(3×BG39)	-	28	80.7	-	-
BG39×HoyaB370×UG5	-	25	89.5	-	-
(2×BG39)×HoyaB370×UG5	-	22	81.1	-	-
(2×BG3)×(2×BG39)×UG5	-	24	76.4	-	-
BG3(1mm)×BG39×HoyaB370×UG5	-	24	70.7	-	-
BG3(2mm)×BG39×HoyaB370×UG5	-	22	57.2	-	-
BG3(3mm)×BG39×HoyaB370×UG5	-	20	47.4	-	-

Table 4.3 The transmittance of various glass filters and combinations of glass filters at 405 nm and their estimated detected count rate for the 60035 at a range of wavelength of the warm white LED

the count rate estimated from the measured SiPM current using Equation 3.7. However, in practice, the SiPM has a limited dynamic range due to its non-ideal effects, which have been discussed in chapter 3, and therefore limit the maximum detectable count rate. Based on the non-paralysable model (Equation 3.11), the maximum detectable count rates estimated for the 30035 and 60035 are 48.5 Gcps and 124 Gcps respectively. Ideally, the detected count rate of the 60035 can be converted to the count rate of the 30035 by multiplying the count rate to the ratio of the total number of microcells of the 30035 to the 60035. Apart from that, the WLED lamp obeys the Lambert's law, and exhibit Lambertian reflectance, which means that the irradiance on the SiPM is proportional to the angle between the direction of the incident light and the surface normal and therefore may vary significantly with the effective angle [103]. Moreover, the irradiance may also vary with the effective refractive index a glass filter or a combination of glass filters and thus using a simple method overestimate the overall background count rate. For this reason, the SiPM current has been measured for a few glass filters and combination of glass filters to see the impact of the ambient light.

The measured SiPM current and an estimation of background count rate based on the measured SiPM current when a single glass filter is used suggests that the use of a single glass filter is likely to saturate the SiPM. Therefore, various combinations when each include two, three and then four glass filters of different thicknesses have been used to estimate the overall background count rate. From the table, it can be seen that the count rate reduces as the number of glass filters in a combination increases. However, correspondingly, the transmittance also reduces, which may significantly impact the irradiance required from the transmitter. Similarly, at higher transmittance, the detected count rate from the warm white LED will be higher, which again can significantly impact the irradiance required from the transmitter to achieve a target BER. Hence, there is a trade-off between the detected background count rate and the transmittance of the filter or a combination of glass filters. Therefore, the 60035 has been used to evaluate its

performance with a combination of glass filters and two combinations have been verified when a data rate of 1 Gbps is transmitted to achieve a BER of 1×10^{-3}. In [21], it has been shown that when the first combination, which include two BG3 and one BG39 filter is used, the SiPM current measured in the ambient light was equal to 38.3 mA and the SiPM requires an irradiance of 2.8 mWm^{-2}. Whereas, adding HoyaB370 in the combination reduces the SiPM current more than half (15 mA) the SiPM current measured with previous combination, and the SiPM requires an irradiance of 1.8 mWm^{-2} to achieve a BER of 1×10^{-3} [21]. Furthermore, it can be seen in Table 4.4 that adding further filters in the combination reduces the background count rate, however, the transmittance at 405 nm is also being compromised, which will result in a power penalty from the 405 nm transmitter. Therefore, a combination of two BG3, one HoyaB370 and one BG39 is a reasonable choice. The next section is therefore compares the performance of the 30035 and the 60035 with the selected combination of glass filters at a range of data rates when operating in the presence of ambient light.

4.6 Link results in ambient light

To evaluate the performance of the 30035 and the 60035 in the presence of ambient light, two warm white LEDs (Philips IBRS 10461) have been added to the testbed, which generates 500 lux at the position of the SiPM. Moreover, instead for the narrow bandpass filter, a particular combination of glass filters, which has been discussed in the previous section, is selected to mitigate the impact of the ambient light. Figure 4.13 shows the average required irradiance by SiPMs to achieve a BER of 1×10^{-3} at a range of data rates in the presence of ambient light. The fit (dashed and dotted-dashed line) to the measured average irradiance is based on Equation 4.8. The slope (m) and constant (c) used for the each fit are listed in Table 4.5. From Figure 4.13, it can be seen that the slope (dashed line) of the average irradiance changes at around the same data rate as it has been observed when SiPMs were operated in the dark i.e. the slope of the

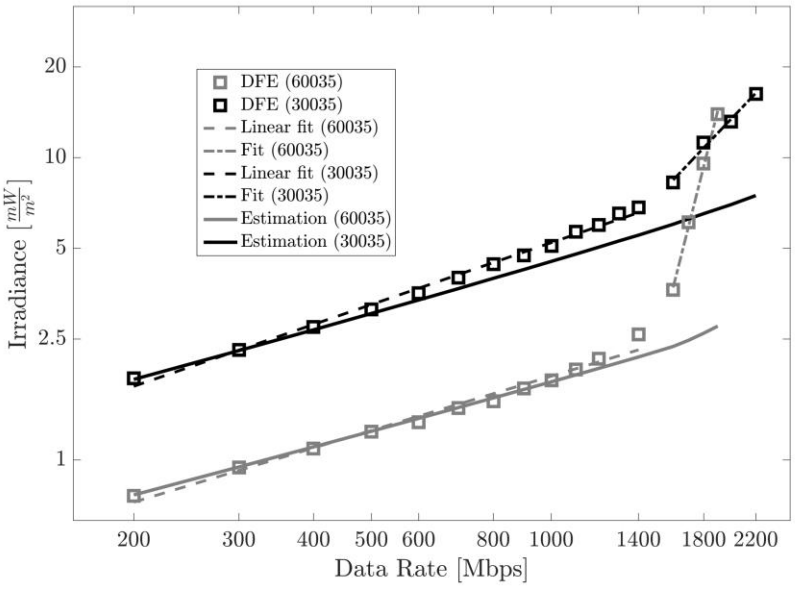


Fig. 4.13 Average irradiance required by the 30035 and the 60035 to achieve the target BER at a range of data rates when the equalisation is employed, and the ambient light level is equal to 500 lux

average irradiances changes at 1.4 Gbps and 1.2 Gbps for the 30035 and the 60035 respectively. At lower data rates, despite SiPMs are operated in 500 lux, no significant difference between the

Linear fit	Slope (m)	Constant (c)
Black dashed (30035)	0.7	-1.32
Black dotted-dashed (30035)	2	-5.7
Grey dashed (60035)	0.65	-1.5
Grey dotted-dashed (60035)	7.8	-24.5

Table 4.4 Slope and constant value of fits to average measured irradiance in Figure 4.13

slope in 500 lux and slope in the dark has been observed. However, at higher data rates (i.e. above 1.4 Gbps when the 30035 is used and 1.2 Gbps when used the 60035), a significant change in the slope is observed, which is related to the link noise, which dominates at higher data rates, and non-linearity of the SiPM, which depends upon the average irradiance required. For convenience, to observe the level of non-linearity of SiPMs, a ratio between the linear response and the measured SiPM current is shown in Figure 4.14. The average irradiance required by both

SiPMs at higher data rates corresponds to the non-linear region and it can be seen that above 1mWm^{-2}, the 60035 is more non-linear as compared to the 30035 at higher irradiances. Moreover, the frequency response of the link with the 60035 shows more variations at higher frequencies than the link with the 30035. Therefore, the 60035 has a steeper slope at higher data rates than the observed slope for the 30035.

The solid lines in Figure 4.13 show the average irradiance estimated using the same method, described in section 4.4.1 and Equation 4.3. However, to calculate the average number of photons per bit against the number of background counts per bit, the Gaussian statistic (Equation 2.9) is used instead of Poisson. The reason for using the Gaussian statistics is the detected background count rate, which is beyond the limit of the function used in MATLAB for estimating the average number of photons per bit based on the Poisson statistics. For this reason, in section 2.4.2, it is demonstrated that two statistics converge at higher background counts per

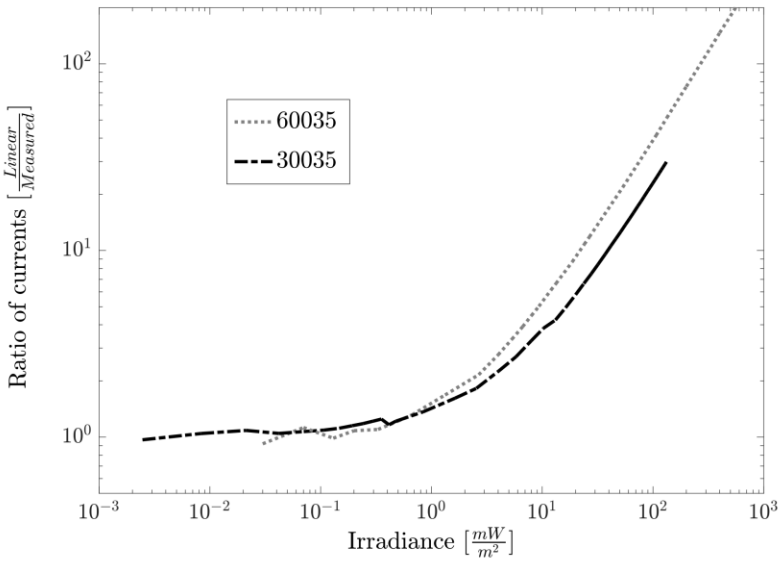


Figure 4.14 Ratio of the linear response to the measured SiPM current vs. the irradiance falling on the SiPM

bit. Both estimates (black and grey solid lines in Figure 4.13) are close to the measured average irradiance when the detected background count rate from the white LED only is equal to 90 Gcps

and 252 Gcps, respectively. However, in practice, both the 30035 and 60035 can't detect a background count rate of 90 Gcps and 252 Gcps, which are well above the maximum detectable count rate estimated for these SiPMs described in section 3.4.3. This means that other factors are involved, which may result in the average irradiance increasing significantly when SiPMs are operated in 500 lux. For instance, even with the best combination, a 15 mA of SiPM current with no data transmitted on the 60035 means that the SiPM is operating in the non-linear region. The impact of non-linearity gets even more severe as the average irradiance on the SiPM increases. Therefore, these factors must be studied to understand the unexpected increase in the required average irradiance.

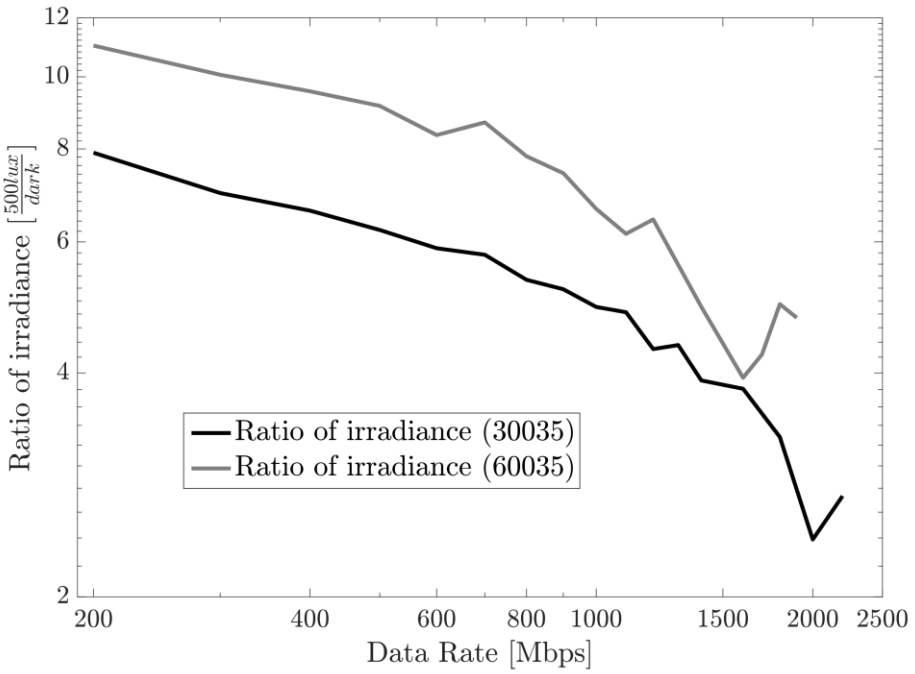


Figure 4.15 Ratio between the average irradiance required by the SiPM in 500 lux and in the dark at a range of data rates

A comparison between the average irradiance required by SiPMs in 500 lux and the average irradiance required in the dark is shown in Figure 4.15. Expectedly, due to the larger collection area, the 60035 seems more susceptible to the background light as compared to the 30035. It can be seen that at 200 Mbps, the 60035 requires an average irradiance almost 12

times more than it requires in the dark. Similarly, the 30035 requires 8 times more irradiance than it requires in the dark. However, as the data rate increases, the number of background counts per bit reduces and the average number of required photons per bit also reduces as observed in section 2.4.2. As a result, the ratio between the average irradiance required in ambient light and in the dark also reduces. However, at higher data rates a variation in the ratio is observed, which is related to the link noise and non-linearity the SiPM.

4.7 Comparison of irradiance

The comparison between the average irradiance required by the 30035 and the 60035 at a given data rate depends upon the value of irradiance, which may further depends upon factors such as linear and non-linear region of the SiPM and ISI power penalty. In a case, if both SiPMs are operating in the linear region, the average required irradiance is around 1 mWm^{-2} or less and do not encounter any ISI or equalisation power penalty then the 60035 would be almost 4 times sensitive than the 30035. However, as soon as any of the above factors starts to impact on the

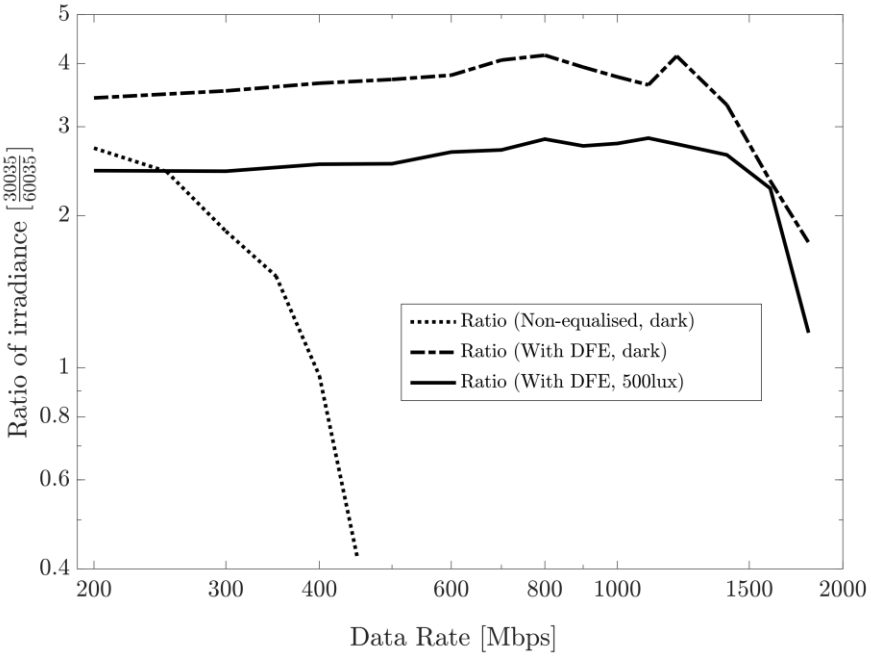


Figure 4.16 The ratio between the average irradiance required by the 30035 and the 60035 when operating in the dark with and without equalisation and in 500 lux with equalisation

performance, then their sensitivity will starts to degrade and as a result their sensitivity ratio will also degrade. Figure 4.16 shows that when the performance of both SiPMs are compared using their ratio (dotted line) of average required irradiance when they are operating in the dark without equalisation. Then, the 60035 starts to encounter ISI power penalty, which has been discussed in detail in section 4.4.1 at around 200 Mbps. Hence, their ratio (dotted line) decline rapidly as the data rate increases as shown in the figure. However, when the performance of both SiPMs is compared in the dark with equalisation, it can be seen that their ratio is maintained around 4 until approximately 1.4 Gbps. However, at data rates higher than 1.4 Gbps both SiPMs encounter non-linearity (discussed in chapter 3) and also their link response have variations at higher frequencies (shown in Figure 4.2), which creates a power penalty and result in their sensitivity to degrade and hence their ratio falls promptly at higher data rates. Similarly, when the average irradiance of both SiPMs are compared when they are operating in 500 lux, their ratio is maintained around 2.5 until the same data rate as observed in the dark with equalisation employed. Although, the of equalisation compensate the ISI power penalty, however, operating SiPMs in the presence of ambient light increase the number of background counts per bit and thus requires a significant factor of the average irradiance as compared to the avarege irradiance required in the dark, which has been discussed in the previous section. This cause both SiPMs to operate close to the saturation regions and therefor their ratio to reduce from 4 to 2.5. At higher data rates, the impact of non-linearity on both SiPMs is significant and as discussed earlier variations in the link at higher frequencies may also impact significantly on the performance. Hence, their ratio of average irradiance decline rapidly at higher data rates.

4.8 Summary

In this chapter, a method to set up a testbed to evaluate the performance of a SiPM-based VLC receiver in an indoor environment is presented. Two SiPMs of same microcell size, which differ in size, pulse width, and the total number of microcells are used to compare their performance

without and with equalisation in the dark. Also, methods are presented, which predict the performance in no ambient light and the presence of ambient light when used with various absorption filters.

The frequency response of the link is measured separately for the 30035 and 60035 when used with their fast output. The measured frequency response shows a 3dB bandwidth of 215 MHz and 80 MHz when the 30035 and 60035 are used. The relationship of 3dB bandwidth and data rate, discussed in section 2.5, suggested that in the case of the 30035, when the data rate is approximately 500 Mbps and higher, a significant power penalty will be required to maintain the BER. Similarly, in the case of the 60035, it was anticipated that the power penalty would start to rise when the data rater is around 200 Mbps or higher. Therefore, to avoid the impact of background light, results were first obtained in the dark. As expected, a rise in the power penalty is observed around 500 Mbps for the 30035 and around 200 Mbps for the 60035. However, the trend of power penalty deviates from the power penalty of the first-order low-pass system when the data rate is significantly higher than the 3dB bandwidth, discussed in section 4.4.1. The rise in the measured power penalty can also be anticipated by comparing the measured frequency response of the link to the first-order low-pass response. The measured frequency response of the link deviates from the first-order low-pass filter response at higher frequencies. However, the measured power penalty of the 30035 is steeper than the 60035. This is because the 30035 is operating in the non-linear region when the power penalty is significant. Whereas, in the case of the 60035, despite the impact of ISI, the SiPM operates in the linear region. Since the power penalty here is mainly due to the impact of ISI, this means that equalisation is required at higher data rates. It is worth noting that the power penalty at a data rate is calculated based on the estimated average irradiance (Equation 4.3) required by the SiPM. Moreover, when comparing the sensitivity of the 60035 to 30035, the 60035 is more sensitive than 30035 up to 350 Mbps.

However, above 350 Mbps, the performance of the 60035 starts to worsen compared to the 30035, which is mainly due to the impact of ISI.

The results obtained with equalisation are first compared to the average irradiance required by a SiPM without equalisation. In the case of the 30035, up to 500 Mbps, the equalisation has a marginal or negligible effect on the required average irradiance. However, above 500 Mbps, a significant reduction in the required average irradiance is observed compared to the required average irradiance without equalisation. Similar to the 30035, the required average irradiance by the 60035 reduced significantly above 200 Mbps compared to the results without equalisation. Another advantage of using equalisation is that the maximum data rate achieved equals 2.4 Gbps and 1.9 Gbps, respectively, when the 30035 and 60035 are used. Moreover, the sensitivity ratio between the 60035 and 30035 shows that the 60035 is 4 times more sensitive than the 30035 up to 1.2 Gbps when used with equalisation. However, at higher data rates, the sensitivity ratio starts to fall, which is related to the link noise, which dominates at higher data rates. The non-linear effects of SiPMs also significantly impact the sensitivity.

The results achieved in the dark have also been compared to the estimated average irradiance. For the 30035, both without and with equalisation results satisfy the estimated average irradiance up to 500 Mbps. Exceptionally, equalisation results are close to the estimated average irradiance until 1.4 Gbps. As discussed in the previous paragraph, the link noise and non-linearity of the 30035 become important at higher data rates. Hence, as a result, the required average irradiance with equalisation deviates from the estimated average irradiance. Similar behaviour has been observed for the 60035. However, unexpectedly, the estimation of the average irradiance is underestimated at lower data rates, which is related to the pulse variability of the 60035 discussed in section 4.4.3. Later, when the variability is considered in the estimation, results show that the estimated average irradiance is close to the measured average irradiance at lower data rates.

Subsequently, the performance of SiPMs in the presence of ambient light was evaluated using absorptive filters. The advantage of using absorption filters is that their spectral response is independent of the incident angle and hence may provide a wide FOV. Before evaluating the performance of SiPMs in the presence of ambient light, the impact of warm white LED, which generates 500 lux, is predicted at a range of wavelengths. Section 4.5 discusses the method, which uses the transmittance of a glass filter or a combination of glass filters at 405 nm, and the PDE of the SiPM to evaluate the detected background count rate. From the results of detected background count rate and transmittance, it has been concluded that a combination of glass filters including two BG3 (3 mm), HoyaB370 (2.5 mm), and BG39 (1 mm) is a suitable choice, which is then compared to a few other combinations at a data rate of 1 Gbps. The selected combination has provided better results than other combinations and is then used to evaluate the performance of SiPMs at a range of data rates.

The results achieved in 500 lux when SiPMs are used with absorption filters to reject the ambient light show that the required average irradiance increases significantly compared to the average irradiance in the dark. However, the difference between the required average irradiance in 500 lux and dark reduces as the data rate increases, mainly due to the reduction in the background counts per bit. Furthermore, the sensitivity ratio between the 60035 and 30035 falls to approximately 2.5 when operating in 500 lux. This is because the required average irradiance in the presence of ambient light causes both SiPMs to operate in the non-linear region. This ratio is maintained until 1.4 Gbps; however, at higher data rates, the link noise and non-linearity of SiPMs dominate and thus the sensitivity ratio between the 60035 and 30035 reduces to 1.2 at 1.8 Gbps. Despite the impact of background, bandwidth, and non-linearity, it is observed that the 60035 is still more sensitive than 30035. However, with some improvements in the effective recovery time and pulse width, the 60035 can achieve even better sensitivity.

Chapter 5

Conclusion and Future Work

5.1 Summary

In indoor wireless communication, visible light communication has the potential to complement RF systems and to overcome the problems associated to crowded RF spectrum. However, VLC systems require a high bandwidth, wide FOV, and sensitive receivers, which are able to support at least a few Gbps of data rate using an average irradiance, which is eye and skin safe. Over the past decade, several APD-based VLC receivers have been reported, which are able to support a transfer rate in the range of Gbps. However, their collection area is typically less than a square millimeter. In addition, the excess noise generated by the avalanche multiplication, limit the APD gain to a few of hundred and hence its sensitivity as discussed in section 1.3. Moreover, due to the limited sensitivity, APDs require irradiance, which may be higher than the eye-safe limit.

On the contrary, a SiPM avoids the excess noise factor by operating each microcell in the SiPM in Geiger-mode as a single-photon avalanche diode. SiPMs are sensitive enough to detect a single photon and can be used as a sensitivity VLC receiver. However, in practice, the sensitivity of a VLC receiver may significantly be influenced by the background counts. Section 2.4.2 shows the theoretical performance of an OOK photon-counting receiver in terms of the average number of required photons per bit to achieve a particular BER at a range of background counts per bit. From the results in Figure 2.5, it has been observed that the average number of required photons per bit increases at a slower pace as compared to the number of background counts per bit. Therefore, it has been anticipated that a SiPM with a larger collection area would be more sensitive than the SiPM with a smaller collection area as long as the pace of the average number of required photons per bit is maintained slower than the background counts per bit.

To study the impact of collection area, and other parameters such as output pulse width or bandwidth and dynamic range on the performance of a SiPM as VLC receiver, J-Series 3 mm by 3 mm, and 6 mm by 6 mm from onsemi$_{TM}$, both have 35 µm pitch are selected. Apart from their difference in the collection area, these SiPMs are selected due to their fast output pulse width. However, since, the aim was to study and evaluate the performance of SiPM-based VLC receivers in an indoor environment. Therefore, prior to characterising and evaluating their performance as VLC receivers, spectra of white LEDs have been studied. Both warm and cool white LED spectrum show that their intensity is negligible at shorter wavelengths i.e. at around 400 nm. This means that if longer wavelengths are filtered, the data can be transmitted at around 400 nm. Moreover, another advantage of using a shorter wavelength is that SiPMs are more sensitive to shorter wavelengths as compared to longer wavelengths. Consequently, a laser diode, which has a wavelength centred at 405 nm is preferred for the transmission of data.

The PDE measured at 405 nm is approximately 40% when SiPMs are biased at 28 V, which is the optimum bias voltage discussed and is in section 3.4.3. The optimum bias voltage is searched at which the impact of non-ideal effects such as cross-talk and after pulse probability is minimum while maintaining a PDE, which is comparable to PDE at the maximum bias voltage applied. Subsequently, the average standard output is measured to study the effective recovery time, which is important to predict the dynamic range of a SiPM. The dynamic range is an important term, which determines the linearity of a SiPM against a range of irradiance falling on its active area. The dynamic range typically depends upon the total number of microcells, PDE, and effective recovery time. Therefore, the dynamic range of a SiPM can be predicted in terms of its current against a range of irradiance. There are two models used in estimating the SiPM current. The first model uses the paralysable count rate (Equation 3.8) and the second is the non-paralysable (Equation 3.11). While comparing the estimated current (Equation 3.7) to the measured in Figure 3.11, it has been observed that the non-paralysable model approximates the

response of the SiPM more accurately than the model based on the paralysable count rate. This means that SiPMs are of non-paralysable type. Moreover, it is also observed that the response of both SiPMs is linear up to approximately 1 mWm^{-2}. In the linear region, as expected from the difference in the number of microcells and active area, the ratio of sensitivity between the 60035 and 30035 is equal to 4 approximately. However, as the irradiance falling on SiPMs is over 1 mWm^{-2}, their response is entering the non-linear region, the ratio of sensitivity starts to fall and saturate at around 2.5 when the irradiance is around 100 mWm^{-2}. This suggests that to achieve the maximum sensitivity and to maintain the highest ratio of sensitivity, SiPMs should be operated in the linear region.

The performance of SiPMs was first evaluated in the dark to minimise the impact of background. The target BER is preferred for the evaluation of SiPMs as VLC receivers is equal to 1×10^{-3}, which has been discussed in detail in section 2.4.1. However, prior evaluating the performance link frequency response was measured separately for each SiPM to determine the 3dB bandwidth. The bandwidth of the system can be used to predict the ISI power penalty required at a given data rate. In a first-order low-pass system, the relationship of bandwidth and data rate suggests that when their ratio is less than 0.5, a more than 0.5 dB of power penalty is required to maintain the BER. The 3dB bandwidth of the system when the 30035 and 60035 are used is around 215 MHz and 85 MHz respectively. The bandwidth and data rate relationship suggests that a significant power penalty will be required by the 30035 and 60035, respectively, when the data rate is around 450 Mbps and around 200 Mbps. As expected, results obtained in the dark (Figure 4.3) show that the average irradiance required deviates from the estimated average irradiance (Equation 4.3) at around 500 Mbps and 200 Mbps for the 30035 and 60035, respectively. The deviation of the average required irradiance from the estimated average irradiance is due to the impact of ISI, which causes a power penalty to maintain the target BER when the data rates are high and comparable to the bandwidth of the system. Despite the impact

of the ISI power penalty, it was observed that the 60035 is better than the 30035 up to 350 Mbps. However, due to the impact of ISI when the 60035 is used, the ratio of sensitivity between the 60035 and 30035 is not equal to 4. Therefore, when operating in the dark, the 60035 is better only at lower data rates, i.e., less than 200 Mbps where the ISI is not significant. However, above 350 Mbps, the 30035 is preferred. Therefore, the results in the dark (Figure 4.3) mainly show the impact of ISI in relation to data rate and bandwidth and suggest that equalisation can address the impact of ISI at higher data rates.

The results with equalization (Figure 4.6) show that when the 30035 is used, equalization marginally impacts the average irradiance required up to 500 Mbps. However, above 500 Mbps, equalization significantly reduces the average required irradiance compared to non-equalized results, and a maximum data rate of 2.4 Gbps is achieved. Similarly, for the 60035, with equalization, the average required irradiance reduces significantly over 200 Mbps compared to results without equalization, and also the achievable data rate increased to 1.9 Gbps. Another advantage of using equalization is that the sensitivity ratio between 60035 and 30035 is around 4 up to 1.2 Gbps. In other words, the 60035 is approximately 4 times more sensitive than the 30035 until 1.2 Gbps. However, at higher data rates, the link noise dominates, and the non-linearity of the SiPM result in a significant power penalty required to equalize the data. Thus, the sensitivity ratio between the 60035 and 30035 starts to fall, and it has been observed that even at the highest data rate (i.e. at 1.8 Gbps) at which both SiPMs can be compared, the 60035 is sensitive by a factor of 1.7 when compared to the 30035. This means that to obtain the maximum sensitivity due to a larger collection area, the 60035 should be operated in the linear region when used with equalization.

To evaluate and compare the performance of SiPMs when operating in an ambient light level of 500 lux, glass (absorptive) filters are preferred to filter the ambient light whilst maintaining a good transmittance at 405 nm. The advantage of selecting glass filters is that compared to

narrow-band interference filters, they can provide a wide FOV because their spectral response is independent of the angle of incidence. Before evaluating the performance of SiPMs in the presence of ambient light, a method has been studied, which predicts the performance of various glass filters and combinations of glass filters in terms of filtering the ambient light and transmittance at 405 nm described in section 4.5. The performance of filters shows an inverse relationship between the rejection of ambient light and transmittance at 405 nm. For instance, for 100% transmittance of 100% at 405 nm, the rejection of ambient light is insignificant in a way that the SiPM is likely to saturate. Whereas, with the maximum rejection of ambient light, the transmittance at 405 nm of a filter or a combination of filters will be compromised, resulting in a power penalty required from the transmitter. Therefore, a range of combinations of glass filters is evaluated at a single data rate discussed in section 4.5. Consequently, the best combination includes two BG3 (3 mm), one HoyaB370 (2.5 mm), and one BG39 (1 mm) filter provide a 36% transmittance at 405 nm with an adequate rejection of ambient light has been used to evaluate the performance of SiPMs a range of data rate.

The results in 500 lux (Figure 4.13) show a similar trend of the required average irradiance for both SiPMs as observed in the dark. However, the requirement of average irradiance is increased by a factor of 8 and 12 almost at 200 Mbps for the 30035 and 60035 respectively, compared to the average irradiance required in the dark. This increase in the required average irradiance is due to the impact of background, which is causing SiPMs to operate in their non-linear region. Hence, a higher irradiance is required to maintain the BER. Since the number of background counts per bit reduces as the data rate increases, the ratio of the average irradiance required in 500 lux to dark also reduces accordingly. However, even at the highest data rate, this ratio is more than by factor of 4 at 1.9 Gbps for the 60035 and factor of 2 at 2.2 Gbps for the 30035. Moreover, it has also been observed that due to the impact of background and non-linearity, the sensitivity ratio between the 60035 and 30035 is reduced to 2.5. This sensitivity ratio

is maintained until 1.4 Gbps, which at higher data rates reduced to approximately 1 at 1.8 Gbps due to the significant variation in the link response. Although, despite the impact of background and non-linearity, the 60035 is still more sensitive than the 30035 at data rates lower than 1.8 Gbps. However, to achieve the maximum sensitivity due to a larger collection area of the 60035, the background from ambient light is required to be minimized further up to a level where non-linearity of SiPMs can be avoided. Also, the transmittance of a filter at 405 nm should be as high as possible.

5.2 Future work

One of the problems, which is inherent to VLC systems is that a VLC receiver must be in line-of-sight (LOS) from the transmitter. A VLC receiver, which is not in the LOS or if its orientation is equal to and greater than 90 degrees from the normal angle of incidence of light. Then, the receiver may likely receive weaker diffuse reflections from the surrounding. The photon-counting nature of SiPMs suggests that SiPMs can potentially support data reception in an indoor environment using diffused reflections, where LOS is not possible. An initial test can be performed using the same testbed, which has been used in this work and described in section 4.2 to evaluate and compare the performance of both the 60035 and 30035 SiPMs in a scenario, where the SiPM receives light reflected from objects. Initially, the performance can be evaluated in the dark by changing the orientation of the receiver at various angles, where only a single transmitter transmits the data. Subsequently, multiple transmitters can also be added in the testbed to improve the coverage.

The impact of background light on the performance of SiPM-based VLC receivers has been discussed in section 4.5, 4.6, and 4.7. In section 4.7, it has been observed that despite using the best combination of glass filters, SiPMs have been operating in the non-linear region, which causes the sensitivity ratio between SiPMs to reduce from 4 to 2.5. The primary reason for selecting this combination of glass filters is its adequate rejection of background count rate from

the white LED and an optimal optical transmittance of 36% at 405 nm. However, it is essential to note that a trade-off between the rejection of background and transmittance at 405 nm is also observed while estimating the background count rate with various combinations of glass filters. A few combinations, which have been discussed in section 4.5, show a further reduction in the background count rate, where the transmittance at 405 nm will be compromised significantly. Reducing the background count rate can avoid SiPMs operating in the non-linear region. However, due to the low transmittance, a power penalty will be required from the transmitter. Therefore, the power penalty due to transmittance of combinations needs to be investigated, which can then be compared to the power penalty required due to the non-linearity of SiPMs, and high background count rate. This will allow selecting a power penalty, which is farthest from the eye-safe limit.

Fluorophore-doped elements such as fluorescent fibres can also be used with SiPMs as wide FOV optical filters. These absorb light of some particular wavelength and emit light at a particular longer wavelengths, and can also be used as concentrators. For example, a VLC receiver that incorporates a 9 mm^2 SiPM (Onsemi$_{TM}$ J-series 30020) has been coupled to 28, 12 cm lines of fluorescence fibres (Kuraray, CSF-81), which serves as a concentrator and wide FOV filter reported in [104]. The performance of this fibre-based receiver has been compared in 500 lux to a receiver, which uses absorption filters for filtering the ambient light. The fibre-based receiver is more sensitive than the receiver with an absorption filter up to 600 Mbps. However, the limited bandwidth of fluorescence fibres means that ISI becomes significant at higher data rates. Hence the average irradiance required by this overtakes the average irradiance required by the receiver with an absorption filter. Furthermore, with more than 60-degree rotation, the fibres arranged in the design encounter shadowing effect, which degrade the performance of the fibre-based receiver. This suggests that further fluorophore-based fibres need to be explored, which

have even higher bandwidth, and also the impact of various designs of fluorescent fibres are required to be studied when coupled to SiPMs.

Higher-order modulation schemes such as optical orthogonal frequency division multiplexing (OFDM) can also be used with SiPM-based VLC receivers to achieve even higher data rates. However, it is challenging to use OFDM with SiPM-based VLC receivers due to the non-linear effects of SiPM as OFDM requires a very high linear dynamic range [105], [106]. Recently, the performance of the 30035 using OFDM modulation has been reported in [107]. The receiver requires an average irradiance of 2.55 mWm^{-2} to achieve a BER of 1×10^{-3} at 1.35 Gbps. The same SiPM requires an average irradiance of 2.3 mWm^{-2} to achieve this BER at 1.4 Gbps when used with OOK modulation, which is more robust to noise and simple to implement reported in [14]. This suggests that further study is required on using higher-order modulation schemes with SiPMs to achieve higher data rates, which compete OOK modulation's data rates. Other higher-order modulation schemes such as 4 level pulse amplitude modulation (4-PAM) and quadrature amplitude modulation (QAM) are also good candidates, which can be investigated using the existing testbed, which has been used in this project. However, to use OFDM with SiPMs, further work is required, including studying different techniques to cope with the non-linear effects of a SiPM.

The page left blank

References

[1] “Social media users pass the 4.5 billion mark - We Are Social Global.” https://wearesocial.com/blog/2021/10/social-media-users-pass-the-4-5-billion-mark/ (accessed Dec. 20, 2021).

[2] D. Karunatilaka, F. Zafar, V. Kalavally, and R. Parthiban, “LED Based Indoor Visible Light Communications : State of the Art,” vol. 17, no. 3, pp. 1649–1678, 2015.

[3] J. Reed, M. Vassiliou, and S. Shah, “The Role of New Technologies in Solving the Spectrum Shortage [Point of View],” *Proc. IEEE*, vol. 104, no. 6, pp. 1163–1168, Jun. 2016, doi: 10.1109/JPROC.2016.2562758.

[4] “Optical wireless communications,” *Wikipedia*. Jun. 14, 2021. Accessed: Dec. 21, 2021. [Online]. Available: https://en.wikipedia.org/w/index.php?title=Optical_wireless_communications&oldid=1028441051

[5] D. Karunatilaka, F. Zafar, V. Kalavally, and R. Parthiban, “LED Based Indoor Visible Light Communications: State of the Art,” *IEEE Commun. Surv. Tutor.*, vol. 17, no. 3, pp. 1649–1678, thirdquarter 2015, doi: 10.1109/COMST.2015.2417576.

[6] “MmWave and VLC-Based Indoor Channel Models in 5G Wireless Networks | IEEE Journals & Magazine | IEEE Xplore.” https://ieeexplore.ieee.org/document/8443599 (accessed Jun. 29, 2022).

[7] O. Ulgen, U. Ozmat, and E. Gunaydin, “Hybrid Implementation of Millimeter Wave and Visible Light Communications for 5G Networks,” in *2018 26th Telecommunications Forum (TELFOR)*, Nov. 2018, pp. 1–4. doi: 10.1109/TELFOR.2018.8611818.

[8] A. R. Ndjiongue, H. C. Ferreira, and T. M. N. Ngatched, “Visible Light Communications (VLC) Technology,” in *Wiley Encyclopedia of Electrical and Electronics Engineering*, American Cancer Society, 2015, pp. 1–15. doi: 10.1002/047134608X.W8267.

[9] S. Arnon, J. R. Barry, G. K. Karagiannidis, R. Schober, and M. Uysal, *Advanced Optical Wireless Communication Systems*. 2006.

[10] A. W. Mahmood Zuhdi and A. Zuhdi, “High performance drive circuits for integrated microLED/CMOS arrays for visible light communication (VLC),” Jun. 2015, Accessed: Dec. 11, 2019. [Online]. Available: https://era.ed.ac.uk/handle/1842/10006

[11] “Different Wi-Fi Protocols and Data Rates,” *Intel*. https://www.intel.com/content/www/uk/en/support/articles/000005725/network-and-i-o/wireless-networking.html (accessed Mar. 02, 2020).

[12] “IEEE 802.11,” *Wikipedia*. Mar. 02, 2020. Accessed: Mar. 02, 2020. [Online]. Available: https://en.wikipedia.org/w/index.php?title=IEEE_802.11&oldid=943463365

[13] R. Bian, I. Tavakkolnia, and H. Haas, “15.73 Gb/s Visible Light Communication With Off-the-Shelf LEDs,” *J. Light. Technol.*, vol. 37, no. 10, pp. 2418–2424, May 2019, doi: 10.1109/JLT.2019.2906464.

[14] Z. Ahmed, R. Singh, W. Ali, G. Faulkner, D. O’Brien, and S. Collins, “A SiPM-Based VLC Receiver for Gigabit Communication Using OOK Modulation,” *IEEE Photonics Technol. Lett.*, vol. 32, no. 6, pp. 317–320, Mar. 2020, doi: 10.1109/LPT.2020.2973200.

[15] “Technical Options for improving in Building Coverage,” *Ofcom*, Sep. 13, 2016. https://www.ofcom.org.uk/research-and-data/telecoms-research/mobile-smartphones/improving-building-coverage (accessed Dec. 05, 2019).

[16] R. X. G. Ferreira *et al.*, “High Bandwidth GaN-Based Micro-LEDs for Multi-Gb/s Visible Light Communications,” *IEEE Photonics Technol. Lett.*, vol. 28, no. 19, pp. 2023–2026, Oct. 2016, doi: 10.1109/LPT.2016.2581318.

[17] X. Li *et al.*, “Wireless Visible Light Communications Employing Feed-Forward Pre-Equalization and PAM-4 Modulation,” *J. Light. Technol.*, vol. 34, no. 8, pp. 2049–2055, Apr. 2016, doi: 10.1109/JLT.2016.2520503.
[18] D. Tsonev *et al.*, “A 3-Gb/s Single-LED OFDM-Based Wireless VLC Link Using a Gallium Nitride $\mu\rm LED$,” *IEEE Photonics Technol. Lett.*, vol. 26, no. 7, pp. 637–640, Apr. 2014, doi: 10.1109/LPT.2013.2297621.
[19] H. Elgala, R. Mesleh, and H. Haas, “Indoor optical wireless communication: potential and state-of-the-art,” *IEEE Commun. Mag.*, vol. 49, no. 9, pp. 56–62, Sep. 2011, doi: 10.1109/MCOM.2011.6011734.
[20] “Lighting Levels in the Workplace | (UK) Health & Safety,” *ATP Instrumentation Ltd*, Feb. 27, 2017. https://www.atp-instrumentation.co.uk/blog/lighting-levels-workplace/ (accessed Dec. 18, 2019).
[21] W. Ali, G. Faulkner, Z. Ahmed, W. Matthews, and S. Collins, “Giga-Bit Transmission Between an Eye-Safe Transmitter and Wide Field-of-View SiPM Receiver,” *IEEE Access*, vol. 9, pp. 154225–154236, 2021, doi: 10.1109/ACCESS.2021.3116704.
[22] “PIN vs. APD: Different Sensitivity, Different Applications | Electronics360.” https://electronics360.globalspec.com/article/10397/pin-vs-apd-different-sensitivity-different-applications (accessed Dec. 23, 2021).
[23] K. Orechovesky, “Avalanche Photodiodes: A User’s Guide,” p. 8.
[24] “Single Photon Detectors.” https://www.thorlabs.com/newgrouppage9.cfm?objectgroup_id=5255 (accessed Dec. 23, 2021).
[25] A. Giudice *et al.*, “High-rate photon counting and picosecond timing with silicon-SPAD based compact detector modules,” *J. Mod. Opt.*, vol. 54, no. 2–3, pp. 225–237, Jan. 2007, doi: 10.1080/09500340600763698.
[26] D. Chitnis, “Single photon avalanche diodes for optical communications,” http://purl.org/dc/dcmitype/Text, Oxford University, UK, 2013. Accessed: Feb. 01, 2020. [Online]. Available: https://ora.ox.ac.uk/objects/uuid:5fd582dd-8167-4fe4-88f8-871ba905ade1
[27] “Photon 2020.” https://www.europeanoptics.org/events/eos-co-sponsored/photon-2020.html (accessed Dec. 23, 2021).
[28] D. R. Paschotta, “Interference Filters.” https://www.rp-photonics.com/interference_filters.html (accessed Dec. 24, 2021).
[29] “Optical Filters | Edmund Optics.” https://www.edmundoptics.co.uk/knowledge-center/application-notes/optics/optical-filters/ (accessed Dec. 24, 2021).
[30] D. Milovančev, T. Jukić, N. Vokić, P. Brandl, B. Steindl, and H. Zimmermann, “VLC Using 800-µm Diameter APD Receiver Integrated in Standard 0.35-µm BiCMOS Technology,” *IEEE Photonics J.*, vol. 13, no. 1, pp. 1–13, Feb. 2021, doi: 10.1109/JPHOT.2020.3036549.
[31] H. Li, X. Chen, J. Guo, and H. Chen, “A 550 Mbit/s real-time visible light communication system based on phosphorescent white light LED for practical high-speed low-complexity application,” *Opt. Express*, vol. 22, no. 22, pp. 27203–27213, Nov. 2014, doi: 10.1364/OE.22.027203.
[32] Z. Lu *et al.*, “Active tracking system for visible light communication using a GaN-based micro-LED and NRZ-OOK,” *Opt. Express*, vol. 25, no. 15, pp. 17971–17981, Jul. 2017, doi: 10.1364/OE.25.017971.
[33] T. Jukić, B. Steindl, R. Enne, and H. Zimmermann, “200 µm APD OEIC in 0.35 µm BiCMOS,” *Electron. Lett.*, vol. 52, no. 2, pp. 128–130, 2016, doi: 10.1049/el.2015.3540.
[34] B. Fahs, A. J. Chowdhury, and M. M. Hella, “A 12-m 2.5-Gb/s Lighting Compatible Integrated Receiver for OOK Visible Light Communication Links,” *J. Light. Technol.*, vol. 34, no. 16, pp. 3768–3775, Aug. 2016, doi: 10.1109/JLT.2016.2587598.

[35] D. Milovančev, P. Brandl, T. Jukić, B. Steindl, N. Vokić, and H. Zimmermann, “Optical wireless APD receivers in 0.35 µm HV CMOS technology with large detection area,” *Opt. Express*, vol. 27, no. 9, pp. 11930–11945, Apr. 2019, doi: 10.1364/OE.27.011930.
[36] “Semipolar GaN-based laser diodes for Gbit/s white lighting communication: devices to systems.” https://www.spiedigitallibrary.org/conference-proceedings-of-spie/10532/105321N/Semipolar-GaN-based-laser-diodes-for-Gbit-s-white-lighting/10.1117/12.2315791.short?SSO=1 (accessed Jan. 27, 2022).
[37] Z. Ahmed, L. Zhang, G. Faulkner, D. O’Brien, and S. Collins, “A Shot-Noise Limited 420 Mbps Visible Light Communication System using Commerical Off-the-Shelf Silicon Photomultiplier (SiPM),” in *2019 IEEE International Conference on Communications Workshops (ICC Workshops)*, May 2019, pp. 1–5. doi: 10.1109/ICCW.2019.8757030.
[38] J. Kosman *et al.*, “29.7 A 500Mb/s -46.1dBm CMOS SPAD Receiver for Laser Diode Visible-Light Communications,” in *2019 IEEE International Solid- State Circuits Conference - (ISSCC)*, Feb. 2019, pp. 468–470. doi: 10.1109/ISSCC.2019.8662427.
[39] “High Bandwidth Visible Light Communications Based on a Post-Equalization Circuit | IEEE Journals & Magazine | IEEE Xplore.” https://ieeexplore.ieee.org/document/6657715 (accessed Jan. 27, 2022).
[40] L. Zhang *et al.*, “A Comparison of APD- and SPAD-Based Receivers for Visible Light Communications,” *J. Light. Technol.*, vol. 36, no. 12, pp. 2435–2442, Jun. 2018.
[41] C. Wang, H.-Y. Yu, Y.-J. Zhu, T. Wang, and Y.-W. Ji, “Experimental study on SPAD-based VLC systems with an LED status indicator,” *Opt. Express*, vol. 25, no. 23, pp. 28783–28793, Nov. 2017, doi: 10.1364/OE.25.028783.
[42] R. M. Gutierrez and A. I. Hernandez, “An optical Network Communication System performance using Silicon Photo Multipliers (SiPM),” in *2018 20th International Conference on Transparent Optical Networks (ICTON)*, Jul. 2018, pp. 1–4. doi: 10.1109/ICTON.2018.8473809.
[43] D. Milovančev, J. Weidenauer, B. Steindl, M. Hofbauer, R. Enne, and H. Zimmermann, “Visible light communication at 50 Mbit/s using a red LED and an SPAD receiver,” in *2018 11th International Symposium on Communication Systems, Networks Digital Signal Processing (CSNDSP)*, Jul. 2018, pp. 1–4. doi: 10.1109/CSNDSP.2018.8471890.
[44] H. Zimmermann, “APD and SPAD Receivers : Invited Paper,” in *2019 15th International Conference on Telecommunications (ConTEL)*, Jul. 2019, pp. 1–5. doi: 10.1109/ConTEL.2019.8848547.
[45] Z. Ahmed, L. Zhang, G. Faulkner, D. O’Brien, and S. Collins, “A Shot-Noise Limited 420 Mbps Visible Light Communication System using Commerical Off-the-Shelf Silicon Photomultiplier (SiPM),” in *2019 IEEE International Conference on Communications Workshops (ICC Workshops)*, May 2019, pp. 1–5. doi: 10.1109/ICCW.2019.8757030.
[46] L. Zhang, H. Chun, Z. Ahmed, G. Faulkner, D. O’Brien, and S. Collins, “The Future Prospects for SiPM-Based Receivers for Visible Light Communications,” *J. Light. Technol.*, vol. 37, no. 17, pp. 4367–4374, Sep. 2019, doi: 10.1109/JLT.2019.2923957.
[47] C. Lu, J. Wang, S. Li, and Z. Xu, “60m/2.5Gbps Underwater Optical Wireless Communication with NRZ-OOK Modulation and Digital Nonlinear Equalization,” in *2019 Conference on Lasers and Electro-Optics (CLEO)*, May 2019, pp. 1–2. doi: 10.1364/CLEO_SI.2019.SM2G.6.
[48] O. Almer *et al.*, “A SPAD-based Visible Light Communications Receiver Employing Higher Order Modulation,” pp. 0–5, 2015.
[49] D. Chitnis and S. Collins, “A SPAD-Based Photon Detecting System for Optical Communications,” vol. 32, no. 10, pp. 2028–2034, 2014.
[50] L. Zhang *et al.*, “A comparison of APD and SPAD based receivers for visible light communications,” no. Vlc.

[51] D. Chitnis and S. Collins, “A SPAD-Based Photon Detecting System for Optical Communications,” *J. Light. Technol.*, vol. 32, no. 10, pp. 2028–2034, May 2014, doi: 10.1109/JLT.2014.2316972.
[52] E. Fisher, I. Underwood, and R. Henderson, “A Reconfigurable Single-Photon-Counting Integrating Receiver for Optical Communications,” *IEEE J. Solid-State Circuits*, vol. 48, no. 7, pp. 1638–1650, Jul. 2013, doi: 10.1109/JSSC.2013.2253222.
[53] H. P. K.K, “Measuring the electrical and optical properties of silicon photomultipliers.” https://hub.hamamatsu.com/us/en/technical-note/electrical-optical-sipm-properties/index.html (accessed Jan. 02, 2020).
[54] N. Dinu, “8 - Silicon photomultipliers (SiPM),” in *Photodetectors*, B. Nabet, Ed. Woodhead Publishing, 2016, pp. 255–294. doi: 10.1016/B978-1-78242-445-1.00008-7.
[55] A. Vil�, A. Arbat, E. Vilella, and A. Dieguez, “Geiger-Mode Avalanche Photodiodes in Standard CMOS Technologies,” 2012. doi: 10.5772/37162.
[56] “Single-pixel photon counting modules / Single-photon avalanche diode (SPAD).” https://www.hamamatsu.com/eu/en/product/optical-sensors/mppc/photon-counting-module/index.html (accessed Dec. 28, 2021).
[57] L. Baudis, A. Kish, and M. S. J. Wulf, “Characterization of silicon photomultiplier arrays in liquid xenon and development of dedicated read-out electronics,” PhD Thesis, 2016.
[58] V. Chmill, E. Garutti, R. Klanner, M. Nitschke, and J. Schwandt, “Study of the breakdown voltage of SiPMs,” *Nucl. Instrum. Methods Phys. Res. Sect. Accel. Spectrometers Detect. Assoc. Equip.*, vol. 845, pp. 56–59, Feb. 2017, doi: 10.1016/j.nima.2016.04.047.
[59] A. Fiory and N. Ravindra, “Light emission from silicon: Some perspectives and applications,” *J. Electron. Mater.*, vol. 32, pp. 1043–1051, Oct. 2003, doi: 10.1007/s11664-003-0087-1.
[60] “Application Notes: Silicon Photomultipliers (SiPM).” https://www.onsemi.com/design/resources/design-resources/appnotes?category=17940 (accessed Dec. 29, 2021).
[61] Frank Träger, *Lasers and Optics*, 2nd ed. Springer, New York, NY.
[62] R. M. Gagliardi and S. Karp, “Optical communications,” *wi*, 1976.
[63] A. N. Otte, D. Garcia, T. Nguyen, and D. Purushotham, “Characterization of Three High Efficiency and Blue Sensitive Silicon Photomultipliers,” *Nucl. Instrum. Methods Phys. Res. Sect. Accel. Spectrometers Detect. Assoc. Equip.*, vol. 846, pp. 106–125, Feb. 2017, doi: 10.1016/j.nima.2016.09.053.
[64] Govind P. Agrawal, *Fiber-Optic Communication Systems*, 4th ed. WILEY, 2010.
[65] “Design of Integrated Circuits for Optical Communications, 2nd Edition | Wiley,” *Wiley.com*. https://www.wiley.com/en-us/Design+of+Integrated+Circuits+for+Optical+Communications%2C+2nd+Edition-p-9781118439456 (accessed Jan. 01, 2022).
[66] K. Nallappan, H. Guerboukha, C. Nerguizian, and M. Skorobogatiy, “Uncompressed HD and Ultra-HD Video Streaming Using Terahertz Wireless Communications,” in *2018 11th Global Symposium on Millimeter Waves (GSMM)*, May 2018, pp. 1–3. doi: 10.1109/GSMM.2018.8439548.
[67] “What is FEC, and How Do I Use It?” https://www.signalintegrityjournal.com/articles/1284-what-is-fec-and-how-do-i-use-it (accessed Jan. 01, 2022).
[68] A. A. Jafaar, “Reed-Solomon Hybrid Codes For Optical Communications.” Nov. 05, 2013. Accessed: Jan. 01, 2022. [Online]. Available: https://www.iasj.net/iasj/download/827abaeeeb6b1af6
[69] K. Szczerba, P. Westbergh, E. Agrell, M. Karlsson, P. A. Andrekson, and A. Larsson, “Comparison of Intersymbol Interference Power Penalties for OOK and 4-PAM in Short-Range Optical Links,” *J. Light. Technol.*, vol. 31, no. 22, pp. 3525–3534, Nov. 2013.

[70] S. Pudlewski and T. Melodia, “On the Performance of Compressive Video Streaming for Wireless Multimedia Sensor Networks,” in *2010 IEEE International Conference on Communications*, May 2010, pp. 1–5. doi: 10.1109/ICC.2010.5502135.
[71] A. A. Atayero, O. I. Sheluhin, and Y. A. Ivanov, “Modeling, Simulation and Analysis of Video Streaming Errors in Wireless Wideband Access Networks,” in *IAENG Transactions on Engineering Technologies: Special Edition of the World Congress on Engineering and Computer Science 2011*, H. K. Kim, S.-I. Ao, and B. B. Rieger, Eds. Dordrecht: Springer Netherlands, 2013, pp. 15–28. doi: 10.1007/978-94-007-4786-9_2.
[72] U. Pal and H. King, “Effect of UHD High Frame Rates (HFR) on DVB-S2 Bit Error Rate (BER),” in *SMPTE15: Persistence of Vision - Defining the Future*, Jul. 2015, pp. 1–11. doi: 10.5594/M001606.
[73] “4 Reasons Why HEVC (H.265) Matters, and How You Can Start Using It Now,” *Teradek*. https://teradek.com/blogs/articles/3-reasons-why-hevc-x265-matters-and-how-you-can-start-using-it-now (accessed Jan. 02, 2022).
[74] Sherman Karp and Robert M. Gagliardi, *Optical Communications*, 2nd ed. Wiley-Interscience, 1995.
[75] R. Hui, *Introduction to Fiber-Optic Communications*. Elsevier, 2019.
[76] E. Säckinger, *Analysis and design of transimpedance amplifiers for optical receivers*. John Wiley & Sons, 2017.
[77] E. Sackinger, “Analysis and Design of Transimpedance Amplifiers for Optical Receivers,” 2017. doi: 10.1002/9781119264422.
[78] “Equalization (communications),” *Wikipedia*. Aug. 14, 2021. Accessed: Jan. 03, 2022. [Online]. Available: https://en.wikipedia.org/w/index.php?title=Equalization_(communications)&oldid=1038770406
[79] “Illuminance - Recommended Light Level.” https://www.engineeringtoolbox.com/light-level-rooms-d_708.html (accessed Dec. 26, 2019).
[80] “Lighting Comparison: LED vs Fluorescent and CFL.” https://www.stouchlighting.com/blog/fluorescent-vs-led-vs-cfl (accessed Jan. 04, 2022).
[81] “MPPCs (SiPMs)/MPPC arrays.” https://www.hamamatsu.com/eu/en/product/optical-sensors/mppc/mppc_mppc-array/index.html (accessed Feb. 04, 2020).
[82] “Silicon Photomultipliers (SiPM).” https://www.onsemi.com/products/sensors/silicon-photomultipliers-sipm (accessed Feb. 04, 2020).
[83] “R-Series Silicon Photomultiplier (SiPM) Sensors - onsemi | Mouser.” https://www.mouser.co.uk/new/onsemi/onsemi-r-sipm-sensors/ (accessed Jan. 18, 2022).
[84] “J-SERIES SIPM: Silicon Photomultiplier Sensors, J-Series (SiPM).” https://www.onsemi.com/products/sensors/photodetectors-sipm-spad/silicon-photomultipliers-sipm/j-series-sipm (accessed Jan. 11, 2022).
[85] P. Eckert, H.-C. Schultz-Coulon, W. Shen, R. Stamen, and A. Tadday, “Characterisation Studies of Silicon Photomultipliers,” *Nucl. Instrum. Methods Phys. Res. Sect. Accel. Spectrometers Detect. Assoc. Equip.*, vol. 620, no. 2–3, pp. 217–226, Aug. 2010, doi: 10.1016/j.nima.2010.03.169.
[86] D. Chitnis *et al.*, “A 200 Mb/s VLC demonstration with a SPAD based receiver,” in *2015 IEEE Summer Topicals Meeting Series (SUM)*, Jul. 2015, pp. 226–227. doi: 10.1109/PHOSST.2015.7248280.
[87] M. Green and M. Keevers, “Optical properties of intrinsic silicon at 300 K,” *Prog. Photovolt. Res. Appl.*, vol. 3, pp. 189–192, 1995, doi: 10.1002/pip.4670030303.
[88] A. Eisele *et al.*, “185 MHz Count Rate, 139 dB Dynamic Range Single-Photon Avalanche Diode with Active Quenching Circuit in 130 nm CMOS Technology,” Jun. 2011.
[89] S. H. Lee and R. P. Gardner, “A new G–M counter dead time model,” *Appl. Radiat. Isot.*, vol. 53, no. 4, pp. 731–737, Nov. 2000, doi: 10.1016/S0969-8043(00)00261-X.

[90] Y. Li, M. Safari, R. Henderson, and H. Haas, “Nonlinear Distortion in SPAD-Based Optical OFDM Systems,” in *2015 IEEE Globecom Workshops (GC Wkshps)*, Dec. 2015, pp. 1–6. doi: 10.1109/GLOCOMW.2015.7414148.
[91] H. P. K.K, “A technical guide to silicon photomultipliers (MPPC) - Section 3.” https://hub.hamamatsu.com/us/en/technical-note/sipm-mppc-technical-note/section3.html (accessed Jan. 19, 2022).
[92] W. Matthews, W. Ali, Z. Ahmed, G. Faulkner, and S. Collins, “Inter-Symbol Interference and Silicon Photomultiplier VLC Receivers in Ambient Light,” *IEEE Photonics Technol. Lett.*, vol. 33, no. 9, pp. 449–452, May 2021, doi: 10.1109/LPT.2021.3067511.
[93] Z. Ahmed, R. Singh, W. Ali, G. Faulkner, D. O’Brien, and S. Collins, “A SiPM-Based VLC Receiver for Gigabit Communication Using OOK Modulation,” *IEEE Photonics Technol. Lett.*, vol. 32, no. 6, pp. 317–320, Mar. 2020, doi: 10.1109/LPT.2020.2973200.
[94] L. N. Staff, “White Light vs. Yellow Light: Which is Better for Eyes When Reading & Studying,” *Lumen Now*, Aug. 17, 2020. https://lumennow.org/reading-light-white-or-yellow/ (accessed Feb. 01, 2022).
[95] “8b/10b Encoder/Decoder.” Accessed: Feb. 21, 2020. [Online]. Available: https://www.latticesemi.com/-/media/LatticeSemi/Documents/ReferenceDesigns/1D/8b10bEncoderDecoder-Documentation.ashx?document_id=5653
[96] “Equalize modulated signals using decision feedback filtering - Simulink - MathWorks United Kingdom.” https://uk.mathworks.com/help/comm/ref/decisionfeedbackequalizer.html (accessed Jun. 29, 2022).
[97] “Decision Feedback Equalizer - Principles of Digital Communications - OpenStax CNX.” https://cnx.org/contents/BzNzlwcY@7.9:xqfdTpnk@4/Decision-Feedback-Equalizer (accessed Jun. 29, 2022).
[98] “5.1.5.6. Decision Feedback Equalization (DFE).” https://www.intel.com/content/www/us/en/docs/programmable/683617/21-1/decision-feedback-equalization-dfe.html (accessed Jun. 29, 2022).
[99] “Equalization of Channels with ISI.” http://courses.ece.ubc.ca/564/chapter6.pdf (accessed Jan. 03, 2022).
[100] P. O’Shea, “DOE publishes technical brief clarifying misconceptions about safety of LED lighting,” *Electronic Products*, Oct. 23, 2014. https://www.electronicproducts.com/doe-publishes-technical-brief-clarifying-misconceptions-about-safety-of-led-lighting/ (accessed Jan. 19, 2022).
[101] “506.pdf.” Accessed: Jan. 19, 2022. [Online]. Available: https://www.thorlabs.com/catalogpages/506.pdf
[102] “Radiative Heat Transfer - 4th Edition.” https://www.elsevier.com/books/radiative-heat-transfer/modest/978-0-12-818143-0 (accessed Jan. 19, 2022).
[103] “Lambert’s cosine law,” *Wikipedia*. Nov. 03, 2021. Accessed: Jan. 19, 2022. [Online]. Available: https://en.wikipedia.org/w/index.php?title=Lambert%27s_cosine_law&oldid=1053287658
[104] “Ali et al. - A wide field-of-view receiver that incorporates fl.pdf.” Accessed: Jan. 10, 2022. [Online]. Available: https://www.owcconference.com/wp-content/uploads/2021/10/ali-OWC-2021-Eindhoven_.pdf
[105] “Signal Pre-Equalization in a Silicon Photomultiplier-Based Optical OFDM System | IEEE Journals & Magazine | IEEE Xplore.” https://ieeexplore.ieee.org/document/9343826 (accessed Jan. 27, 2022).
[106] C. He, Z. Ahmed, and S. Collins, “Optical OFDM and SiPM Receivers,” in *2020 IEEE Globecom Workshops (GC Wkshps*, Dec. 2020, pp. 1–6. doi: 10.1109/GCWkshps50303.2020.9367554.

[107] L. Zhang, R. Jiang, X. Tang, Z. Chen, J. Chen, and H. Wang, “A Simplified Post Equalizer for Mitigating the Nonlinear Distortion in SiPM Based OFDM-VLC System,” *IEEE Photonics J.*, vol. 14, no. 1, pp. 1–7, Feb. 2022, doi: 10.1109/JPHOT.2021.3127230.